

The Magnetic Properties of Ultrathin Films of Fe(001) Grown on Ag(001) Substrates

by

Kenneth Bjorn Urquhart

B.Sc., Simon Fraser University, 1983

M.Sc., Simon Fraser University, 1985

THESIS SUBMITTED IN PARTIAL FULFILLMENT OF

THE REQUIREMENTS FOR THE DEGREE OF

DOCTOR OF PHILOSOPHY

in the Department

of

Physics

© Kenneth Bjorn Urquhart 1989

SIMON FRASER UNIVERSITY

April 1989

All rights reserved. This work may not be reproduced
in whole or in part, by photocopy or other means,
without permission of the author.

Approval

Name: Kenneth Bjorn Urquhart
Degree: Doctor of Philosophy
Title of Thesis: The Magnetic Properties of Ultrathin Films of Fe(001) Grown on
Ag(001) Substrates.

Examining Committee:

Chairman: Dr. R.H. Enns

Dr. J.F. Cochran
Senior Supervisor

Dr. B. Heinrich

Dr. A.S. Arrott

Dr. E.D. Crozier

Dr. R.F.C. Farrow
External Examiner
IBM Almaden Research Center

Date Approved: April 11, 1989


PARTIAL COPYRIGHT LICENSE

I hereby grant to Simon Fraser University the right to lend my thesis, project or extended essay (the title of which is shown below) to users of the Simon Fraser University Library, and to make partial or single copies only for such users or in response to a request from the library of any other university, or other educational institution, on its own behalf or for one of its users. I further agree that permission for multiple copying of this work for scholarly purposes may be granted by me or the Dean of Graduate Studies. It is understood that copying or publication of this work for financial gain shall not be allowed without my written permission.

Title of Thesis/~~Project/Extended Essay~~

The Magnetic Properties of Ultrathin Iron Films Grown on Silver

Author:


(signature)

Kenneth Bjorn Urquhart

(name)

APRIL 18, 1989

(date)

Abstract

Ultrathin films of bcc Fe(001) have been grown on bulk Ag(001) single crystal substrates using the techniques of Molecular Beam Epitaxy (MBE). Reflection High Energy Electron Diffraction (RHEED), Auger Electron Spectroscopy (AES) and X-ray Photoemission Spectroscopy (XPS) were used to establish that iron grows epitaxially, layer-by-layer, on Ag and that Au and Ag grow layer-by-layer on Fe. The static and the dynamic magnetic properties of the films were studied using Ferromagnetic Resonance (FMR). Simplified techniques for extracting the magnetic parameters from the measured FMR spectra of ultrathin films are described.

Iron films were found to possess large uniaxial anisotropies with easy axis perpendicular to the specimen plane. In sufficiently thin films the saturation magnetization was oriented along the specimen normal in zero applied field. The uniaxial anisotropy was found to be associated with the film surfaces. *In-situ* FMR measurements identified the strength of the uniaxial anisotropy constant at vacuum/Fe, Au/Fe, and Ag/Fe interfaces as $K_s = 0.96, 0.64, \text{ and } 0.3 \text{ ergs/cm}^2$ respectively. The surface anisotropies deduced for {bulk Fe/noble metal} interfaces are in good agreement with the values exhibited by ultrathin films. The uniaxial anisotropy originates in the broken symmetry of an abrupt interface. The in-plane cubic anisotropy of bcc Fe(001) films decreases with film thickness. This was due to the presence of a weak fourth order in-plane surface anisotropy characterized by the surface anisotropy coefficient $K_1^{\text{surf}} = -0.033 \text{ ergs/cm}^2$. The surface in-plane and uniaxial perpendicular anisotropies are due to the spin-orbit interaction in iron. The Gilbert damping parameter and the spectroscopic g-factor are also associated with the spin-orbit interaction and are shown to provide additional information of use to theoreticians modeling the electronic structure of Fe.

Dedication

*For my mother, Thorun, my father, Jim, and the
keeper of my sanity, Lorraine Chinatambi.*

Acknowledgments

It has been a distinct pleasure to have been associated with the Magnetism and Surface Science Group at Simon Fraser University and to have been guided through the complexities of magnetism and molecular beam epitaxy by John Cochran, Bretislav Heinrich, and Tony Arrott. I consider it an honor to have known them and to have worked with them.

I thank my co-workers and friends, Jeff Rudd, Ken Myrtle, Don Hunter, Stephen Purcell, and John Dutcher for their advice, support, and assistance in matters of FMR, MBE, and otherwise. Many thanks to Ken Myrtle, Les Bird and the members of the SFU machine shop for constructing the *in-situ* and *ex-situ* Ferromagnetic Resonance systems used in this work.

I am grateful to John Cochran, Michael Wortis, and Gerri Sinclair for allowing me to use their MacII computers to create and laserprint this thesis. I am indebted to my examining committee, especially Bretislav Heinrich and John Cochran, for their critical reading of this thesis and their valuable comments on its content.

The operations staff of SFU Computing Services went out of their way to keep me happy during data analysis. To this end, I would especially like to thank Rose Doucet, Kirby Mah, Bruce McCubbin, Diane Smith, Shannon Thomas, Doug Davey, and Gerry Adams for being truly "user-friendly".

I would like to give special thanks to Donna Kloeble, Jesse Girard, Corinna Rezanoff, Jeanie Kawakami and all the members of the 6:45 a.m. Early Bird fitness class for helping me take off and keep off over 75 lbs. in dead weight during the course of my work.

Finally, I wish to acknowledge the Natural Sciences and Engineering Research Council and Simon Fraser University for financial support.

Table of Contents

Approval.....	ii
Abstract.....	iii
Dedication.....	iv
Acknowledgements.....	v
List of Tables.....	x
List of Figures.....	xi
1. Introduction.....	1
1.1 Historical Perspective.....	2
1.2 Introduction to Molecular Beam Epitaxy.....	4
1.3 Introduction to Ferromagnetic Resonance.....	7
1.4 The Road Map.....	12
2. The MBE Facility.....	13
2.1 Introduction.....	13
2.2 An Overview of the MBE Facility.....	13
2.3 Components of the Ultrahigh Vacuum System.....	17
2.3.1 The Boostivac Ion Pump.....	17
2.3.2 The Cryogenic Refrigeration Pump.....	19
2.3.4 The Turbopump.....	20
2.3.5 The Cryosorption Pumps.....	21
2.4 The MBE Furnaces.....	22
2.5 The Quartz Crystal Thickness Monitor.....	24

2.5.1 A Word About the Accuracy of the Thickness Monitor.	25
2.6 Reflection High Energy Electron Diffraction (RHEED).	27
2.6.1 Interpretation of RHEED Patterns: Ewald's Construction.	29
2.6.2 The RHEED pattern of a perfect crystal: Ewald Spots.	30
2.6.3 The effect of surface disorder: RHEED Streaks.	32
2.6.4 Determination of the surface lattice structure with RHEED.	35
2.6.5 The effect of three dimensional surface features on RHEED streaks.	36
2.6.6 RHEED Oscillations: a measure of layer by layer growth.	37
2.6.7 Measuring film thickness with RHEED.	40
2.7 Surface Chemical Analysis using AES and XPS.	41
2.7.1 X-Ray Photoelectron Spectroscopy (XPS).	41
2.7.2 Auger Electron Spectroscopy (AES).	46
2.7.3 AES and XPS Spectrometers.	50
2.7.4 Determination of film thickness by means of AES and XPS.	55
2.8 The in situ FMR Spectrometer.	57
2.8.1 Experimental Measurement of FMR.	57
2.8.2 The in situ Microwave Cavity.	60
2.8.3 The in-situ FMR Spectrometer.	62
2.8.4 The in-situ Electromagnet.	65
2.8.5 The ex-situ FMR Spectrometers.	67
3. FMR Theory.	69
3.1 Introduction.	69
3.2 Calculation of the Microwave Absorption in an Ultrathin Film.	71
3.2.1 Maxwell's Equations.	73

3.2.2	The Equation of Motion for the Magnetization.	75
3.2.3	The Equilibrium Tilt Angle.	84
3.2.4	The Effective Microwave Permeability.	85
3.2.5	The Boundary Value Problem.	86
3.3	A Simplified Treatment of the Absorption Problem.	94
3.3.1	The Integrated Equations of Motion.	94
3.3.2	The Ferromagnetic Resonance Condition.	97
3.3.3	Extraction of the Saturation Magnetization.	100
4.	Ultrathin Iron Film Growth.	104
4.1	Introduction.	104
4.2	Preparing the Silver Substrates for Growth.	108
4.3	The Growth of Iron on Bulk Silver Substrates.	113
4.4	The Growth of Silver and Gold Coverlayers on Iron Films.	120
4.5	The Effect of Low Temperatures on Iron and Silver Film Growth.	122
5.	Results and Analysis.	125
5.1	Introduction.	125
5.2	Nomenclature.	127
5.3	Large Surface Anisotropies in Ultrathin Iron Films.	128
5.4	The Effect of the Coverlayer and the Role of Substrate Quality.	141
5.5	The Surface Anisotropy at the vacuum/Fe Interface.	146
5.6	The Dynamic Magnetic Processes in Ultrathin Iron Films.	152

Appendix A: The Ultrathin Film Demagnetizing Factor.....	156
Appendix B: Silver Substrate Preparation.....	165
Appendix C: Strain-Induced Uniaxial Anisotropy.....	171
References.....	175

List of Tables

Table	Page
5.1 The magnetic properties of {Au/Fe/Ag} films grown on vicinal substrates. . .	136
5.2 The magnetic properties of {Ag/Fe/Ag} films grown on vicinal substrates. . .	144
5.3 The magnetic properties of bcc Fe(001) films grown on singular substrates. . .	147
5.4 Intrinsic magnetic damping parameter and inhomogeneous linewidths.	153
A.1 The ultrathin film demagnetizing factors of bcc Fe(001).	164

List of Figures

Figure	Page
1.1 Schematic depiction of the growth of bcc Fe on Ag(001).	6
1.2 The FMR absorption derivative of a 2.8 ML Fe film.	8
2.1 Stylized view of the MBE Facility.	14
2.2 Heart of an ion pump.	18
2.3 MBE Furnace Assembly.	22
2.4 Location of the thickness monitor in the growth chamber.	24
2.5 The RHEED system installed in the growth chamber.	28
2.6 Ewald's Construction for a simple cubic crystal.	29
2.7 Ewald's Construction for the flat surface of a cubic crystal.	31
2.8 Representative RHEED patterns illustrating the effect of surface disorder.	33
2.9 Ewald's Construction for a disordered surface.	34
2.10 RHEED determination of the dimensions of the surface unit cell.	35
2.11 The formation of "chevrons" in a RHEED diffraction pattern.	36
2.12 Kinematic model of RHEED Oscillations.	38
2.13 Behavior of RHEED intensity oscillations as a function of path difference.	39
2.14 The photoemission process utilized in XPS.	42
2.15 The XPS spectrum of a bulk Ag substrate.	43
2.16 Illustration of the "escape depth" for electrons in a metal.	44
2.17 Diagram of the Auger process.	46
2.18 The derivative Auger spectrum of an oxidized bulk Ag(001) substrate.	49
2.19 Cross section of a Cylindrical Mirror Analyzer.	51

2.20 The AES Geometry.	53
2.21 Diagram of the XPS detection geometry.	54
2.22 Calculation of the film thickness, d , using AES.	56
2.23 The simplest practical microwave spectrometer.	58
2.24 The <i>in-situ</i> 16.88 GHz resonant microwave cavity.	61
2.25 The <i>in-situ</i> 16.88 GHz microwave cavity and mount in the MBE facility.	63
2.26 Diagram of the <i>in-situ</i> 16.88 GHz FMR spectrometer.	64
2.27 Side view of the electromagnet used for <i>in-situ</i> FMR.	66
2.28 Electrical and cooling water connections to the electromagnet.	67
2.29 Block diagram of the <i>ex-situ</i> 73.0 GHz FMR spectrometer.	68
3.1 The geometry used to model the FMR experiment.	71
3.2 Origin of the demagnetizing field.	78
3.3 The geometry of the ultrathin film boundary value problem.	87
4.1 Schematic depiction of the growth of bcc Fe(001) on Ag(001).	105
4.2 Diagram of the specimen holders used in the MBE facility.	108
4.3 RHEED patterns of silver substrates prior to film growth.	111
4.4 RHEED patterns of ultrathin bcc Fe(001) films deposited on Ag(001).	113
4.5 RHEED oscillations recorded for the growth of Fe(001) on Ag(001).	116
4.6 RHEED patterns of the Au and Ag capping layers deposited on Fe(001).	120
4.7 RHEED oscillations associated with the growth of Au and Ag on Fe(001). ...	122
4.8 RHEED patterns for low temperature Fe(001) growths on Ag(001).	123

5.1 FMR absorption derivative of a 28 ML {Au/Fe/Ag} film.	132
5.2 FMR absorption derivative of a 17.2 ML {Au/Fe/Ag} film.	133
5.3 FMR absorption derivative of a 5.3 ML {Au/Fe/Ag} film.	134
5.4 FMR absorption derivative of a 2.8 ML {Au/Fe/Ag} film.	135
5.5 Variation of the effective demagnetizing field with film thickness.	137
5.6 Plot of the uniaxial anisotropy constant versus film thickness.	138
5.7 Plot of the effective in-plane cubic anisotropy versus $1/d$	141
5.8 FMR absorption derivatives of a 3.0 ML {Ag/Fe/Ag} film.	143
5.9 FMR absorption derivatives of a 7.6 ML {Fe/Ag} film.	148
B.1 The polishing jig used to hold the substrate during grinding.	166
B.2 The electropolishing bath.	169

Chapter 1

Introduction

This thesis presents the results of an investigation into the structural and magnetic properties of ultrathin bcc Fe(001)* single crystal films grown layer by layer on Ag(001) single crystal substrates in ultrahigh vacuum (UHV) the order of 10^{-10} Torr using the techniques of Molecular Beam Epitaxy (MBE). The films ranged in thickness from 2 to 28 monolayers** (ML) and were either left bare or covered with films of Au or Ag. The motivation for this work originated in the spin-polarized photoemission experiments of Jonker *et al.* (1986), and recent theoretical calculations by Gay and Richter (1986, 1987), which indicated that Fe films on the order of one or two monolayers thick possessed a strong uniaxial surface anisotropy which pulled the magnetization along the specimen normal in zero applied field.

By carrying out Ferromagnetic Resonance (FMR) experiments on well defined bcc Fe(001) films grown on bulk Ag(001) substrates, we have directly verified the existence of a large uniaxial surface anisotropy in ultrathin iron films and determined how this anisotropy scales with film thickness, growth conditions, and contamination levels. We have also found that iron films possess a strong in-plane surface anisotropy with easy axes along the {110} directions. Most of the measurements were made outside ultrahigh vacuum using 9.6, 36.6 and 73.0 GHz FMR spectrometers. This necessitated covering

* The notation bcc Fe(001) refers to a bcc iron film oriented with the [100] axis normal to the film plane.

** For a bcc film whose [100] direction is normal to the film plane, each layer of Fe atoms (monolayers) is separated by 1.425\AA from its neighboring monolayers (1.425\AA is one half the length of a side of the bcc unit cell). A 5ML Fe film is therefore $5 \times (1.425\text{\AA}) = 7.125\text{\AA}$ thick.

the bare Fe films with protective layers of Au(001) or Ag(001) single crystal. In order to investigate the prediction by Gay and Richter (1987) that the details of the magnetic/non-magnetic interface might strongly affect the magnetic properties of a film, a special FMR probe operating at 16.88 GHz was designed and constructed for use in the ultrahigh vacuum MBE facility where the films were grown. This allowed for a detailed examination of the uniaxial surface and cubic in-plane anisotropies of bare Fe films grown on silver and the way in which the anisotropies were affected by the creation of a second Ag/Fe or Au/Fe interface when the films were covered by Ag or Au.

Section 1.1 of this chapter contains a detailed history of the work by Jonker *et al.* and by Gay and Richter that motivated this present study. This is followed by an introduction to the techniques of Molecular Beam Epitaxy (MBE) in section 1.2 and of Ferromagnetic Resonance (FMR) in section 1.3. MBE is essential for the consistent and reproducible growth of well defined, ultrathin Fe films – a necessity for any systematic investigation of film properties. FMR provides an ideal tool for determining the fundamental magnetic parameters of a film, especially the bulk and surface anisotropies, the spectroscopic g-factor (Kittel, 1949), and magnetic damping parameter. Section 1.4 presents a “road map” to the rest of this thesis.

1.1 Historical Perspective

In 1985, Richter *et al.* (1985) and Fu *et al.* (1985) independently calculated the magnetic moment of a monolayer of bcc Fe(001) supported by a Ag(001) substrate. Both groups predicted that a monolayer of iron should possess a magnetic moment of $3.0\mu_B$ per atom, where μ_B is the Bohr Magnetron. This 36% increase over the bulk iron moment of $2.2\mu_B$ per atom would put the film’s saturation magnetization at $4\pi M_s \approx 30$ kOe compared with the bulk iron value of 21.55 kOe. Such an enhancement had neither been

predicted nor observed at that time in any other ferromagnetic film supported by a bulk nonmagnetic substrate. If anything, nonmagnetic substrates were predicted to quench the film's moment relative to that of the bulk due to band hybridization at the magnetic/non-magnetic interface (Richter *et al.*, 1985).

Jonker *et al.* (1986) looked for this enhanced moment while studying the spin polarization of photoelectrons emitted from ultrathin Fe(001) films epitaxially grown on Ag(001) substrates. They found no net spin imbalance (ie, no net magnetic moment) along the in-plane [100] direction for Fe films up to 2.5 ML thick. They suggested that their result was caused by a large uniaxial surface anisotropy with easy axis normal to the specimen plane rather than a decrease in the ferromagnetic Curie temperature, T_c of Fe from 1200° C to near room temperature where the experiments were carried out. The latter explanation was felt to be less likely in view of the measurements of Bader *et al.* (1986) that indicated $T_c \geq 0.5T_c(\text{bulk})$ for comparable Fe films grown on Au(001).

Gay and Richter (1986, 1987) provided support for these conclusions when they added a spin-orbit interaction to their fully self-consistent localized orbital (SCLO) theory and explicitly calculated the magnetocrystalline anisotropy in unsupported monolayers of Fe, Ni, and V using the lattice spacing of a Ag(001) crystal plane. For an isolated Fe monolayer, Gay and Richter predicted:

- (1) The Fe monolayer would be magnetized normal to the specimen plane due to a large uniaxial surface anisotropy.
- (2) The magnetic moment would be enhanced to $3.2\mu_b$ per atom compared with $2.2\mu_b$ per atom in bulk iron.

- (3) The monolayer should exhibit an in-plane cubic anisotropy with magnetically "easy" axes along the {100} directions whose strength would be about an order of magnitude larger than that found in bulk iron.
- (4) The demagnetizing field in Fe films thicker than a monolayer would be strong enough to pull the magnetization back into the plane.
- (5) Supporting the Fe monolayer with a Ag(001) substrate *might* substantially decrease the uniaxial surface anisotropy and put the magnetization back into the plane.

Conclusion (5) indicated that the anisotropy was a sensitive function of the details of the electronic structure at the magnetic/non-magnetic interface. However, Gay and Richter pointed out that the amount of decrease in the uniaxial anisotropy due to the Ag/Fe interface could not be accurately determined because of convergence problems with their SCLO calculations.

1.2 Introduction to Molecular Beam Epitaxy

While it's still impossible to grow unsupported single crystal films, thin film technology has advanced to the point where one can now deposit pure, ultrathin single crystal films on top of bulk single crystal substrates whose surfaces are smooth on the atomic scale over large areas and free from contamination. This technique has come to be known as Molecular Beam Epitaxy or MBE, a reference to its original purpose: the growth of single crystal semi-conducting III-V compounds. Without a properly equipped MBE facility, it would not have been possible to carry out the systematic investigation of the magnetic properties of Fe films reported in this thesis.

MBE is essentially an ultrahigh vacuum (UHV) deposition technique carried out at background pressures of the order of 10^{-10} Torr or less. A properly equipped MBE facility will also include a Reflection High Energy Electron Diffraction (RHEED) unit and

provision for Auger Electron Spectroscopy (AES) and/or X-Ray Photoemission Spectroscopy (XPS). RHEED is a low angle electron diffraction technique that's extremely sensitive to the surface structure of a film. It can be used to continuously monitor the surface quality and crystalline perfection of a substrate and of any subsequently deposited films (see, for example, Lent and Cohen, 1986 or Pendry, 1975). Intensity oscillations of specific features in the RHEED diffraction pattern indicate whether a film is growing atomic layer by atomic layer – a process vital to the growth of single crystal films more than a few layers thick (Neave et al., 1983, Van Hove et al., 1983, Purcell et al., 1987 and 1988). If layer-by-layer growth is indicated, RHEED oscillations can be used to determine the film thickness to within ± 0.1 monolayer or better (Purcell et al., 1988). AES (Davis et al., 1979) and XPS (Wagner et al., 1979) spectroscopies are used to measure the contamination levels of films and substrates and the average film thickness (see section 2.7.4).

The simplest possible thin film structure that can be experimentally realized is that of an ultrathin film grown on a supporting substrate. The substrate can be viewed as an atomic "template" that the film atoms will attempt to follow as they rain down upon its surface; in effect, the film atoms will try to grow into a single crystal that in some way mimics the structure of the substrate underneath. Silver is a natural choice for the substrate upon which to grow bcc Fe. When the (001) surface of a cubic fcc Ag crystal is rotated by 45° , the spacing of 2.8839\AA between adjacent Ag surface atoms very closely matches the 2.8665\AA spacing between adjacent Fe atoms on the (001) surface of an iron crystal. The situation is shown in Fig. 1.1, where the growth of one layer of bcc Fe on Ag(001) is depicted. The horizontal mismatch between the film and the substrate is only 0.6%, which is considered to be very good for epitaxial (ie, single crystal) growth. The vertical spacing between adjacent layers of bcc Fe(001) is 1.43\AA while the corre-

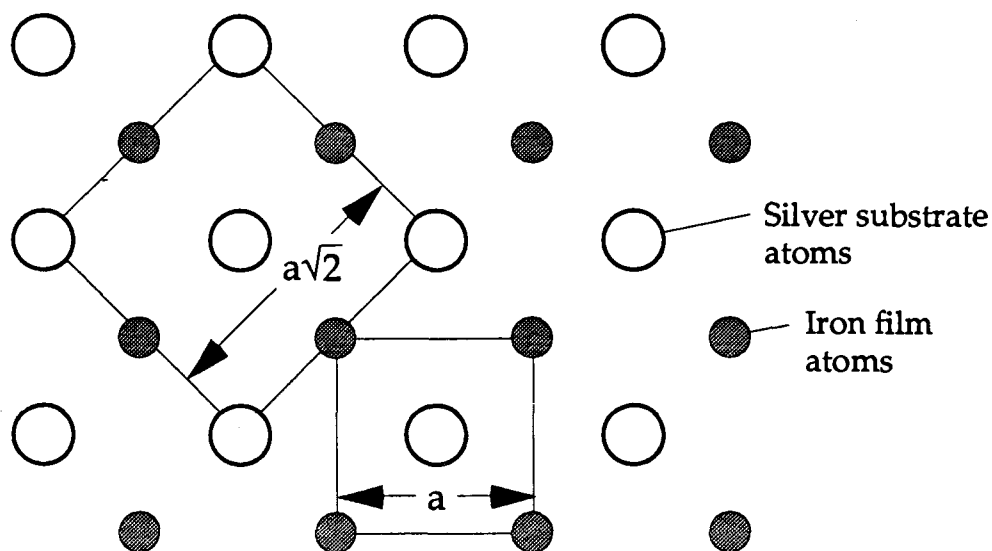


Fig. 1.1 Schematic depiction of the growth of bcc Fe on a (001) surface of fcc Ag. After a 45° rotation, the silver surface net matches the (001) fcc Fe surface net to within 0.8%. The spacing "a" of the rotated Ag(001) surface net is 2.8839\AA while that of Fe(001) is 2.8665\AA . Such a close match is essential if bcc Fe is to grow layer-by-layer on top of a silver single crystal.

sponding vertical spacing between adjacent layers of fcc Ag(001) is 2.04\AA , a 43% difference. This is of little consequence if the silver substrate is an absolutely flat (001) plane but in the actual experiments, the silver crystal will be neither absolutely flat nor oriented exactly parallel to the (001) plane. In that case, the large vertical mismatch might cause the iron film to grow unevenly for at least the first few monolayers.

The (001) surfaces of fcc Au and Al could also be used as substrates for the growth of bcc Fe(001) films. However, both metals are unsuitable candidates because Fe has been shown to strongly intermix with Au and Al during growth at room temperatures (Bader and Moog, 1987). The result is an ill-defined film/substrate interface which would be different for each new specimen and these variations in structure would interfere with

any systematic study of Fe film properties. Our results indicate that Fe grows epitaxially layer-by-layer on Ag, and vice versa, with any intermixing at room temperature being limited to within one monolayer of the Fe/Ag interface (see chapter 4). Interestingly, our results also show that Au, like Ag, can be grown *on top* of Fe without intermixing of more than one monolayer. Both metals are therefore suitable for covering an Fe film when measurements need to be carried out *ex-situ* (ie, outside of the UHV environment of the MBE facility). Covering a film with Au also allows for the investigation of how the details of the magnetic/non-magnetic interface affect the magnetic properties of an iron film since well defined vacuum/Fe, Ag/Fe, and Au/Fe interfaces can be created.

1.3 Introduction to Ferromagnetic Resonance

Ferromagnetic Resonance (FMR) is a powerful technique for determining the magnetic properties of a ferromagnetic metal (Heinrich, Cochran, and Baartman, 1977). A standard FMR spectrometer is readily adapted to the UHV environment of an MBE facility and, as demonstrated in Fig. 1.2, can detect a strong signal from a 2.8 ML (ie, 4Å) bcc Fe(001) film with a 1 cm² surface area. This allows for the study of single layer films instead of the more complicated multilayer structures required by other techniques such as Conversion Electron Mossbauer Spectroscopy (CEMS) (Volkening, 1988) or SQUID Magnetometry (Krebs *et al.*, 1988). FMR is especially useful for measuring the magnetocrystalline anisotropy coefficients and the magnetic damping parameter of a film. These quantities are related to the spin orbit interaction and can be calculated from first principles (Gay and Richter, 1986, 1987, and Kambersky, 1976). Measurement of the damping parameter also provides information on the magnetic homogeneity of the specimen, an aid in characterizing the quality of grown films. The strength of the

signal at resonance can be used, even in the presence of anisotropy, to measure the magnitude of the saturation magnetization, M_s , relative to a standard specimen for which M_s is known (see section 3.3.3).

In the FMR absorption experiment, the specimen is made part of the end wall of a cylindrical microwave cavity designed to resonate at a selected frequency f . A waveguide connected to the cavity through a small coupling hole feeds microwaves into the cavity and returns the portion of the microwave power not absorbed by the

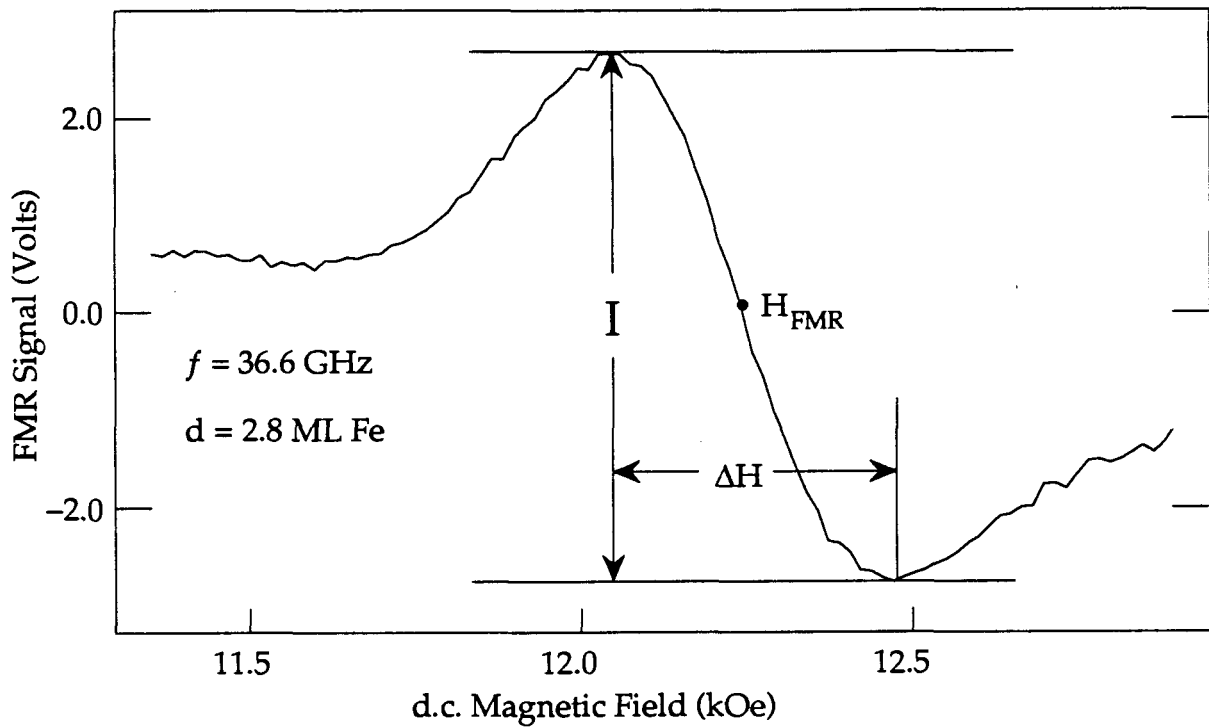


Fig. 1.2. The magnetic field derivative of the microwave absorption spectrum at 36.6 GHz for a 2.8 ML bcc Fe(001) film grown on a bulk Ag(001) single crystal. The iron film was covered with a 40Å layer of Au. The signal to noise ratio is approximately 40:1.

specimen, or the cavity walls, to a diode that outputs a voltage proportional to the microwave power incident upon it. A weakly modulated d.c. magnetic field is applied parallel to the specimen plane and the derivative of the absorbed microwave power is measured using standard lock-in amplification techniques as the d.c. field is swept through FMR. A typical FMR spectrum is shown in Fig. 1.2, collected at 36.6 GHz for a 2.8 ML bcc Fe(001) film grown on Ag(001). The lineshape is defined by a resonance field H_{FMR} (the zero crossing of the absorption derivative) and linewidth ΔH (the field interval between the extrema of the absorption derivative). Both quantities can be related to the magnetic properties of the ferromagnet using the prescription of Ament and Rado (1955) which combines the equation of motion for the specimen's magnetization with Maxwell's equations subject to boundary conditions appropriate to the specimen geometry. The equation of motion for the magnetization,

$$-\left(\frac{1}{\gamma}\right)\frac{\partial \mathbf{M}}{\partial t} = \mathbf{M} \times \mathbf{H}_{\text{eff}}, \quad (1.1)$$

describes the response of the magnetization, \mathbf{M} , to an effective magnetic field, \mathbf{H}_{eff} , which contains the applied d.c. magnetic field, H , the driving microwave magnetic field h , the internal demagnetizing field, the exchange field, fields associated with surface and volume magnetocrystalline anisotropy energies, and a field associated with magnetic damping processes. The absorption experiment is analogous to the case of a specimen irradiated at normal incidence by linearly polarized microwaves while a uniform d.c. magnetic field is applied parallel to the specimen plane and perpendicular to the incident microwave magnetic field (see Fig. 3.1 in section 3.2). The solution in the ultrathin limit (film thickness $d \ll [A/2\pi M_s^2]^{1/2}$, where A is the exchange stiffness constant) leads to an analytic equation that relates the magnetic properties of the film to the microwave frequency, $f = \omega/2\pi$, and the d.c. field, H_{FMR} , corresponding to FMR.

For ultrathin iron films, this equation takes the form (see section 3.3):

$$\left(\frac{\omega}{\gamma}\right)^2 = \left[H_{\text{FMR}} + (4\pi D_z M_s)_{\text{eff}} + \frac{K_1}{2M_s}(3 + \cos 4\theta) \right] \left[H_{\text{FMR}} + \frac{2K_1}{M_s} \cos 4\theta \right] \quad (1.2)$$

where $\gamma = g |e| / (2mc)$ is the gyromagnetic ratio, g is the g -factor, θ is the angle between the magnetization, M_s , and the [100] in-plane direction, $2K_1/M_s$ is the effective in-plane cubic anisotropy field associated with a cubic anisotropy energy term of the form $E_A = K_1(\alpha_1^2\alpha_2^2 + \alpha_2^2\alpha_3^2 + \alpha_3^2\alpha_1^2)$, and $(4\pi D_z M_s)_{\text{eff}}$ is an effective in-plane saturation magnetization given by

$$(4\pi D_z M_s)_{\text{eff}} = 4\pi D_z M_s - \frac{2K_s}{dM_s} \quad (1.3)$$

where D_z is the “thin film” demagnetizing factor (a number between 0.5 and 1 – see Appendix A), d is the film thickness, and K_s is a surface uniaxial anisotropy energy parameter associated with both surfaces of the film. The last term in (1.3) describes the effect of a uniaxial surface anisotropy energy of the form $E_s = -K_s(m_z/M_s)^2$, where m_z is the magnetization component normal to the film surface. This is the surface energy that Gay and Richter (1986) predicted would be large enough to overcome the in-plane demagnetizing field $4\pi D_z M_s$ and magnetize ultrathin Fe films perpendicular to the plane in zero applied field.

Measuring the variation of the resonance field with θ at two different microwave frequencies ω allows one to determine K_1 , γ , and $(4\pi D_z M_s)_{\text{eff}}$ from equation (1.2). The gyromagnetic factor, γ , yields the g -factor, a measure of the residual spin-orbit interaction for the electrons contributing to the magnetization. If the magnetization and the film

thickness are known, then K_s can be obtained from equation (1.3). The frequency dependent linewidth of the resonance, $\Delta H(\omega)$ allows for the determination of both the intrinsic Gilbert damping factor, G , and the inhomogeneous linebroadening, $\Delta H(0)$, through the relation:

$$\Delta H(\omega) = \kappa \left(\frac{\omega}{\gamma} \right) \frac{G}{\gamma M_s} + \Delta H(0) \quad (1.4)$$

where the empirically determined constant, κ , is equal to 1.16 for ultrathin iron films. As mentioned previously, damping in ferromagnetic metals is caused by the spin-orbit interaction. Changes in the strength of the spin-orbit coupling due, for example, to changing specimen thickness, would be reflected in the Gilbert damping coefficient, G . The frequency independent part of the linewidth, $\Delta H(0)$, is caused by magnetic inhomogeneities in the film and is therefore a measure of the quality of the grown magnetic film. Two-magnon scattering theory can relate surface quality of a film to $\Delta H(0)$ (Heinrich *et al.*, 1985). In this respect, the frequency independent linebroadening could be as useful for characterizing grown magnetic films as photoluminescence line broadening is for MBE grown III-V compounds.*

The peak-to-peak amplitude, I , of a FMR spectra such as that shown in Fig. 1.2 is related to the magnetization, M_s , by

$$I \sim \frac{1}{2} \omega \frac{M_s d}{(\Delta H)^2} \left[\frac{H_{\text{FMR}} + (4\pi D_z M_s)_{\text{eff}}}{2H_{\text{FMR}} + (4\pi D_z M_s)_{\text{eff}}} \right] \quad (1.5)$$

* Dr. G.A. Prinz, private communication, 1987.

This relationship can be used to determine the magnitude of the saturation magnetization relative to that of a standard specimen for which M_s is known (see section 3.3.3).

1.4 The Road Map

Chapter 2 of this thesis describes the various components of the MBE machine used to carry out the work reported in this thesis. The surface analysis tools of RHEED, AES, and XPS, and the FMR system, are given particular emphasis. Chapter 3 covers the simple phenomenological FMR theory used to deduce the magnetic properties of ultrathin films from FMR spectra. An outline of the methods used to calculate the detailed line-shape of a spectrum is presented and simpler techniques for obtaining anisotropy and magnetization data are presented in some detail. Application of these techniques to include other effects such as magnetostriction are easily carried out. Chapter 4 discusses the growth of the ultrathin iron films. Chapter 5 presents the experimental results and discusses their significance in comparison with work reported by other groups.

Chapter 2

The MBE Facility

2.1 Introduction

Epitaxial growth of the ultrathin iron films was carried out in a Physical Electronics* molecular-beam epitaxy (Φ MBE-400) system. This MBE facility was equipped with the surface analysis tools of Reflection High Energy Electron Diffraction (RHEED), Auger Electron Spectroscopy (AES) and X-Ray Photoelectron Spectroscopy (XPS). A special 16.88 GHz FMR probe was installed in conjunction with this thesis work to allow the magnetic properties of bare iron films to be measured *in-situ*. This chapter describes the various components of the MBE system. We begin with an overview of the system followed by detailed descriptions of the various components.

2.2 An Overview of the MBE Facility

The general layout of the Φ MBE-400 facility is shown in Fig. 2.1. The system is built around two ultrahigh vacuum chambers connected by a small access tunnel. One chamber is used exclusively for film growth and the other for surface chemical analysis with AES and XPS. The ultrahigh vacuum is maintained in the low 10^{-10} Torr range by means of an ion pump attached to the bottom of the analysis chamber and a cryogenic refrigeration pump attached to the growth chamber. The vacuum in both chambers is monitored by means of several ionization gauges. The operation of these pumps is described in section 2.3. The growth chamber contains the metal evaporation furnaces

* Physical Electronics Division, Perkin-Elmer Corporation, U.S.A.

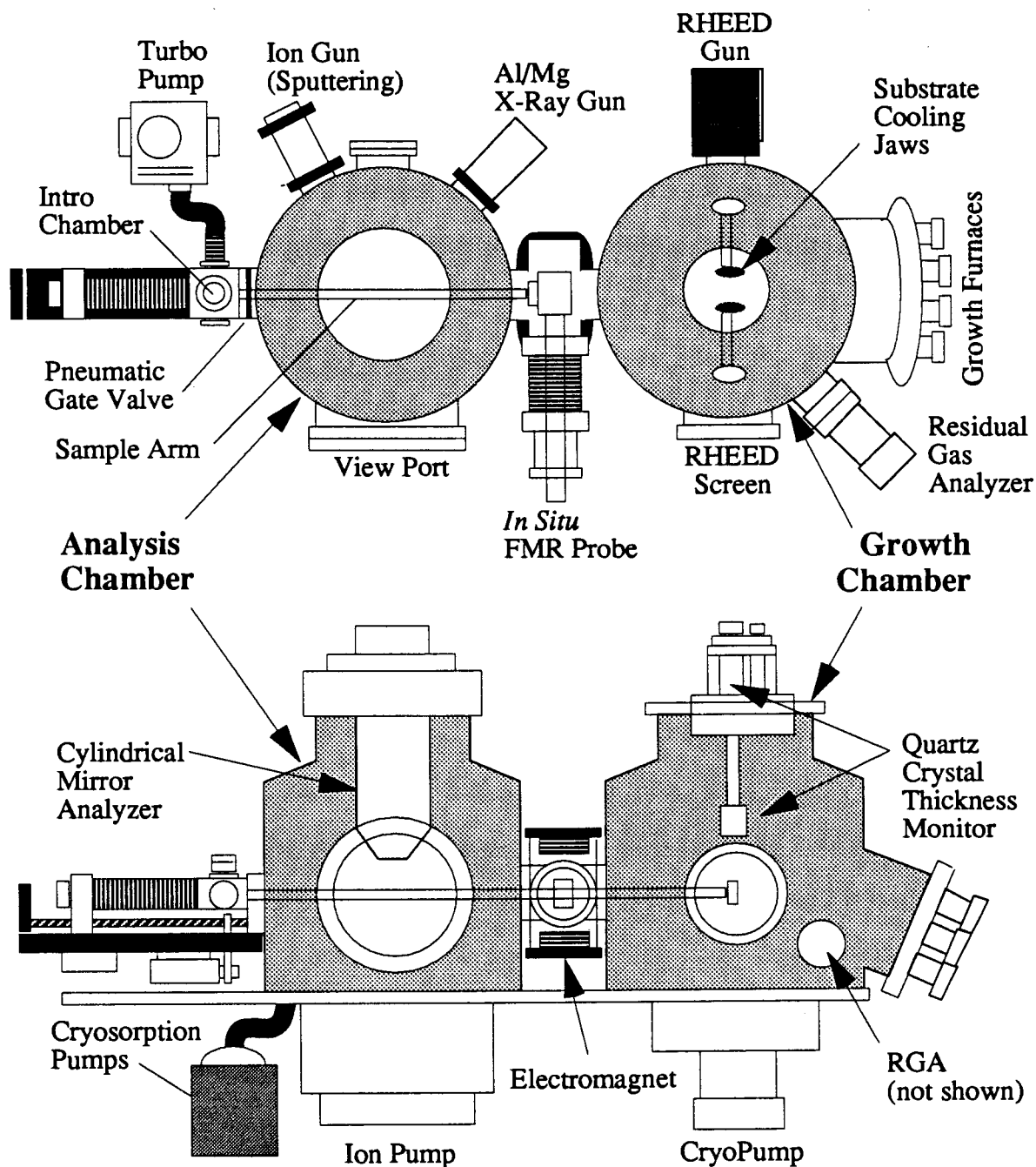


Fig. 2.1 Stylized top and side views of a PHI Model 400 Molecular Beam Epitaxy (MBE) facility showing the placement of the high vacuum pumps, growth furnaces, and analytic tools. The substrate is attached to the sample arm in the "intro-chamber" and prepared for film growth in the analysis chamber. The film is deposited onto the substrate in the growth chamber and the magnetic properties of the film determined by the *in situ* FMR probe located between the two chambers. The system was approximately 2.5 meters long and 2 meters high.

surrounded by a liquid nitrogen cooled cryoshroud. A temperature controlled Mathis* quartz crystal thickness monitor is mounted at the top of the chamber along with a pair of LN₂ cooled "claws" that serve to cool the substrate to ~140 K for low temperature growth (see Chapter 4). A 0–10 keV electron gun focussed on a SnO₂ coated phosphor screen forms the glancing angle (0–5°) RHEED unit used to continuously monitor film quality during growth (see section 2.6). A quadropole mass spectrometer (also called the Residual Gas Analyzer or RGA) can be used to monitor the levels of contaminants in the growth chamber or, by intercepting part of the flux from a growth furnace, serve as a second thickness monitor.

The analysis chamber houses the UHV surface analysis tools and the ion sputtering gun used to clean the substrates prior to growth. At the top of the chamber is an PHI model 15-255GAR precision energy analyzer consisting of a PHI Model 10-155 double pass cylindrical mirror analyzer (CMA) with built-in electron gun for Auger Electron Spectroscopy (AES). The CMA does double duty as an XPS spectrometer when used in conjunction with the water cooled Al/Mg X-ray source mounted on the side of the chamber. The spectrometers are described in more detail in section 2.7.

Specimens enter the MBE facility through the "intro-chamber", a small airlock connected to the analysis chamber by means of a pneumatic valve assembly. During mounting the specimen arm is retracted into the intro-chamber and sealed off from the rest of the MBE system. The intro-chamber is back filled with dry nitrogen and opened to the atmosphere. The overpressure of N₂ is maintained to minimize contamination of the rod and holder. Only the end of the specimen arm is exposed to the atmosphere at this time; most of the arm is protected inside a long metal bellows assembly which is

* R.E. Mathis Corporation,

continuously pumped to $\sim 10^{-6}$ Torr by means of a turbo-molecular pump. Following mounting of the specimen, the intro-chamber is resealed and the valve between the intro-chamber and the turbo-pump is opened to pump out the chamber to $\sim 10^{-6}$ Torr; this requires approximately one hour. A motor driven screw is used to move the specimen arm out of the intro-chamber, through the pneumatic valve, and into the analysis chamber for pre-growth preparation. The end of the specimen arm can be used to rotate the specimen about the long axis of the arm. A complex manipulator assembly upon which the substrate is mounted can be used to tilt the specimen 90° to the long axis so that it faces the CMA during AES or XPS analysis or so that it can be viewed by the operator at the observation port. A specimen heater located behind the substrate can be used to heat the substrate to a maximum temperature of 700°C for annealing and/or outgassing. The temperature of the substrate is measured by means of a thermocouple attached to the heater.

The growth and analysis chambers are connected by a tunnel just large enough to allow the specimen holder and arm to pass between the chambers. The tunnel contains the *in-situ* FMR probe which is described in section 2.8. The portion of the probe inside the MBE facility consists of a 16.9 GHz resonant microwave cavity attached to a length of KU-band waveguide. The waveguide is attached to a metal bellow assembly that allows the cavity to be placed in the connecting tunnel. The film deposited on a substrate is brought up to a 12 mm hole in the side of the cavity in order to carry out FMR measurements on it. FMR requires the specimen to be immersed in a uniform d.c. magnetic field parallel to the film plane. This is provided by a water cooled electromagnet that surrounds the connecting tunnel as shown in Fig. 2.1.

2.3 Components of the UltraHigh Vacuum System

This section describes the various pumps used to maintain a vacuum of approximately 10^{-10} Torr in the MBE system. The ultrahigh vacuum serves to minimize the presence of unwanted contaminants like water vapor, oxygen, and carbon which would otherwise settle onto the substrates and contaminate the ultrathin films during their growth.

2.3.1 The Boostivac Ion Pump

The analysis chamber is pumped by means of a "BoostiVac" ion pump* mounted below the analysis chamber. The components of the pump are shown in Fig. 2.2. A set of cylindrical anodes are each sandwiched between a pair of Titanium coated Tantalum cathodes. Permanent magnets mounted behind the cathodes generate a strong magnetic field through the assembly. When a 5000-7000 Volt potential is applied between the cathodes and the anodes, cold-cathode electron emission occurs and a stream of electrons are driven at high speed towards the anodes. The electrons follow spiral trajectories due to the magnetic field. Gas molecules entering the anode region are ionized by these spiralling electrons and, in turn, are accelerated towards one of the cathode plates where they sputter titanium atoms and bury themselves in the cathode. The sputtered titanium atoms are then free to combine with a variety of active gases in the anode region, such as O_2 , N_2 , and CO_2 , to form stable compounds which settle on the inner walls of the anodes. Noble gases like Helium and Argon are pumped by ion burial into the cathode while hydrogen is 'pumped' by diffusion into the cathodes.

A Titanium evaporation unit is used periodically to regenerate the sputtered Ti coat-

* available from Thermionics Vacuum Products, Hayward California

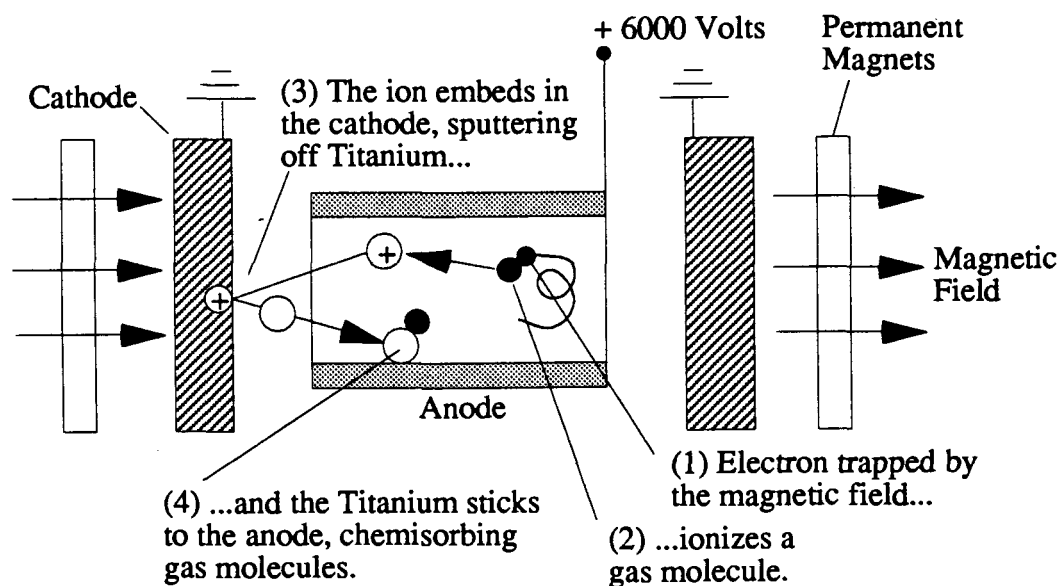


Fig 2.2. Heart of an ion pump. Electrons emitted by cold-cathode discharge are drawn towards a cylindrical anode, ionizing gas molecules in their path. The ionized molecules embed themselves in the cathodes, sputtering off Titanium atoms which chemisorb other gas molecules and form stable compounds on the anode walls. Noble gases like argon pump by ion burial in the cathodes, He and H pump by diffusion into the cathodes, and gases like O_2 , N_2 , and CO_2 pump by combining with the Ti.

ing on the cathodes. For pressures below 10^{-8} Torr, it is sufficient to evaporate Ti on the cathodes for 2 minutes every 24 hours. At higher pressures, a longer Ti deposition time is required to maintain pumping efficiency.

The combined action of noble gas pumping through ion burial in the cathodes, hydrogen pumping through diffusion into the cathodes, and chemisorption of other active gases by the sputtered titanium results in a very high vacuum at the expense of a low pumping speed compared with the cryopump described in the next section. However, the low pumping speed is offset by the fact that an ion pump has no moving parts. The resulting absence of pump vibration makes it an ideal choice to pump the analysis chamber where the CMA, shared by the AES and XPS spectrometers, is

housed. The CMA is a delicate instrument that must be isolated from mechanical vibration in order to operate at maximum sensitivity.

Ion pumps can be easily damaged by permitting the internal pressure of the analysis chamber to rise above some limiting value (about 5×10^{-6} Torr in the PHI Model-400 MBE system). For higher pressures, the sheer volume of sputtering ions can permanently damage the cathode plates. Such conditions are approached when the chamber is back filled with Argon during ion sputtering of specimens. During these times, the pump is normally run in "standby" mode with no potential applied between the cathodes and the anodes in order to avoid any damage to the cathode plates through excessive sputtering.

2.3.2 The Cryogenic Refrigeration System

The growth chamber is pumped by means of a helium cryopump. A cryopump is essentially a closed cycle refrigerator that uses helium gas as the refrigerant. The refrigerator operates on the Solvay cycle (E. Solvay, 1886) and the parts of it inside the growth chamber (the "cryopanel") reach a temperature of approximately 14 K. The cryopanel adsorb all kinds of gases except helium and hold the gases as long as the pump is turned on. A large valve sits between the cryopanel and the rest of the growth chamber and can be closed when the growth chamber might be exposed to the atmosphere for maintenance. This allows the cryopump to remain running so that the gas deposits remain firmly adsorbed. Removal of these deposits is carried out by switching off the refrigeration unit and allowing the pump to warm to room temperature while the area around the cryopanel is continuously pumped by means of a mechanical TurboPump. The valve separating the cryopanel from the rest of the chamber is closed during this cleaning process to prevent desorbed material from entering the growth chamber.

At the bottom of the cryopump is a rotary valve assembly that contains the moving parts of the refrigerator. The reciprocating action of this mechanical pump assembly causes the growth chamber to vibrate slightly with a period of approximately 0.5 seconds. The equipment in the growth chamber is relatively insensitive to this vibration but the spectrometers in the analysis chamber cannot operate at peak resolution if subjected to such shaking. To reduce the transmission of mechanical vibration between the growth chamber and the analysis chamber, part of their connecting passage consists of a shock absorbing metal bellows.

2.3.3 The TurboPump

Attached to the rear of the analysis chamber is the "intro-chamber", a small air-lock through which specimens are introduced into the ultrahigh vacuum. When the specimen arm is retracted into this chamber, a valve seals it off from the analysis chamber and the intro-chamber is maintained at a vacuum of $\sim 10^{-6}$ Torr by means of a Turbo Molecular Pump or "TurboPump". A turbopump is simply a set of carefully designed fan blades attached to a high speed motor rotating at 40,000 rpm. Heavy gas molecules hitting the fan blade assembly are swept out of the high vacuum side of the pump and passed to a venting connection where they are expelled from the pump. Vacuums as low as 4×10^{-8} Torr can be achieved in a clean chamber.

When the sample arm is inserted into the analysis chamber, a teflon ring fits snugly around the cylindrical arm and serves as the seal between the intro-chamber and the analysis chamber. Leakage through the teflon seal increases the pressure in the analysis chamber by $\sim 5 \times 10^{-11}$ Torr, approximately the same as the contribution to the background pressure due to outgassing from the walls of the analysis chamber.

2.3.4 The Cryosorption Pumps

When the MBE system has to be opened to the atmosphere for maintenance, the valves separating the ion pump and the cryopump from their respective chambers are closed and the chambers backfilled with dry nitrogen. The nitrogen pressure is kept above that of the surrounding atmosphere in order to minimize contamination of the system by oxygen and water vapor. After the MBE machine has been resealed, the rather large volume of nitrogen has to be pumped out. Cryosorption pumps attached to the analysis chamber serve admirably for this purpose. The pumps have no moving parts and use no oil or other materials which could leak back into the system and contaminate it. A cryosorption pump is essentially a metal container filled with adsorbents such as 5Å molecular sieve and/or processed oxides of Al and Si. Cooling the sorption pump's surrounding container with liquid nitrogen turns it into a most effective "getter" due to the large surface area of the sieve.

The cryopumps rapidly remove the nitrogen from the growth and analysis chambers. By employing two cryosorption pumps in sequence the system can be pumped to the low 10^{-4} Torr region within 30 minutes. At that point, the cryosorption pumps are sealed from the MBE system, the cryogenic refrigeration pump (section 2.3.2) can be re-opened and the system pressure further reduced to $\sim 10^{-7}$ Torr. The ion pump may then be safely re-opened and the final pump down to UHV ($\sim 10^{-10}$ Torr) takes place over the next few hours.

Outgassing of the "used" cryosorption pumps is carried out by means of a heating jacket which heats the sieve material to 300° C for 1–2 hours. The trapped nitrogen is released into the atmosphere through a small relief valve after the pumps have been sealed off from the UHV system.

2.4 The MBE Furnaces

The atomic beams used to grow the various ultrathin metallic films are produced by a set of eight furnaces located at the rear of the growth chamber (see Fig. 2.1). A typical furnace is shown in Fig. 2.3 (not to scale). Furnaces are built on 3" wide UHV mounting flanges and installed in "furnace wells" that open into the growth chamber through small holes ~2 cm in diameter. Each hole is covered with a pneumatically operated shutter which can be opened and closed to control the growth process. The entire set of furnaces are surrounded by a liquid nitrogen cooled "cryoshroud". The shroud reduces heating of the growth chamber during furnace operation. Such heating can release gas molecules adsorbed on the chamber walls which might contaminate a growing film.

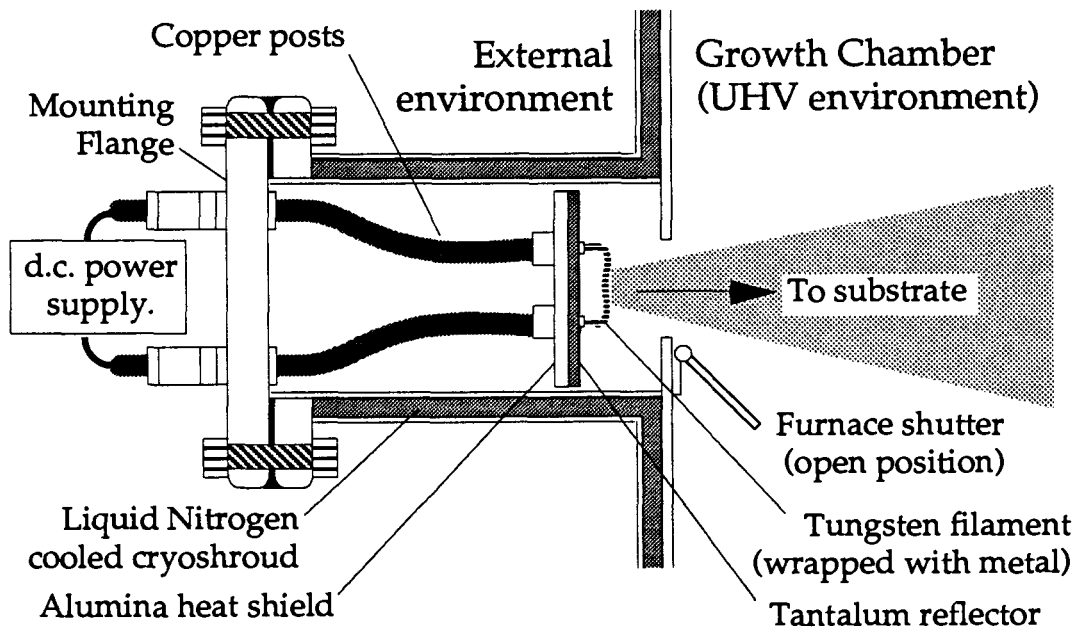


Fig. 2.3. A typical furnace assembly attached to the growth chamber. A beam of metal atoms is produced by sublimation from a strand of pure metal wire wrapped around a tungsten heating filament. Entry of the atomic beam into the growth chamber is controlled by a pneumatically operated shutter. A heat shield and reflector protects the furnace mount.

The furnace shown in Fig. 2.3 produces a beam of metal atoms by sublimation from a strand of pure metal wire (99.999%) wrapped around a tungsten heating filament. Tungsten is used because of its low vapor pressure compared with metals such as Fe, Ni, Ag, and Au. The filament is spot welded between a pair of electrically isolated copper posts that feed through the UHV mounting flange upon which the furnace is built. The posts serve both to support the filament and to supply it with current from an external d.c. power supply. Radiation heating of the furnace well is minimized by placing an alumina heat shield covered with a tantalum reflector immediately behind the filament. This works in conjunction with the cyroshroud to inhibit outgassing from the growth chamber walls and the rest of the furnace.

Filament-type furnaces were used to grow all of the iron films, and most of the Ag films, discussed in this thesis. Some of the Ag films, and all of the Au films, were grown using a different type of furnace consisting of a pyrolytic boron nitride (BN) crucible wrapped with coils of tungsten heating wire. Pellets of pure gold or silver were simply placed in the crucible and heated to approximately 1000 °C. BN crucible furnaces were a standard component of the original Model-400 MBE machine supplied by PHI (PHI part number 04-410). While such furnaces could be used to grow noble metals such as Au and Ag, they proved unsuitable for transition metals such as Fe and Ni because the BN crucibles tended to outgas considerable amounts of N₂ at the approximately 1200°C temperatures needed to sublimate the transition metals. The nitrogen intermixed with the metal atoms at the substrate and heavily contaminated the growing films.

2.5 The Quartz Crystal Thickness Monitor

A temperature controlled Mathis TM-100 thickness monitor was used in the growth chamber to measure the thickness of growing films. The thickness monitor consisted of a 6 MHz resonant circuit connected to a small piezoelectric quartz crystal located just above the substrate, see Fig. 2.4. During growth, a fraction of the metal atoms emitted from a furnace would be deposited on the oscillating quartz crystal. The increased mass deposited on the crystal surface caused the resonant frequency of the circuit to decrease in proportion with the thickness of the deposited film. The frequency of the loaded quartz crystal was compared with an external reference crystal. From this data it was possible to compute the thickness of a deposited film. Calculation of the thickness required certain material parameters (such as the mass per unit volume of the metal being deposited) to be entered into the thickness monitor by the operator. The monitor also had to be calibrated to account for the fact that the atomic flux intercepted by the piezoelectric crystal might not be the same as the flux intercepted by the substrate.

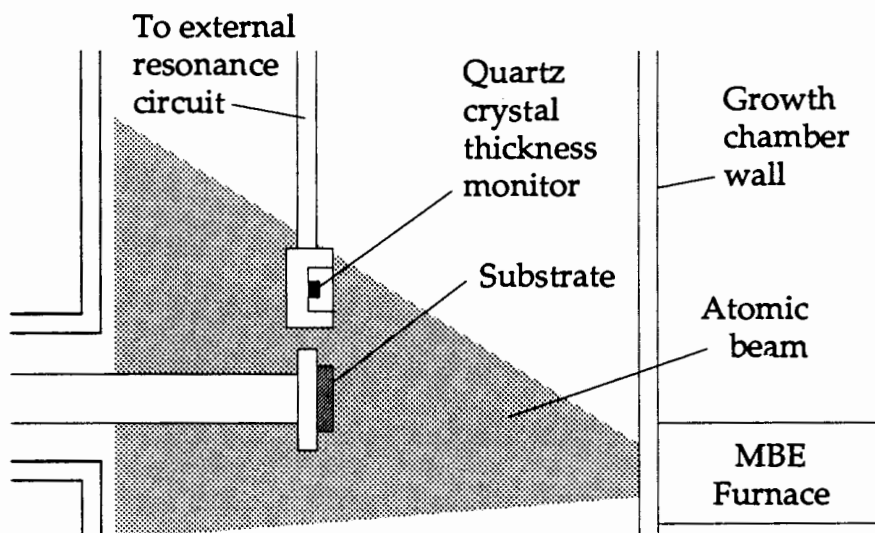


Fig. 2.4. Location of the thickness monitor used to measure the thickness of a film depositing on a substrate during growth.

The constant of proportionality between the two fluxes was referred to as the “tooling factor”. It had to be determined for each individual furnace because of their different positions and distances from the substrate and the quartz crystal. The procedure recommended by the manufacturer was to lower the thickness monitor to the position normally occupied by the substrate during growth and then determine the flux from a given furnace by plotting the increasing thickness measured by the monitor as a function of time (the thickness monitor supplies an analog dc voltage which is proportional to the thickness reading displayed on its front panel). The monitor was then moved to the position it would normally occupy during growth and the flux re-measured. The ratio of the fluxes yielded the tooling factor. Tooling factors for the PHI Model-400 MBE system ranged from 1.05 for the Au furnace mounted almost directly in front of the substrate and monitor to 1.2 for one of the Fe furnaces mounted below and to the side of the Au furnace.

2.5.1 A word about the accuracy of the thickness monitor...

The thickness monitor was extremely sensitive to the temperature of the quartz crystal. At $\sim 30^\circ\text{C}$, a one degree temperature change corresponded to a $\sim 1\text{\AA}$ change in the thickness reading displayed by the monitor. This was a serious problem when 2–5 \AA films were being grown. It was very easy to overshoot the thickness by several angstroms. The situation was improved by the construction of an elaborate temperature control system that circulated water of fixed temperature throughout the quartz crystal housing in the growth chamber. While this stabilized drifts in the monitor reading due to changes in the ambient temperature, it had little effect on temperature changes due to radiation heating inside the MBE machine. There were two competing sources: cooling due to the liquid nitrogen cooled cryoshroud surrounding the MBE furnaces and heat-

ing from the open furnace during growth. Cooling the cryoshroud with liquid nitrogen prior to growth caused the quartz crystal to cool down. This often resulted in a 1-2Å increase in the thickness registered by the monitor. It would then take approximately 2 hours for the reading to stabilize. Opening the furnace to initiate growth warmed the crystal and led to a decrease of 1-4 Å in the displayed thickness. Closing the furnace at the end of the growth would result in an increase in the final reading by several angstroms. A wait of several hours (while the cryoshroud cooling continued), was required to stabilize the thickness reading in order to obtain a true measure of the film thickness.

Using the thickness monitor was more often than not an exercise in extreme patience. Anything that might disturb the temperature of the quartz crystal would lead to a several hour wait while the monitor re-stabilized. RHEED intensity oscillations provided a solution to this dilemma. RHEED oscillations, described in section 2.5.7, could be used to determine the thickness of a film to within ± 0.1 ML provided that the film grew layer by layer on the substrate. Layer by layer growth occurred, for example, when Fe was grown on an Fe substrate or Ag was grown on a Ag substrate. RHEED oscillations provided an absolute calibration of the thickness monitor. The oscillations proved especially useful for calibrating the "apparent" film thickness displayed by the thickness monitor during growth. Following careful calibration, the thickness determined from quartz crystal monitor readings during growth agreed to within ± 0.5 ML of the final thickness determined after the quartz crystal had been allowed to stabilize for several hours.

2.6 Reflection High Energy Electron Diffraction

RHEED (Reflection High Energy Electron Diffraction) is a surface sensitive probe that is widely used to characterize the growth and surface morphology of ultrathin films (see, for example, Lent and Cohen, 1986 or Pendry, 1975). It allows the changing physical structure of a film to be observed during growth. Submonolayer atomic steps, terraces, and three dimensional structures are clearly indicated in RHEED patterns. Intensity oscillations in certain RHEED pattern features during growth (RHEED Oscillations) indicate the degree of layer by layer film growth. In the case of good layer-by-layer growth, the oscillations can provide a measure of the film thickness accurate to within ± 0.1 ML (Purcell et al., 1987, 1988a).

The RHEED system installed in the PHI Model-400 MBE machine is shown in Fig. 2.5. An electron gun mounted on one side of the growth chamber was used to generate a 0.5–10 keV electron beam. The beam impinged upon the surface of the specimen at low angles of incidence ranging from 0 to 5° . The resultant diffracted beams were displayed on a SnO_2 coated phosphor screen. The screen was located 30.5 cm from the specimen. A photomultiplier tube mounted on an x-y stage in front of the screen was used to measure changes in the intensity of the RHEED pattern. In order to concentrate attention on specific features of a pattern, a 1:1 microscope objective was used to form an image of a small area of the screen on a $50 \mu\text{m}$ pinhole covering the photomultiplier.

The glancing incidence geometry does not interfere with the atomic beams arriving at the specimen from the MBE furnaces. The RHEED system can therefore be used to continuously monitor the changing surface structure during film growth. The low angle geometry also results in a component of electron momentum normal to the surface that is so small that penetration of the high energy electron beam into a crystal is

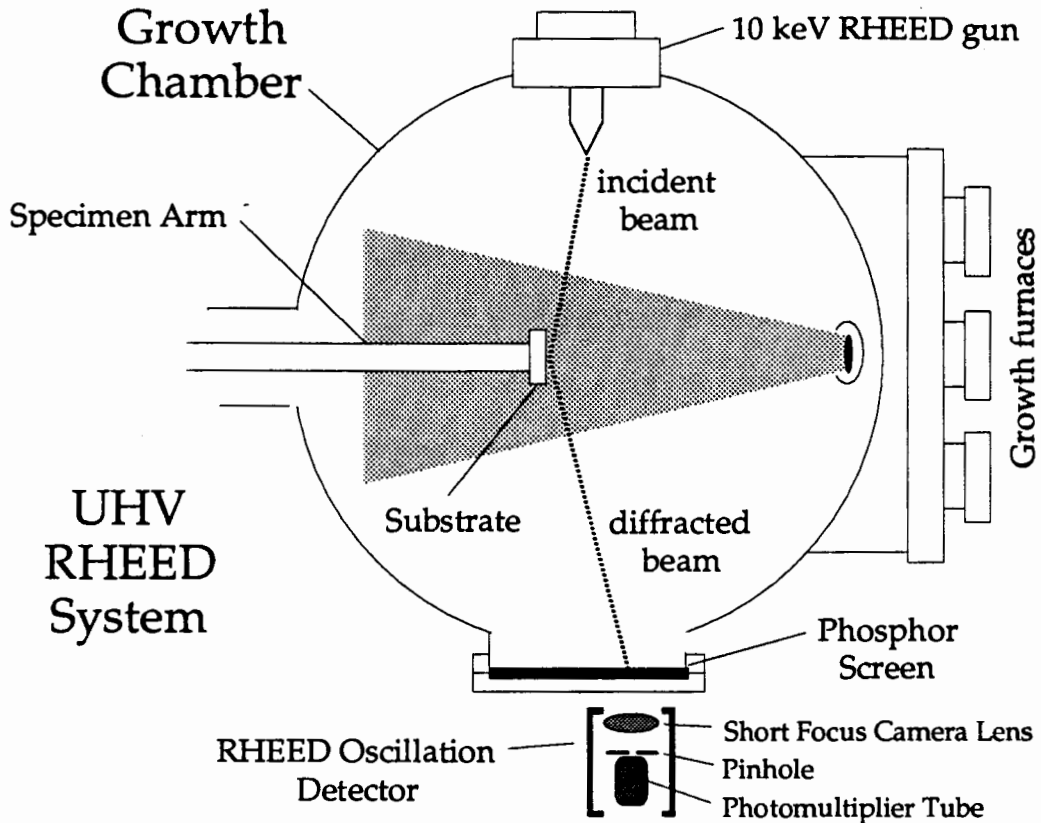


Fig. 2.5. The RHEED system installed in the growth chamber of a PHI Model 400 MBE machine. A 10 keV electron beam strikes the surface of the specimen at a glancing angle. Diffracted beams are created which strike the phosphor screen, producing bright spots and/or streaks indicative of the surface structure. Changes in the intensity of the spots (RHEED Oscillations) can be recorded during growth by means of an external detector. The growth chamber was approximately 0.5m in diameter.

basically limited to the first atomic layer. RHEED is therefore extremely surface sensitive.

RHEED patterns contain a great deal of information about the surface structure of a specimen. Depending on the surface, the patterns can range from a few sharp spots to a large number of thick smeary lines and blobs. The remainder of this section discusses qualitative interpretation of RHEED patterns.

2.6.1 Interpretation of RHEED patterns: Ewald's Construction

Cohen *et al.* (1987) have shown that simple kinematic theory can be used to qualitatively understand many RHEED pattern features. Kinematic theory assumes elastic scattering of electrons from the atoms at the specimen surface. In this limit, the conditions for constructive beam interference (and hence the appearance of the RHEED pattern) can be inferred from Ewald's construction: a simple geometric interpretation of the energy and momentum conservation rules necessary for constructive interference among electrons elastically scattered from the surface of a crystal. In Ewald's construction, one starts with the reciprocal lattice of the crystal and draws the wave-vector, k_i , of the incident electron beam such that it touches one of the lattice points. An "Ewald

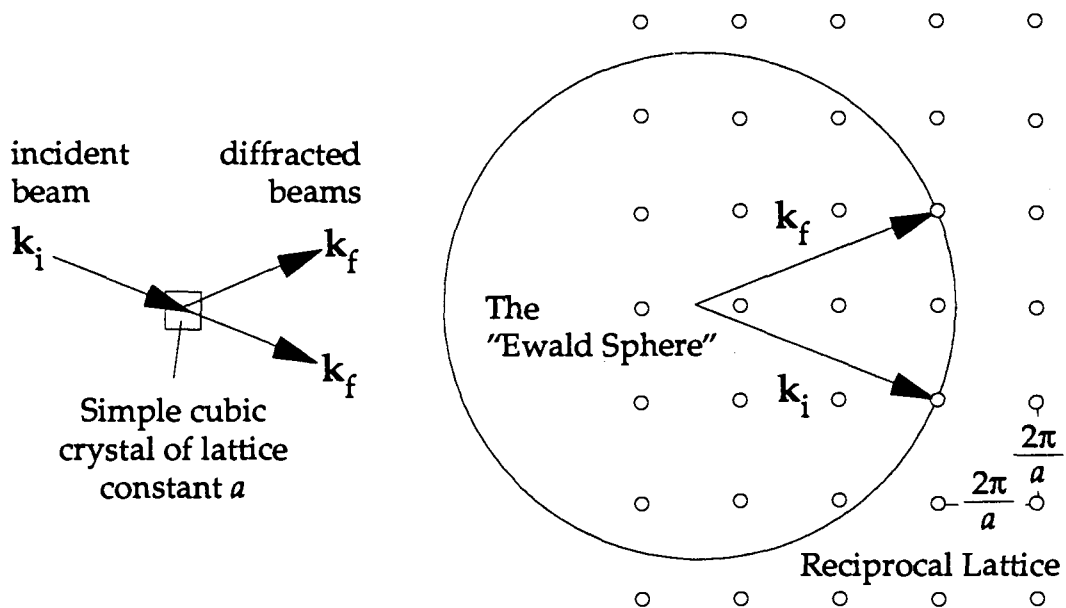


Fig. 2.6 The Ewald Construction for diffraction through a simple cubic crystal: a k -vector, k_i , drawn in the direction of the incident electron beam, is terminated at a reciprocal lattice point. A sphere of radius $k = 2\pi/\lambda$ is drawn about the origin of k_i . Diffracted beams will form along all directions k_f which can be drawn from the origin of the "Ewald Sphere" to the intersection between the sphere and the reciprocal lattice.

Sphere" of radius $|k_i|$ is then drawn about the origin of k_i . Wave-vectors, k_f , drawn from the origin of the sphere to all the points of intersection between the sphere and the reciprocal lattice determine the directions of all possible diffracted beams. Fig. 2.6 illustrates Ewald's construction for the case of a three dimensional, simple cubic lattice (the reciprocal lattice is also a cubic array of spots). Ewald's construction makes the interpretation of the most common RHEED pattern features a straightforward task.

2.6.2 The RHEED pattern of a perfect crystal: Ewald Spots

The grazing incidence RHEED geometry limits the penetration of the incident electron beam essentially to the two dimensional surface net of atoms. The reciprocal lattice of such a two dimensional net is a set of rods oriented normal to the surface.* Ewalds construction for such a lattice is shown in Fig. 2.7, along with the corresponding RHEED pattern, for an ideally flat (001) crystal face of bcc Fe. The RHEED pattern of a perfect crystal exhibits three main features: (1) a bright "specular spot" formed by the primary reflected beam whose angle of reflection equals the angle of incidence. (2) Additional spots created by non-specular beams. (3) A bright spot created by the portion of the incident beam that misses the specimen. All beams are arranged on an "Ewald circle" related to the intersection of the reciprocal lattice rods with the Ewald sphere. The diffracted spots are surrounded by a dim background due to inelastically scattered electrons. The "shadow edge" corresponds to the lowest take off angle of these inelastic electrons from the surface of the specimen.

* The reciprocal lattice of a linear lattice is a set of sheets. The reciprocal lattice of a 2-dimensional lattice is a set of rods. The reciprocal lattice of a 3-dimensional lattice is a 3-dimensional set of points.

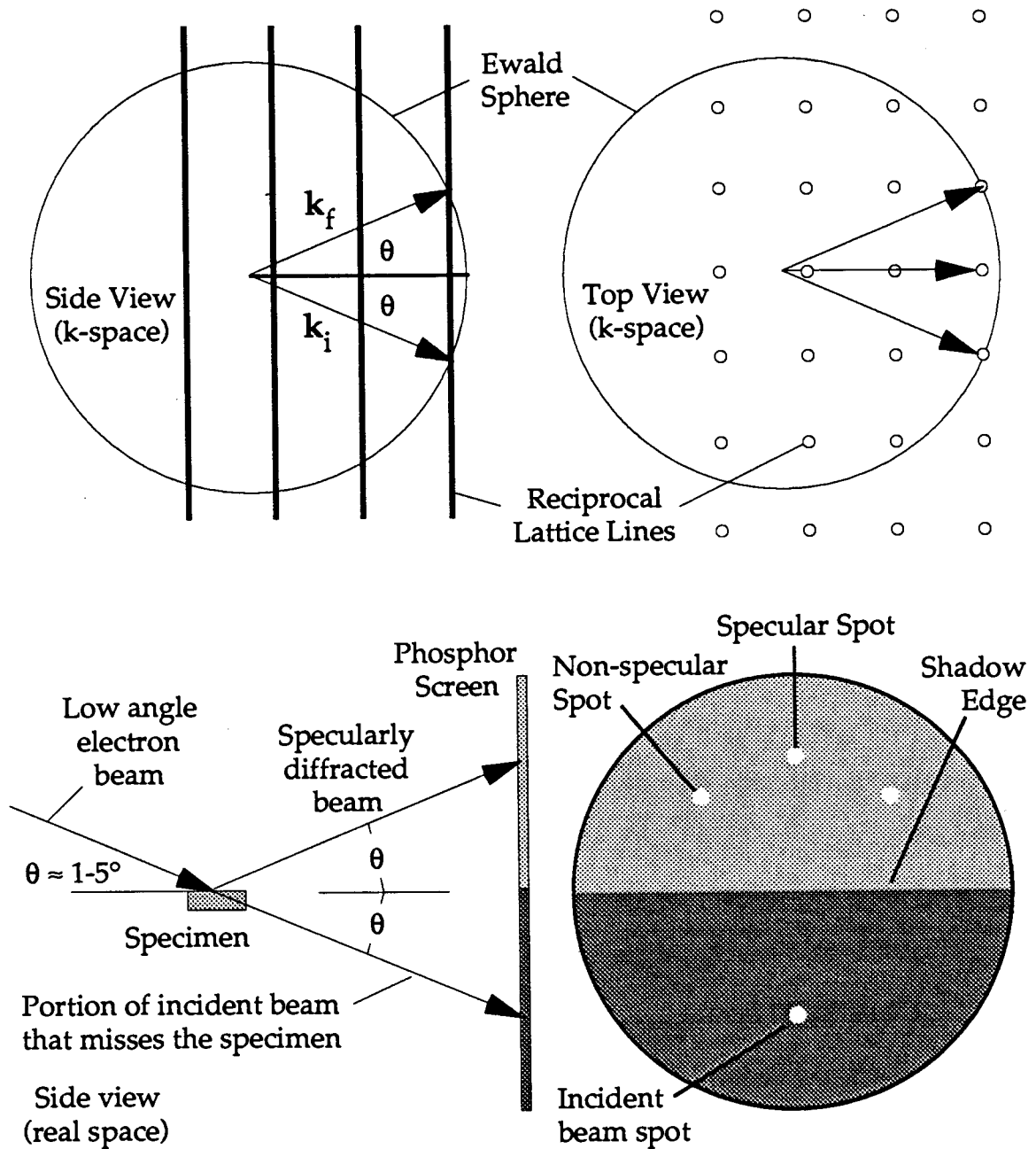


Fig. 2.7. Ewald's construction for RHEED diffraction from a perfectly flat cubic crystal. The low angle RHEED beam in the k_i direction is reflected in the directions k_f which coincide with the intersection of the Ewald Sphere and the reciprocal lattice lines. The resulting RHEED diffraction pattern consists of a set of bright "Ewald spots" set against a dim background of inelastically scattered electrons. The "shadow edge" corresponds to the lowest take off angle from which inelastics can leave the surface. The portion of the electron beam that misses the specimen forms a spot below the shadow edge.

“Perfect” RHEED patterns can very nearly be obtained from (100) surface facets of annealed Fe whiskers. One such pattern is shown in Fig. 2.8(a). Note that the incident beam spot has been obscured in the photo and that the very dark background makes the shadow edge undetectable. Fe whiskers are grown by CVD (chemical vapor deposition). Their surfaces are virtually perfect and flat over areas approximately 0.1mm wide. Fe Whiskers can serve as ideal substrates for RHEED growth studies where it's important to have a reproducible starting surface.

2.6.3 The effect of surface disorder: RHEED Streaks

In general, neither the reciprocal lattice rods nor the Ewald sphere are infinitely thin and well defined. Lattice imperfections and thermal vibrations create surface disorder that causes the reciprocal lattice rods to be characterized by a finite thickness. For example, a “mosaic” specimen composed of many crystallites whose orientation varies slightly, and randomly, from grain to grain, will have reciprocal lattice rods of thickness $2\pi/\Lambda$, where Λ is the average domain size. The finite thickness of the Ewald sphere arises from the spread of incident electron energies and imperfect beam convergence. As a result, the Ewald sphere intersects the thickened reciprocal lattice rods along a portion of their length. The result is a set of long RHEED “streaks” instead of a set of well defined Ewald spots. This is shown in Fig. 2.9 for the case of a square surface net of atoms. The RHEED streaks of a highly ordered surface will be very short and narrow and the RHEED pattern will closely resemble that of a perfect crystal, see Fig. 2.8(a). With increasing disorder, the RHEED streaks lengthen and widen, eventually forming thick, diffuse lines that extend all the way from the shadow edge to the top of the phosphor screen – even when the incident beam angle is less than 1° . Fig. 2.8(b) demonstrates this for the case of a bulk Ag substrate with a 20 mrad mosaic spread.

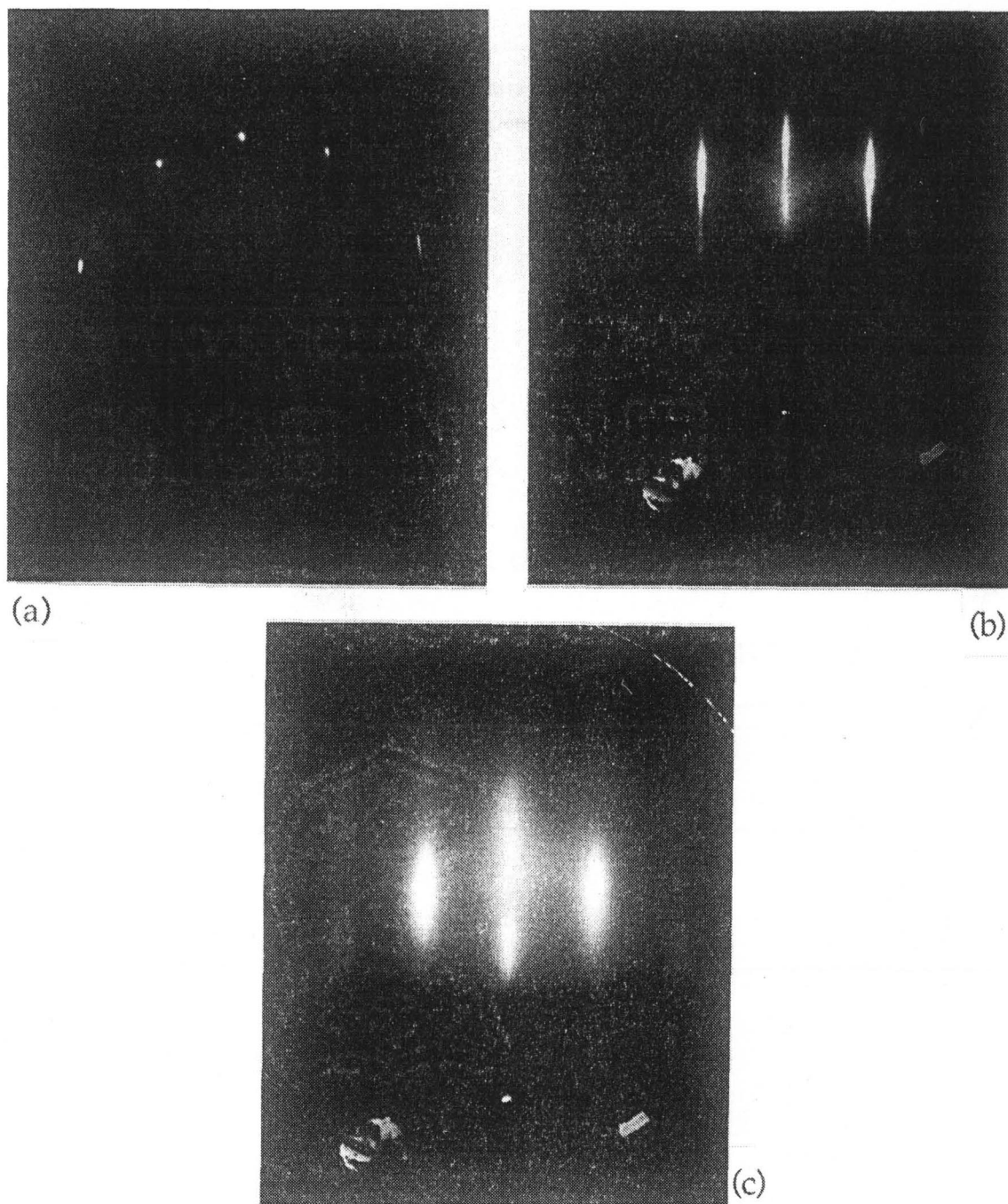


Fig. 2.8. Several representative RHEED patterns illustrating the effect of increasing surface disorder: (a) The pattern of a nearly perfect (001) surface of an Fe(001) whisker facet. (b) The pattern of a bulk Ag substrate with a 20 mrad mosaic spread and misaligned by 2.5° from the (001) plane. (c) The pattern of a 5 ML Fe film grown on top of a bulk Ag(001) single crystal. The breaks along the central streak indicates the presence of three dimensional surface structure.

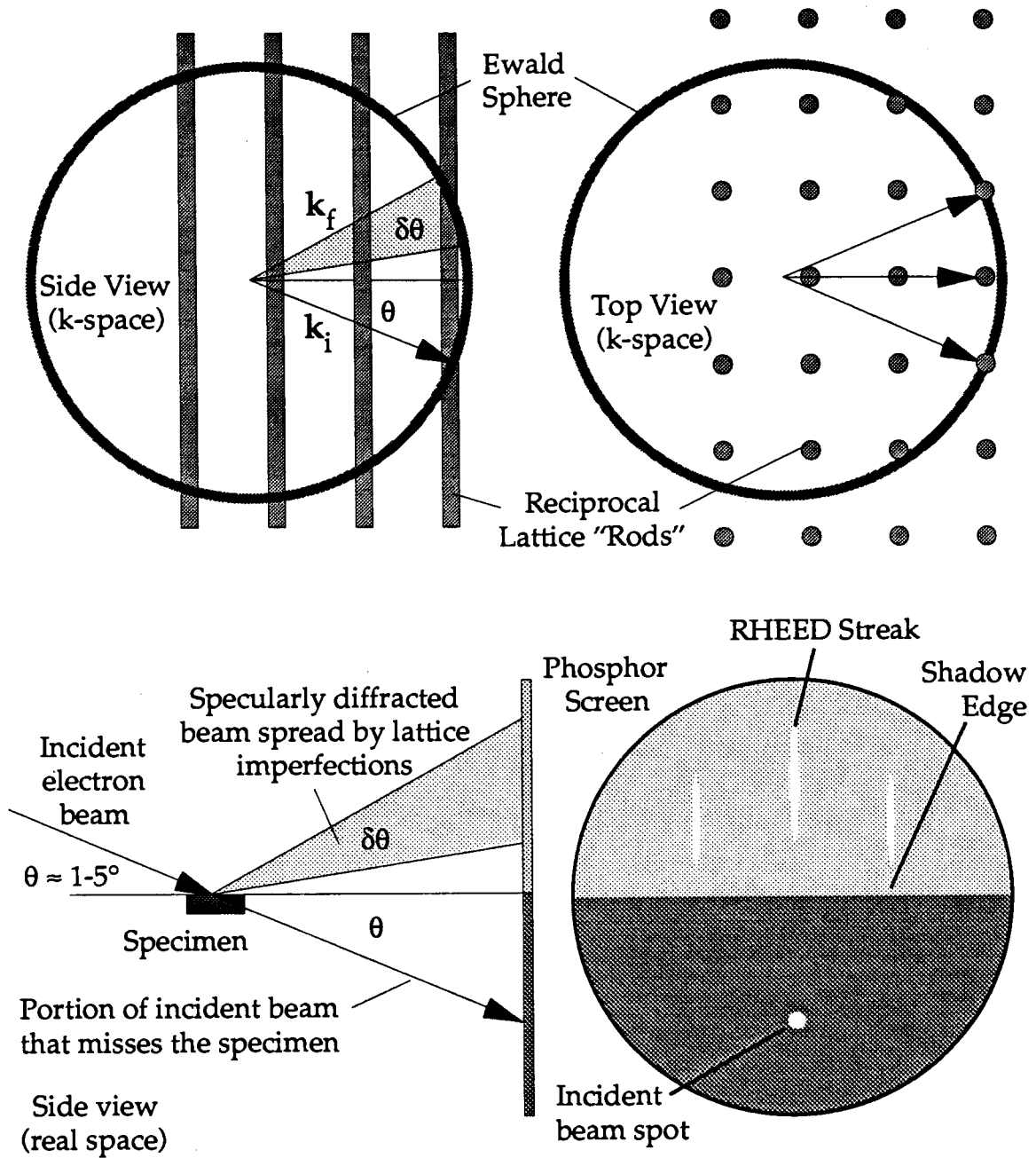


Fig. 2.9. Ewald's construction for RHEED diffraction from a disordered cubic crystal surface. Lattice imperfections and electron energy spread thicken the reciprocal lattice rods and the Ewald sphere such that constructive interference can occur along a portion of each rod that intersects the sphere. The result is a streaked diffraction pattern rather than a set of sharp spots as in the case of a perfectly flat surface (cf. Fig. 2.7). An increase in the number of inelastically scattered electrons by the disordered surface also tends to increase the background intensity above the shadow edge.

2.6.4 Determination of the surface lattice structure with RHEED

The spacing between adjacent RHEED streaks reflects the periodicity of the surface lattice and can be used to determine the basic shape and size of the surface unit cell. As shown in Fig. 2.10, if the distance between the crystal and the RHEED screen is "L", and the spacing between adjacent RHEED streaks is "t", then the periodicity along the in-plane direction perpendicular to the beam direction is given by the simple relation:

$$a = \lambda \frac{L}{t} \quad (2.1)$$

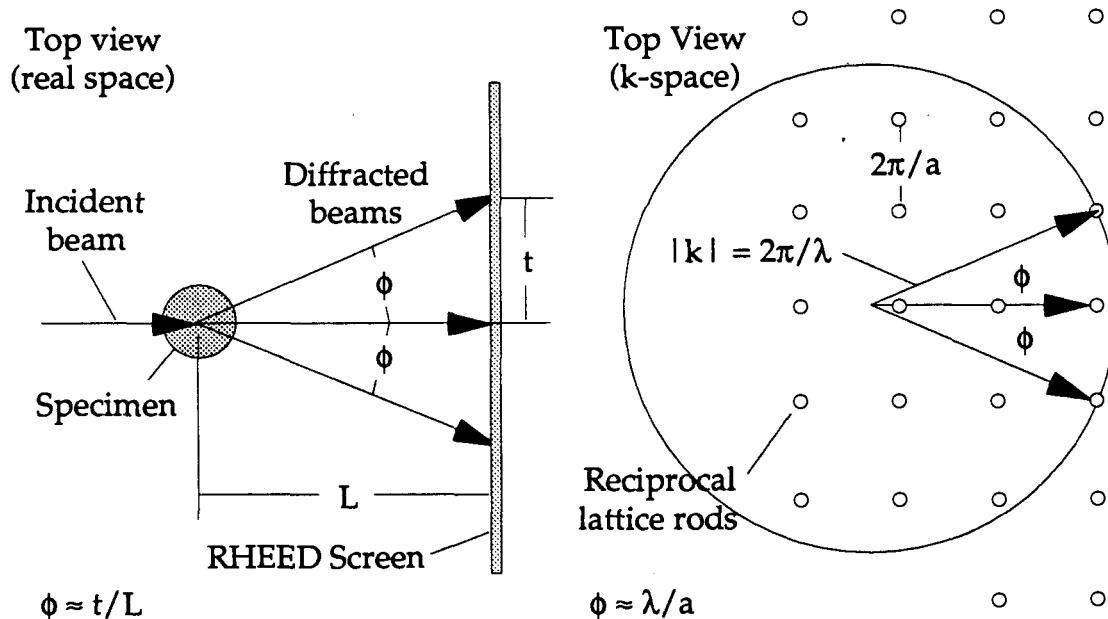


Fig. 2.10. RHEED determination of the dimensions of the surface unit cell. The spacing, t , between adjacent RHEED streaks on the phosphor screen located a distance L from the specimen is proportional to the spacing, a , between adjacent atoms on the surface of the crystal. Equating the small angles, ϕ , in the real space and k-space representations yields $a = \lambda L/t$. Typically, $a/\lambda = (2\pi/\lambda)/(2\pi/a) \approx 15$ to 30 .

2.6.5 The effect of three dimensional surface features

If the surface of a crystal possesses three dimensional structure, several effects can be observed in the corresponding RHEED pattern. The most common effect occurs when the surface is covered with three dimensional islands (or "asperites") due, for example, to poor layer by layer film growth. If the asperites are high enough to intercept part of the incident electron beam, the beam will see a three dimensional lattice and the RHEED streaks will break up to form a spot pattern. This is shown in Fig. 2.8(c) for an Fe(001) film grown on the Ag(001) bulk substrate of Fig. 2.8(b). A striking effect occurs if the asperites have a preferred shape such as that shown in Fig. 2.11. When the surface exhibits pyramidal "facets" (long pyramidal structures that can occur during growth on a rough surface), the resulting pattern will contain sharp, bright "chevrons" or "arrow heads" characteristic of facets (Pukite, 1988). Breaks in the RHEED streaks or the presence of facets are strong indications that a film has not grown layer by layer and that the surface of the specimen is quite rough on the atomic scale. The extreme sensitivity of

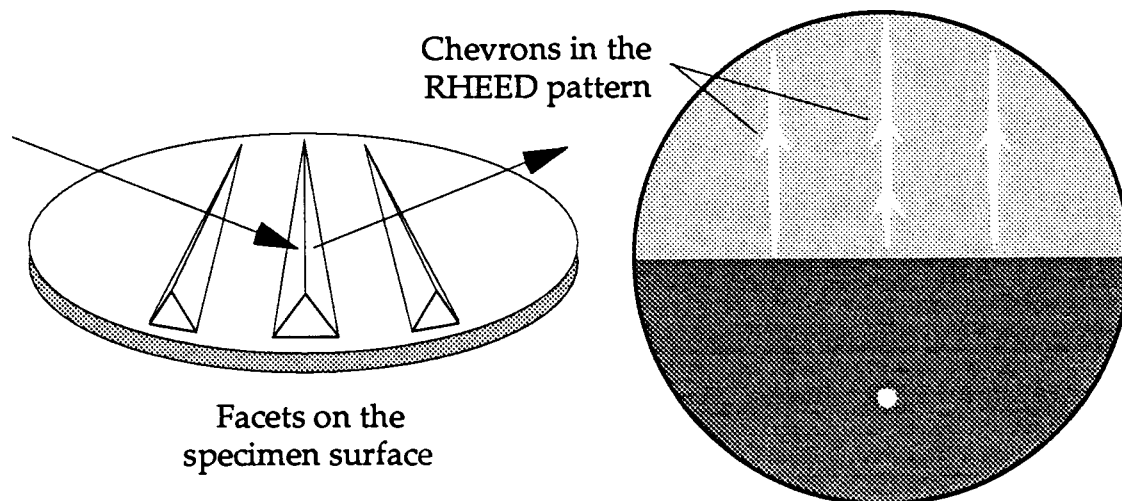


Fig. 2.11. The formation of "chevrons" in a RHEED diffraction pattern due to faceting of the specimen surface. Chevrons indicate the presence of ordered, long range three dimensional structures.

RHEED will show three dimensional surface structures that are only one monolayer higher than the rest of the surface. Such small scale features lead to intensity variations along the length of RHEED streaks (Cohen et al., 1987).

2.6.6 RHEED Oscillations: a measure of layer by layer growth

The intensity of a RHEED pattern can exhibit oscillatory behavior during film growth if the film is growing approximately one atomic layer at a time (Neave et al., 1983, Van Hove et al., 1983, Purcell et al., 1987, 1988a). This behavior can be exploited in two ways. Firstly, it can be used to determine if a given film grows layer by layer on a substrate (such a growth mode is essential to grow well defined films possessing sharp interfaces). Secondly, if a film grows layer by layer and at a constant rate, RHEED oscillations can be used to determine the thickness of the film.

RHEED oscillations are related to changes in the surface roughness during growth. Consider the growth of a single monolayer on top of a perfectly flat surface. Prior to growth, the surface is smooth and the specularly reflected beam will have a high intensity. Opening a furnace shutter to initiate growth creates islands of atoms which grow in lateral size at random positions on the surface. As more atoms arrive, the reflectivity of the surface will decrease as roughness sets in to spoil the previously perfect surface. The islands eventually grow together and reform a smooth surface layer, returning the intensity of the specularly reflected beam to it's initial high intensity. It should therefore be expected that the reflectivity will go through a minimum at 50% coverage. As successive layers grow, the specular spot on the RHEED pattern will go through successive maxima and minima in intensity. If a perfectly smooth surface does not reform at the end of each monolayer due, for example, to incomplete filling in of the monolayer before growth of the next layer begins, then the intensity will not fully recover after

each layer and the intensity oscillations will become smaller as the film grows in thickness. In the limit in which growth does not proceed in a layer by layer fashion, RHEED intensity oscillations will not occur and a 3-d RHEED pattern will develop.

A simple model of RHEED oscillation is shown in Fig. 2.12. A monolayer of material is growing on top of a single crystal substrate. The separation between the substrate and monolayer is d and incident electron waves are characterized by a wave-vector $k = 2\pi/\lambda$. Let the amplitude, ψ_1 , of the specular beam reflected by the growing monolayer be proportional to C , the fraction of the substrate covered by the growing monolayer. For layer by layer growth, C may be assumed to be a "sawtooth" periodic function of time, repeatedly increasing from 0 to 1 with one period equal to the time needed to grow one monolayer. The amplitude, ψ_0 , of the wave reflected by the substrate will be proportional to $(1-C)$, the amount of the substrate still uncovered, and will depend upon the phase factor, $\Delta = 2kdsin\theta$, that accounts for the path difference between ψ_0 and

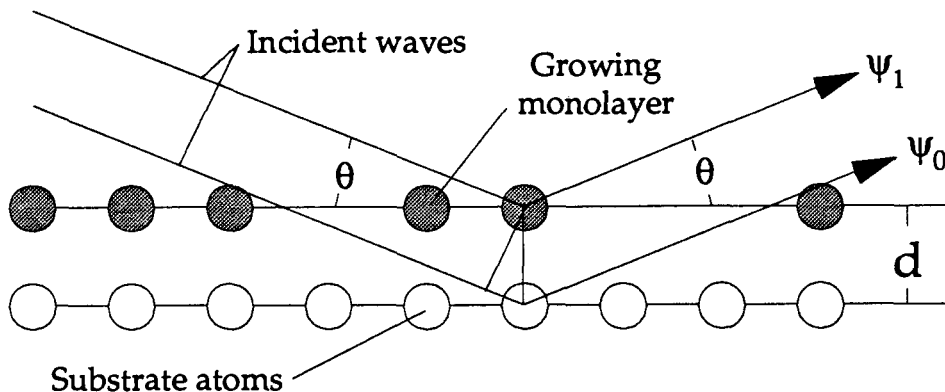


Fig. 2.12. Kinematic model for RHEED Oscillations. The path difference between the waves specularly scattered from the substrate and the growing monolayer gives rise to a variation in the intensity, I , of the net diffracted beam. Here d is the separation between adjacent monolayers and θ is the angle of incidence (and angle of reflection) of the electron waves. The path difference between the waves ψ_0 and ψ_1 is $\Delta = 2kdsin\theta$.

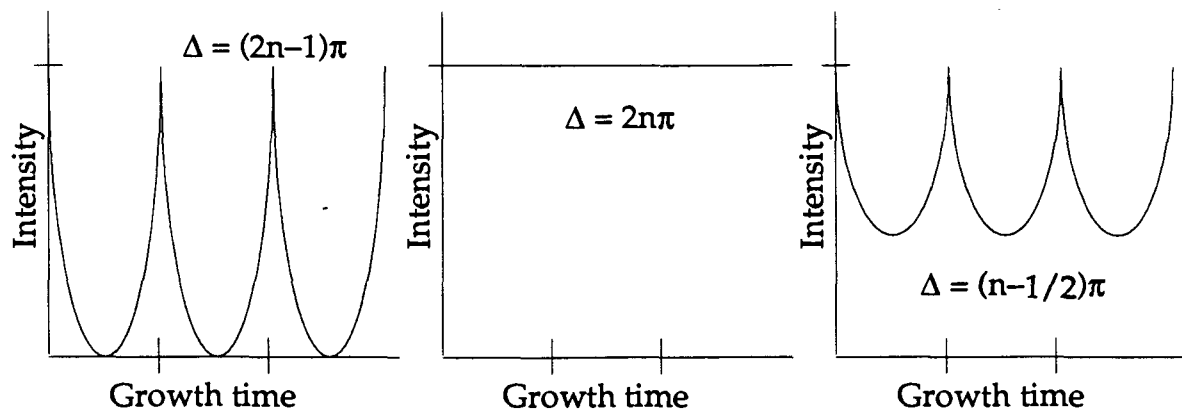


Fig. 2.13. Behavior of RHEED intensity oscillations of the specular beam as a function of the path difference, $\Delta = 2kdsin\theta$, between the electron waves specularly scattered from a substrate and the monolayer growing on top of it (see Fig. 2.12). No oscillations occur when $\Delta=2n\pi$ and the waves are in phase (the Bragg diffraction condition). Maximum oscillations occur when $\Delta=(2n-1)\pi$ (the anti-Bragg condition).

ψ_1 . The net amplitude, ψ , of the specular beam is proportional to

$$\psi = \psi_1 + \psi_0 \propto C + (1 - C)e^{i\Delta}; \quad \Delta = 2kd \sin\theta \quad (2.2)$$

and the resulting intensity of the specular beam is proportional to

$$I = |\psi|^2 \propto C^2 + (1 - C)^2 + 2C(1 - C)\cos(\Delta) \quad (2.3)$$

The value of the phase factor, $\Delta = 2kdsin\theta$, determines the contrast of the intensity oscillations. As shown in Fig. 2.13, there are three cases of interest. When $\Delta = (2n-1)\pi$ (n is an integer), the oscillations will be parabolic in time, reaching a maximum as each monolayer is completed and going through a minimum when each monolayer is half grown. When $\Delta = 2n\pi$, the condition for constructive Bragg interference between the two reflected waves, the intensity will be constant in time. In between these two extre-

ma, some form of parabolic intensity oscillations will be observed with the minimum intensity not going to zero at 50% coverage.

2.6.7 Measuring film thickness with RHEED

RHEED oscillations can be used to accurately determine the thickness of a film since the period of one oscillation corresponds to the growth of one monolayer (Purcell et al., 1988). The film thickness is calculated simply by dividing the total growth time by the average period of the regular oscillations. Assuming a constant growth rate, this average time per monolayer can be used to terminate the growth at any desired film thickness.

2.7 Surface Chemical Analysis using AES and XPS

Auger Electron Spectroscopy (AES) and X-ray Photoelectron Spectroscopy (XPS) are quantitative surface analysis tools capable of determining the chemical structure of the topmost 10-30Å of a specimen with a detection limit of 0.1% – 1% monolayer (Briggs and Seah, 1983). They were used in our work to determine the purity of the substrates and ultrathin films; AES and XPS intensities were also used to estimate the thickness of many of the ultrathin films (see section 2.7.4).

2.7.1 X-Ray Photoelectron Spectroscopy (XPS)

The XPS, or ESCA*, spectroscopy irradiates a specimen with monoenergetic soft x-rays, typically Mg K_α (1253.6 eV) or Al K_α (1486.6 eV), and collects emitted photoelectrons. The photoelectrons exhibit a distribution in kinetic energy, N(E), which carries information about the chemical composition of the specimen. The photoelectric process is illustrated in Fig. 2.14. An x-ray photon of known energy $h\nu$, enters a specimen and interacts with an inner core electron of an atom whose binding energy, E_b , is less than $h\nu$. The interaction results in the direct transfer of energy to the electron, causing the latter to be ejected from the atom. If the electron escapes from the specimen without further energy loss, it will have a kinetic energy characteristic of the photon energy and of the parent atom.

The kinetic energy, E , of emitted photoelectrons is determined by conservation of energy:

$$E = h\nu - E_b - \phi_s \quad (2.4)$$

* ESCA: Electron Spectroscopy for Chemical Analysis

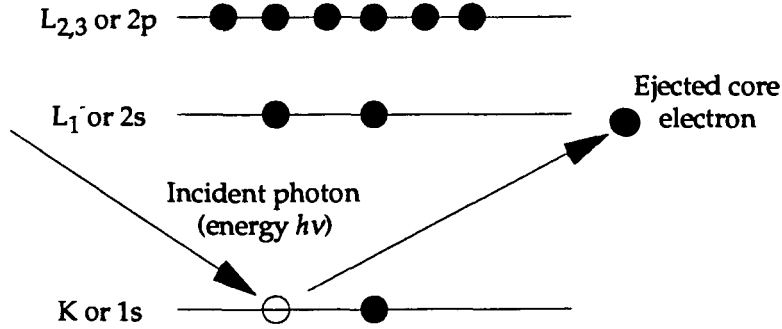


Fig. 2.14. The Photoemission process utilized in XPS. An incident x-ray photon is absorbed by an inner core electron of an atom, causing it to be ejected from the atom. The kinetic energy of the electron is determined by the energy of the x-ray photon and the binding energy of the core level.

where E is the kinetic energy of the photoelectron assuming no energy loss due to collisions with other atoms in the specimen, $h\nu$ is the known energy of the incident x-ray photon, E_b is the binding energy of the core level from which the electron originated, and ϕ_s is the work function of the material (approximately 5 eV in most solids).

An XPS spectrometer uses an energy analyzer, such as the double pass Cylindrical Mirror Analyzer described in section 2.7.3, to collect the emitted photoelectrons and to measure their kinetic energies. The electronics associated with the analyzer automatically compensates for the specimen work function and subtracts off the incident x-ray energy. This allows electron energy spectra to be obtained in the form of the number of electrons, $N(E_b)$, collected at a given atomic binding energy, E_b . The XPS spectrum for a bulk silver substrate is shown in Fig. 2.15. Electrons originating from the Ag $3d_{5/2}$ level give rise to a peak at a binding energy of 368 eV. The peaks located at binding energies above 850 eV are due to Auger electrons emitted from the specimen by the Auger process described in the next section. They are of limited use in XPS, serving mainly to

identity an element whose primary photoelectron peak(s) are obscured by the peaks of other elements.

Most elements contribute several different peaks to an XPS spectrum, each peak being labelled in spectroscopic notation according to the core level from which the photoelectrons were ejected from. Elemental identification is readily carried out by comparison with standard elemental spectra such as those found in the PHI Handbook on XPS spectra (Wagner et al., 1979). XPS spectra are very useful for qualitative identification of various compounds and oxides on a specimen surface. See the PHI XPS Handbook (Wagner et al., 1979) for details.

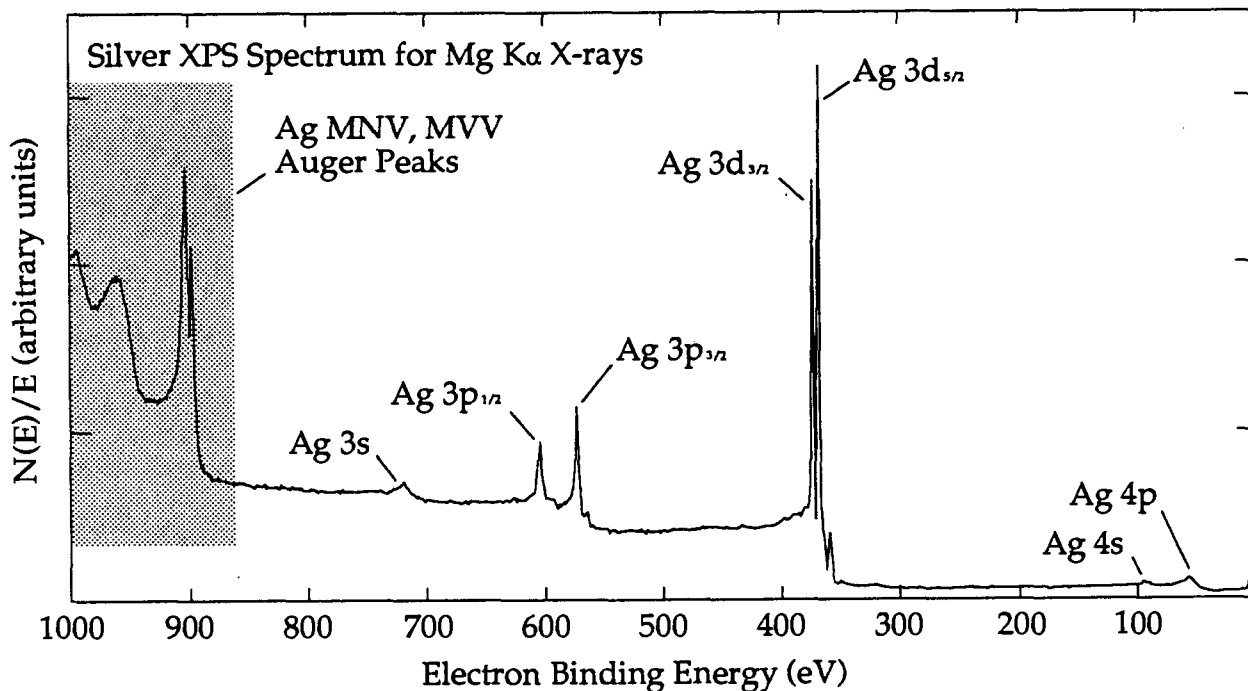


Fig. 2.15. The XPS spectrum of a bulk Ag substrate. Photoelectrons emitted from the specimen give rise to peaks in the secondary electron distribution function $N(E)$. The position of the peaks identify the elements on the surface. The sloping background is due to electrons that suffered energy loss through inelastic collisions before leaving the specimen.

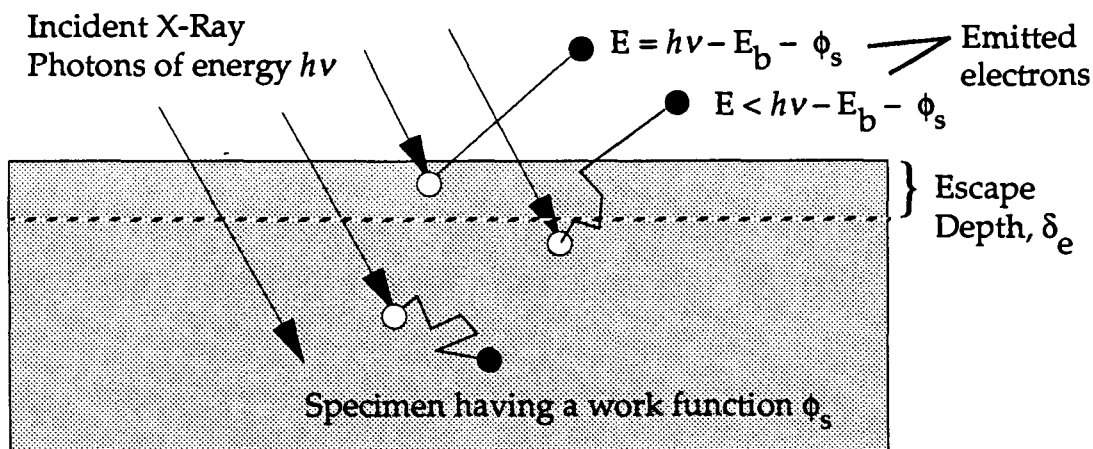


Fig. 2.16. XPS uses x-ray photons to stimulate electron emission from a specimen. The short inelastic mean free path of an electron in a solid allows only electrons located within the "escape depth" to emerge from the specimen without energy loss. Typical escape depths in metals range from 10 to 30Å.

XPS is a surface sensitive technique because the photoelectrons must leave the specimen unchanged in energy in order to contribute to an XPS peak. If an electron is inelastically scattered and loses some of its energy between the time of its emission from an atom and the time it enters the energy analyzer, they are lost in terms of providing chemical information and contribute only to the continuous background signal shown in Fig. 2.15. Since electrons can only travel a short distance in a solid before being inelastically scattered, only those that originate near the surface can contribute to a peak in an XPS spectrum. This is illustrated in Fig. 2.16. The average depth from which electrons can escape without scattering is termed the "escape depth", δ_e . The escape depth has been shown to depend primarily on the kinetic energy of an electron and on the number density (atoms per unit volume) of the solid. One measure of the escape depth is provided by the inelastic mean free path (IMFP), λ_M , defined to be the average distance an electron can travel in a solid before being inelastically scattered. More precise-

ly, an electron has a probability of e^{-1} of travelling a distance λ_M before scattering. It follows that a given flux, I_0 of monoenergetic photoelectrons will decay in intensity by the factor of $\exp(-l/\lambda_M)$ after having travelled a distance l in the solid.

A convenient definition of the escape depth, δ_e for electrons travelling at some angle of inclination α to the specimen plane is therefore

$$\delta_e \approx 3\lambda_M \sin(\alpha) \quad (2.5)$$

since electrons travelling a distance $3\lambda_M$ in the specimen have a 95% chance of being scattered.* Most of the emitted electrons will have travelled a shorter distance than δ_e .

By fitting experimental data to several empirical functions, Seah and Dench (1981) have shown that the IMFP of electrons in most pure elements can be adequately described by the simple equation:

$$\lambda_M = \frac{538}{n^{1/3} E^2} + 0.41 \sqrt{\frac{E}{n}} \quad (2.6)$$

where λ_M is expressed in nm, "E" is the electron kinetic energy in eV, and "n" is the number density of the element expressed in atoms/(nm)³. A typical XPS photoelectron has a kinetic energy of 500 eV (Wagner et al., 1979). Such electrons travelling through transition metals whose number densities are of the order of 70 atoms/nm³ will have a mean free path of approximately 10Å. This implies a maximum escape depth of approximately 30Å. This is the maximum depth that can be probed in most metallic specimens using XPS or AES.

* Electrons emitted at a depth of $\delta_e = 3\lambda_M$ have a probability of $[1 - \exp(-3)] \approx 0.95$ of scattering before reaching the surface.

2.7.2 Auger Electron Spectroscopy (AES)

Auger Electron Spectroscopy bombards a specimen with a 2–10 keV electron beam and collects the electrons emitted by the Auger process illustrated in Fig. 2.17. The Auger electrons exhibit a distribution in kinetic energy, $N(E)$, which carries information about the chemical composition of the specimen. The Auger process occurs in two steps: first, an electron from the incident beam collides with an atomic inner core electron, such as the K-shell electron shown in Fig. 2.17(a), and knocks the electron out of the atom. Approximately 10^{-14} seconds later, the atom relaxes through a process that fills the vacant state with an electron from a higher shell such as the L-shell shown in Fig. 2.17(b). Most of the time the energy given up by the relaxing electron is transferred to another electron (the Auger electron) which is then ejected from the atom. The energy could also go into the creation of an x-ray photon (x-ray fluorescence) but this competing process is a minor one, and occurs less than 1% of the time (Wagner et al., 1979).

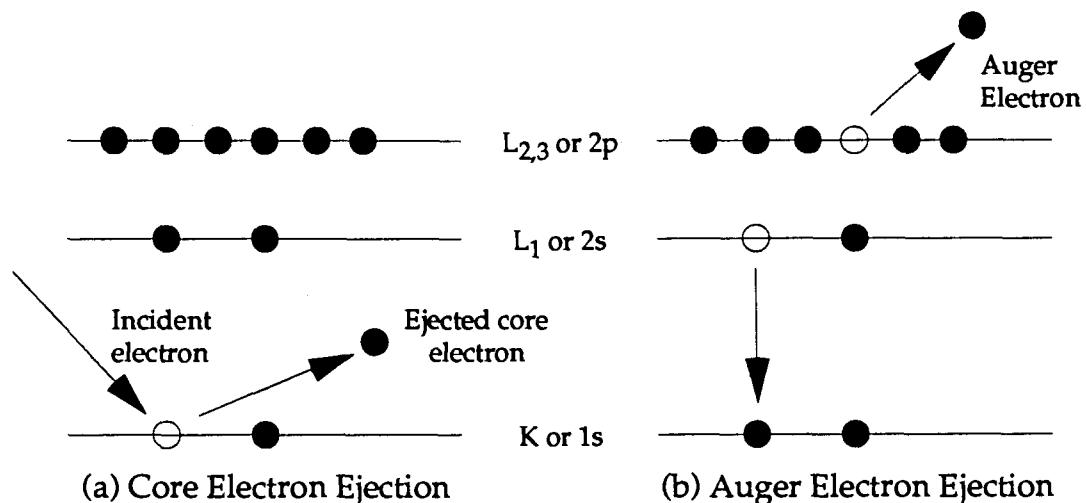


Fig. 2.17. Diagram of the Auger process. (a) An incident photon or electron ionizes a core electron. (b) A higher energy electron relaxes into the vacant state, giving part of its energy to another electron in a nearby orbital. The latter electron can receive enough energy to escape the atom.

The kinetic energy, E , of an Auger electron is characteristic of the parent atom so that Auger electrons emitted close enough to the surface to escape without energy loss can be used to identify chemical species. To a first approximation, the kinetic energy, E , is given by

$$E = E_c - E_r - E_A \quad (2.7)$$

where E_c is the (positive) binding energy of the core electron originally knocked out of the atom, E_r is the (positive) binding energy of the relaxing electron, and E_A is the (positive) binding energy of the Auger electron. Equation (2.7) is approximate in the sense that it ignores energy shifts in the core levels due, for example, to the presence of the vacant states during the relaxation and Auger emission processes. These shifts have been discussed in some detail by Briggs and Rivière (1983) and are usually expressed as one or more small energy correction terms added to (2.7).

Auger electrons are labelled according to the atomic levels involved in the emission process. For example, the Auger electron emitted in Fig. 2.17(b) would be labelled $KL_1L_{2,3}$. Auger electrons need not come from the same shell as the relaxing electron. They can just as easily come from any higher shell, even the valence band. Thus, it's possible for an atom with the atomic levels shown in Fig. 2.17 also to emit KL_1L_1 , $KL_{2,3}L_{2,3}$, $L_1L_{2,3}L_{2,3}$, or KL_1V Auger electrons (the letter V indicating that the Auger electron was ejected from the valence band).

Every Auger process has a certain probability of occurrence; most elements favor one or two particular transitions. The most probable transition (the principle transition) is used to identify a given element. The Auger electrons collected by means of an AES spectrometer contribute a set of characteristic peaks to the secondary electron distribu-

tion function, $N(E)$, which is defined to be the number of electrons having kinetic energy between E and $E+\Delta E$ collected by the spectrometer. The energy range depends on the AES system and is discussed in the next section. Many Auger peaks in $N(E)$ tend to be rather small in amplitude compared with the background signal due to inelastically scattered electrons. In order to emphasize the Auger peaks, it has become standard practice to differentiate $N(E)$ with respect to E and to use $dN(E)/dE$ to display Auger spectra. The differentiation is usually accomplished electronically during data collection, see section 2.7.3 for details.

A typical AES derivative spectrum for an oxidized Ag substrate is shown in Fig. 2.18. The peak positions denote Auger transitions unique to Ag and to oxygen and can therefore be used to identify the elements unambiguously. Most elements can be readily identified by comparing the positions of unknown peaks with those of published standard spectra. One good source of such spectra is the PHI AES handbook (Davis et al., 1979). The peak position and shape provides chemical information about the bonding between elements on a specimen surface. The peak height is proportional to the number of electrons collected having a particular kinetic energy which, in turn, is proportional to the concentration of a particular element in the analysis volume. This latter fact makes determination of relative elemental concentrations by means of AES a rather straightforward task. The only small complication is that the efficiency of the Auger process varies with both atomic number and the intensity of the incident electron beam. This variation in sensitivity is accounted for by "atomic sensitivity factors" empirically determined for the principle Auger transition of most elements using standard specimens. This information is usually supplied for a given spectrometer by the manufacturer.

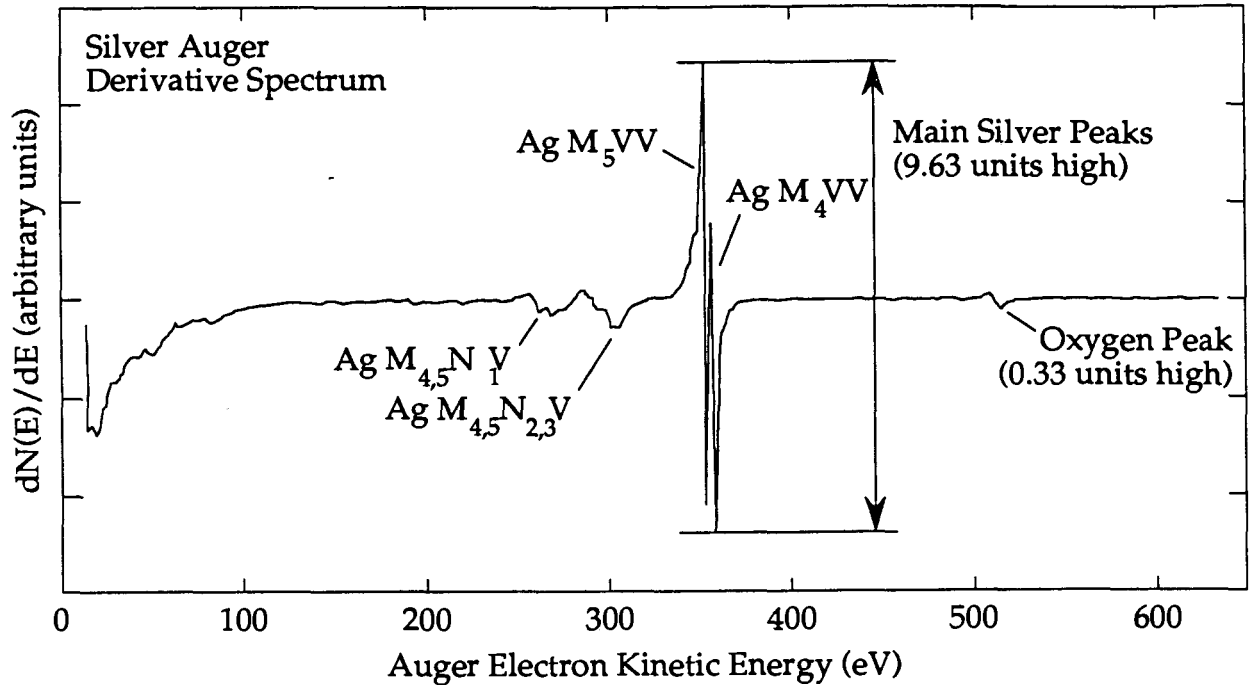


Fig. 2.18. The derivative Auger spectrum of an oxidized bulk Ag(001) substrate. Auger spectra can be used for quantitative chemical analysis because each element produces a unique set of Auger peaks and the "height" of any given peak is proportional to the surface concentration of the element producing it.

Consider the problem of the determination of the amount of oxygen present on the Ag substrate whose Auger spectrum is shown in Fig. 2.18. The spectrum was collected with a PHI AES system and an incident electron beam energy of 3 keV. The principle oxygen and silver Auger peak heights are in the ratio 1:29. For a 3 keV beam energy, the PHI spectrometer has an oxygen sensitivity factor of 0.35 and a silver sensitivity factor of 1.0 (silver is used as the standard reference for PHI spectrometers – Davis et al., 1979). The ratio of Oxygen atoms to Ag atoms on the surface of the specimen is therefore $(1+0.35)$ to $(29+1.0)$ or 1 to 10 (ie, roughly one oxygen atom for every 10 silver

atom). Note that this information could just as well have been obtained from an XPS spectra of the silver substrate using similar techniques (see, Wagner et al., 1979).

Like XPS, the surface sensitivity of AES is related to the escape depth, δ_e , of Auger electrons or, equivalently, the inelastic mean free path, λ_M , of Auger electrons in a solid. The value of λ_M for Auger electrons travelling through an element is the same as that for photoelectrons of the same kinetic energy and can be calculated using equation (2.6). Typical kinetic energies of Auger electrons lie in the 100–500 eV range. Such electrons travelling through transition and noble metals ($n \approx 70$ atoms/nm³) are characterized by mean free paths $\lambda_M \approx 5\text{--}10\text{\AA}$ so that AES can be used to analyze the 15–30Å layer near the surface.

2.7.3 AES and XPS Spectrometers

The AES and XPS spectrometers available in the PHI Model 400 MBE machine are housed near the top of the analysis chamber as shown in Fig. 2.1. A more detailed, cut-away view is shown in Fig. 2.19. Both spectrometers are built around a “double pass” Cylindrical Mirror Analyzer (CMA), part of the PHI Model 15-255GAR Precision Energy Analyzer system. The electron gun used for AES is mounted inside the CMA. The 2–10 keV electron beam could be focussed to a 0.2 mm spot for detailed surface chemical analysis. The x-ray gun used for XPS is mounted on the side of the analysis chamber. The PHI Model 04-548 Mg/Al X-Ray gun used 10 keV electrons to bombard a water-cooled Mg or Al target to produce K_α X-Rays. The Al K_α line has an energy of 1486.6 eV and a line width of 0.8 eV. The Mg K_α line has an energy of 1253.6 eV and a line width of 0.7 eV. The Mg line was chosen for most of our work.

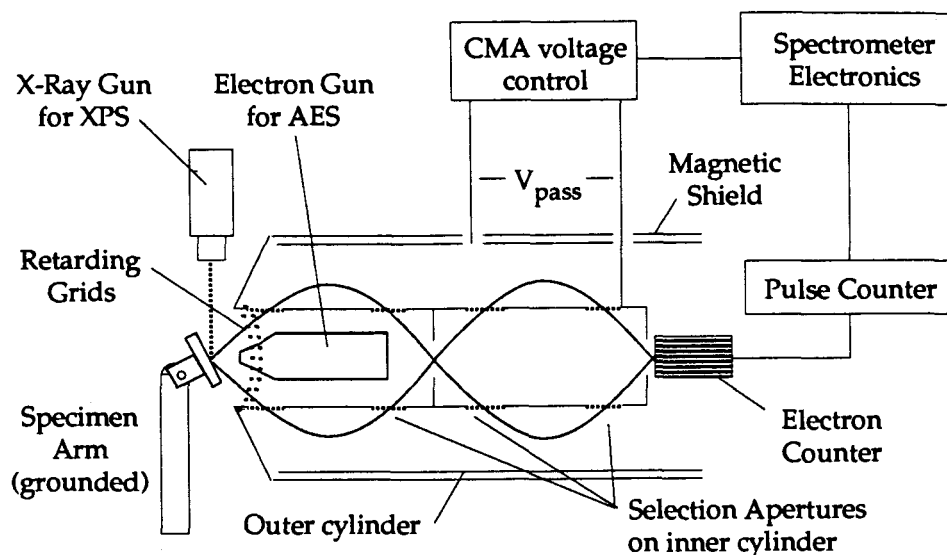


Fig. 2.19. Cross section of the PHI Model 15-110 double-pass Cylindrical Mirror Analyzer (CMA) mounted at the top of the analysis chamber of a PHI Model 400 MBE facility (see Fig. 2.1). The CMA analyzes the energy of electrons emitted from a specimen under bombardment by electrons (for Auger Electron Spectroscopy) or by X-Rays (for X-Ray Photoelectron Spectroscopy).

The PHI Model 15-110 double pass CMA was used to collect and analyze the secondary electrons emitted from the specimen under excitation by x-rays (XPS) or electrons (AES). The CMA acts as a “velocity selector” and allows electrons of one kinetic energy to pass through the instrument to an electron counter (see Fig. 2.19). Electrons emitted from a specimen enter the CMA through an annular “acceptance aperture” surrounding the AES gun. The aperture allows only electrons which leave the specimen surface at specific “acceptance angles” to enter the CMA (see Figs. 2.19 and 2.21). Once inside the CMA, a potential difference, V_{pass} , maintained between an inner metal cylinder and the outer wall sets up an electrostatic field which allows electrons of only one specific “pass energy”, E_{pass} , to traverse a helical trajectory through sets of “selection

apertures" in the inner cylinder to an electron detector where they were recorded by external counting electronics. For the PHI model 15-110 CMA, the pass energy was related to the potential of the outer cylinder by the relation $E_{\text{pass}} \approx 1.7eV_{\text{pass}}$. The output from the counting electronics was the "secondary electron distribution function", $N(E)$, defined to be the number of electrons emitted by the specimen having kinetic energy between E and $E+\Delta E$.

XPS spectra were collected by setting the CMA to pass a certain electron energy, E . Retarding grids at the entrance to the CMA were used to vary the energy of the electrons entering the CMA. The relative resolution, $\Delta E/E$, of a CMA is fixed so that this procedure yielded a constant energy resolution, ΔE , across the entire scan range and resulted in an improved resolution at energies in excess of the pass energy. The PHI Model 10-155 CMA used in this work could be set for pass energies of 25, 50, or 100 eV providing energy resolutions better than $\Delta E \leq 1$ eV.

The specimen geometry, the mode of operation of the CMA, and the resulting energy resolution differs for AES and XPS. The specimen AES geometry is shown in Fig. 2.20. The specimen is normal to the axis of the CMA and at the focus of the electron gun. In this position, the CMA will accept electrons that leave the specimen surface at an "acceptance angle" of approximately 42° . This results in an effective Auger electron escape depth of approximately $3\lambda_M \sin(42^\circ) = 2\lambda_M$ where λ_M is the inelastic mean free path. As mentioned in section 2.7.2, the Auger yield from a typical specimen is rather small compared with the large number of inelastically scattered electrons leaving the surface. As a result, the Auger peaks in the secondary electron energy distribution function $N(E)$ measured by the CMA tend to be rather small compared with the continuous inelastic background. In order to make the Auger peaks stand out, it has become

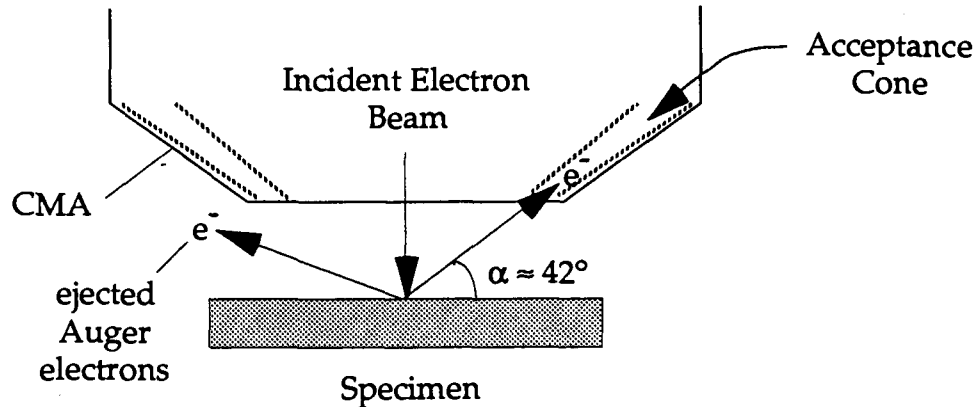


Fig. 2.20. The AES geometry. The double pass CMA shown in Fig. 2.21 accepts electrons through an annular opening surrounding the internal electron gun. When a specimen is at the focus of the gun, the CMA will accept electrons leaving the surface at an "acceptance angle", α , of approximately 42° with respect to the specimen plane.

standard practice to differentiate $N(E)$ with respect to electron kinetic energy, E . In order to obtain a signal proportional to the derivative of the electron density function $N(E)$ a small ac modulation signal of frequency f_m is superposed on the dc pass potential V_{pass} . The output signal component at the modulation frequency, f_m , is proportional to $dN(E)/dE$, and can be readily measured by means of a lock-in amplifier.

When operating in AES mode, the relative energy resolution, $\Delta E/E$, of the PHI 10-155 CMA was approximately 0.006. Given that the principle Auger transition of any element above helium produces Auger electrons in the 0-2 keV energy range, spectral features larger than 12eV could be resolved. This was about an order of magnitude larger than the energy resolution of the CMA when operating in XPS mode ($\Delta E \approx 1\text{eV}$)

The specimen geometry for XPS is shown in Fig. 2.21. The specimen normal is inclined at an angle of $\phi \approx 40^\circ$ to the CMA axis. This allows the CMA to accept electrons

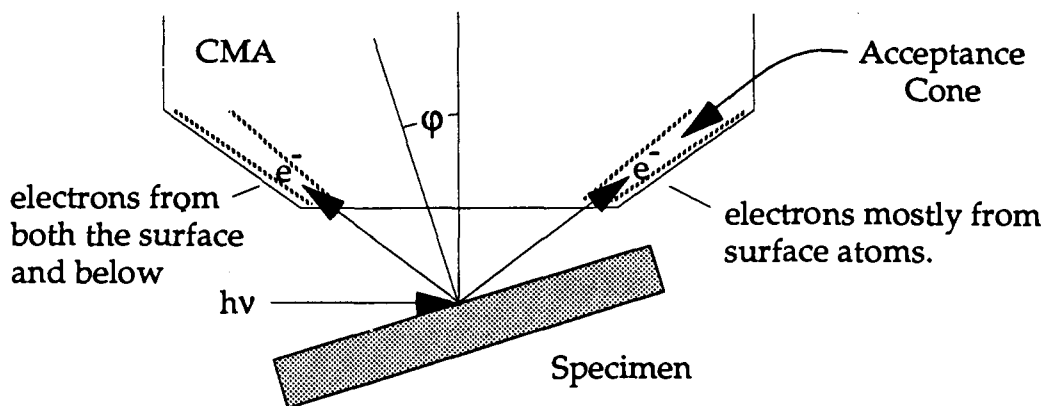


Fig. 2.21. Schematic diagram of the XPS detection geometry. An X-Ray gun mounted perpendicular to the CMA axis irradiates the specimen with x-rays. The X-Ray gun is placed as close to the specimen as possible. The specimen is tilted at $\phi \approx 40^\circ$ to the CMA axis to allow for "angular resolved" XPS studies.

leaving the surface at angles ranging from roughly 2° ($42^\circ - 40^\circ$) to approximately 82° ($42^\circ + 40^\circ$) when the center of the specimen surface is located at the focus of the AES electron gun. The specimen is tilted in order to permit "angular resolved XPS" (ARXPS) studies. ARXPS can be used to determine if a given element is concentrated on the specimen surface, just below the surface, or uniformly distributed throughout the analysis volume. The CMA contains a set of shutters to block the selection apertures located near the electron counter (see Fig. 2.19). Blocking one aperture will allow only the high angle electrons to reach the counter. Blocking the other aperture will pass only the low angle electrons. The high angle electrons can come from any atom located throughout the escape depth of approximately $\delta_e \approx 3\lambda_M \sin(82^\circ) = 2.97\lambda_M$ (see equation 2.5). In comparison, the low angle electrons can come only from electrons located within the escape depth $\delta_e \approx 3\lambda_M \sin(2^\circ) = 0.1\lambda_M$. The finite size of the slits allows electrons in a range of angles around 82° and 2° to be accepted. In the PHI CMA the angular range was approximately $6-12^\circ$.

Comparing the XPS spectra obtained from the high and low acceptance angles allows information about the chemical state both on the surface and throughout the analysis volume to be obtained. One use of ARXPS is in surface segregation studies which seek to determine if substrate atoms have intermixed with atoms of the film. If no intermixing has occurred, there should be no substrate peaks in the low angle XPS spectrum.

2.7.4 Determination of film thickness by means of AES and XPS

AES and XPS can be used to measure the thickness of an ultrathin film *provided* that the film is of uniform thickness. Consider the situation shown in Fig. 2.22. Prior to film growth, the substrate emits a certain flux of Auger electrons, I_0 , proportional to the measured height of the principle Auger peak associated with the substrate (see Fig. 2.18 where the AES spectrum of a silver substrate is shown). Following deposition of a film of thickness d , this Auger signal will decrease to I_c due to inelastic scattering over the extra distance $d/\sin(\alpha)$ that the Auger electrons must now travel through the film. If λ_M is the inelastic mean free path for the substrate Auger electrons in the film then the relative signal decrease is

$$\frac{I_c}{I_0} = \exp\left(-\frac{d}{\lambda_M \sin \alpha}\right) \quad (2.8)$$

Consider the determination of the thickness of a bcc Fe(001) film grown on a Ag(001) substrate. The principle silver Auger peak shown in Fig. 2.18 is due primarily to 352 eV Auger electrons. Equation (2.6) gives the inelastic mean free path of these electrons in iron ($n = 85 \text{ atoms/nm}^3$) to be $\lambda_M = 8.34 \text{ \AA}$. If the principle Ag Auger peak decreases in height by $I_c/I_0 = 0.28$ following growth of the iron film, and the CMA acceptance angle is 42° , then (2.8) shows that the Fe film thickness must be $d = 7.1 \text{ \AA} \approx 5 \text{ ML}$.

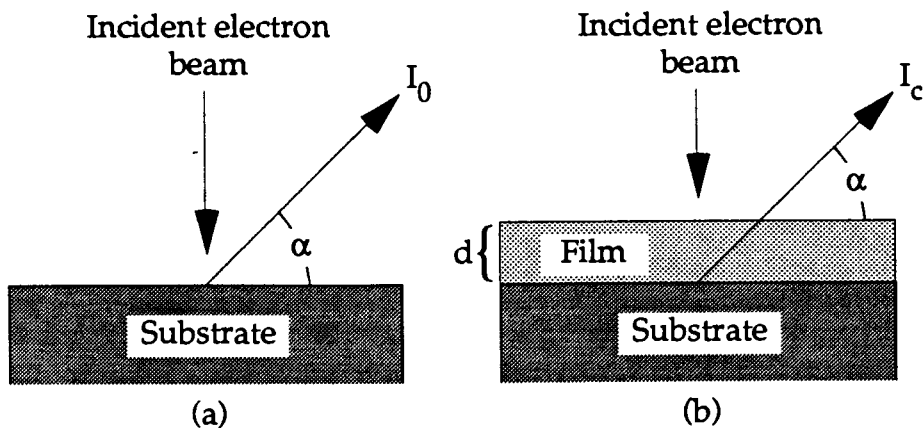


Fig. 2.22. Calculation of film thickness, d , using AES. The Auger electron flux from the substrate decreases after film growth due to the extra distance $d/\sin(\alpha)$ the Auger electrons must travel through the film. Electrons have a probability of $\exp(-1)$ of suffering an inelastic collision after they travel a distance λ_M in the film. Hence, the decrease in the electron flux, I_c/I_0 , due to the presence of the film is just $\exp(-d/\lambda_M \sin(\alpha))$. Here, α is the acceptance angle for AES (see Fig. 2.20).

XPS can also be used to determine the thickness of a film. The thickness equation (2.8) is still valid, the only difference is that the ratio I_c/I_0 should be calculated from the change in the *area* underneath a strong photoelectron peak associated with the substrate *after* the sloping inelastic background signal has been subtracted off. A rougher estimate of I_c/I_0 can be obtained by simply taking the ratio of photoelectron peak heights after background subtraction. Care must be exercised when calculating the inelastic mean free path, λ_M , for photoelectrons. Photoelectron peak energies are usually quoted in terms of *binding energy*, not kinetic energy. The two must not be confused. Equation (2.6) for λ_M requires the use of photoelectron kinetic energy.

The simple exponential signal decay predicted by (2.8) is often observed in practice. See, for example, Fig. 6 in Heinrich et al. (1987a).

2.8 The in situ FMR Spectrometer

FMR in ultrathin iron films used in this investigation was measured at 9.6, 16.88, 36.6, and 73.0 GHz. The 16.88 GHz spectrometer was mounted inside the MBE facility in order to carry out FMR measurements on bare iron films. This spectrometer is described in detail in the next few sections. The other spectrometers were similar in design and identical in operation. They are very briefly described at the end of this chapter. More information on the components of microwave spectrometer systems can be found in the books "Microwave Measurements" by E. L. Ginzton (1957) and "Electron Spin Resonance, A Comprehensive Treatise on Experimental Techniques" by C.P. Poole (1967).

2.8.1 Experimental Measurement of FMR

FMR measurements are typically carried out by immersing a thin slab of the subject metal in a uniform d.c. magnetic field H_0 and irradiating the surface of the slab at normal incidence with microwaves of a fixed frequency $\omega = 2\pi f$. The reflected microwave power is measured as a function of H_0 . The difference between the incident and the reflected power is proportional to the power absorbed by the specimen – the quantity of interest.

Comparison between theory and experiment is simplified if H_0 is oriented either parallel to the specimen plane (parallel configuration) or perpendicular to the plane (perpendicular configuration). The theoretical calculations of Chapter 3 assume the parallel configuration. The microwaves are polarized with the rf magnetic field orthogonal to the d.c. field in either case. With this arrangement the magnetization vector in the slab is pulled into the direction of H_0 and the transverse rf magnetic field drives the

precessional motion of \mathbf{M} . The frequency of the precession, ω_0 , is determined by the strength H_0 and the magnetic properties of the specimen. Ferromagnetic resonance occurs when ω_0 matches the driving microwave frequency ω .

The simplest practical FMR spectrometer that could be used to carry out these measurements is shown in Fig. 2.23. A klystron generates a beam of microwaves that are directed down a waveguide to a specimen placed across the open end. An isolator prevents the reflected microwaves from feeding back into the klystron and distorting its output (Ginzton, 1957). A directional coupler diverts part of the reflected beam to a point-contact diode and a voltage is generated which is proportional to the amplitude of the reflected signal if the reflected power exceeds ~ 1 mWatt (Poole, 1967, Ginzton, 1957). The d.c. diode voltage is measured as a function of the applied field H_0 .

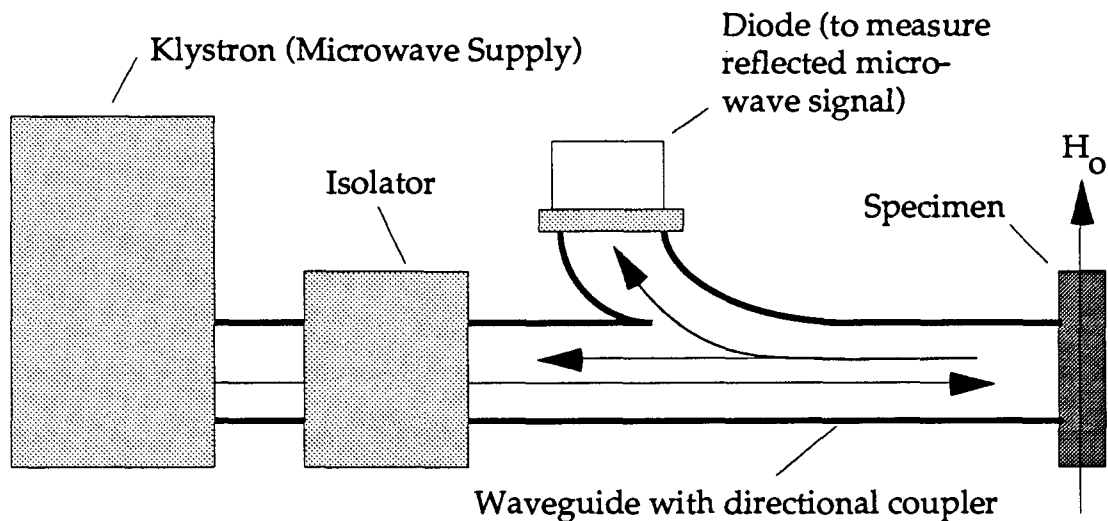


Fig. 2.23. The simplest practical microwave spectrometer. A klystron generates a beam of microwaves that are directed to a specimen via waveguide. An isolator prevents reflected microwaves from feeding back to the klystron. A directional coupler diverts part of the reflected beam to a diode that outputs a signal proportional to the amplitude of the reflected signal. The signal is measured as a function of the strength of the applied d.c. magnetic field H_0 .

Rudd (1985) has shown that the ratio of the reflected microwave power, P_r to the incident power, P_o , in a waveguide spectrometer, operating at 24 GHz with RG53/U waveguide and a Nickel specimen, is $P_r/P_o \approx (1 - 10^{-3})$ and that the change in the reflected power, ΔP_r , on sweeping through FMR is approximately $\Delta P_r/P_o \approx 5 \times 10^{-3}$. Hence the absorption signal is very small and superimposed on a large background.

The signal to noise ratio can be improved if the d.c. field H_o is modulated with a small a.c. magnetic field of frequency f_o and the component of the reflected signal is detected at the modulation frequency by means of a lock-in amplifier. If the amplitude of the modulation is smaller than the FMR linewidth, the output from the amplifier is proportional to the derivative of the absorption signal with respect to the d.c. field H_o .

That part of the reflected signal which varies as a consequence of FMR can be increased by making the specimen part of the wall of a resonant microwave cavity. A resonant cavity is the microwave equivalent of a resonant LCR circuit and is characterized by a resonant frequency, f_c , and a quality factor Q defined as $Q = 2\pi \times (\text{Energy stored into the cavity per cycle}) / (\text{Energy dissipated by the cavity per cycle})$. Energy is dissipated by the cavity in three ways: by specimen absorption, by resistive losses in the cavity walls, and by radiation loss through the hole used to couple microwaves into the cavity from a waveguide. Resistive losses by the walls are minimized by polishing the cavity walls mirror smooth and then electroplating them with a gold a few microns thick. Radiation loss (the reflected signal) is determined, to a large extent, by the size of the coupling hole.

Use of a cavity can enhance the change in the reflected power, ΔP_r , on sweeping through FMR to $\Delta P_r/P_o \approx 0.1$ or more. Such a change in reflected power is easily measured. One problem with using a cavity is that the resonance frequency shifts with the

specimen absorption (Rudd, 1985). This results in a variation of the reflected signal with H_0 that is not directly associated with resonant absorption. In order to remove this unwanted variations the klystron frequency is usually locked to the cavity resonant frequency. This is done by modulating the klystron frequency by applying a small a.c. voltage of frequency f_k to the d.c. klystron reflector voltage. The component of the signal reflected by the cavity at the frequency f_k depends on the difference between the klystron center frequency and the cavity frequency. The amplitude of the component is proportional to the difference. The error signal at frequency f_k is detected by means of a lock-in amplifier and is used to lock the klystron frequency to the resonant frequency of the cavity.

2.8.2 The *in situ* Microwave Cavity

The microwave cavity fabricated for the *in-situ* 16.88 GHz FMR spectrometer is illustrated in Fig. 2.24. The cavity was basically a cylindrical bucket 30 mm in diameter and 24 mm deep cut into a block of phosphor bronze. A phosphor bronze end-wall 1 mm thick covered the cavity. Specimens to be measured were brought up against a 12 mm hole in the end wall so they formed part of the cavity wall. The interior of the cavity was polished mirror smooth with diamond paste and electroplated with $\approx 10 \mu\text{m}$ thick layer of gold. This minimized microwave losses in the cavity walls (see section 2.8.1).

The cavity resonated in the TE_{011} and TE_{012} cylindrical cavity modes. The TE_{012} mode resonated at 16.88 GHz. The field distributions for the TE_{011} mode are shown in Fig. 2.24. The microwave magnetic field is radially directed and the microwave electric field circulates about the cavity axis. This latter feature is especially attractive in the *in-situ* spectrometer because specimens do not have to be in close contact with the end-wall in order for the cavity mode to resonate with a satisfactorily large Q value.

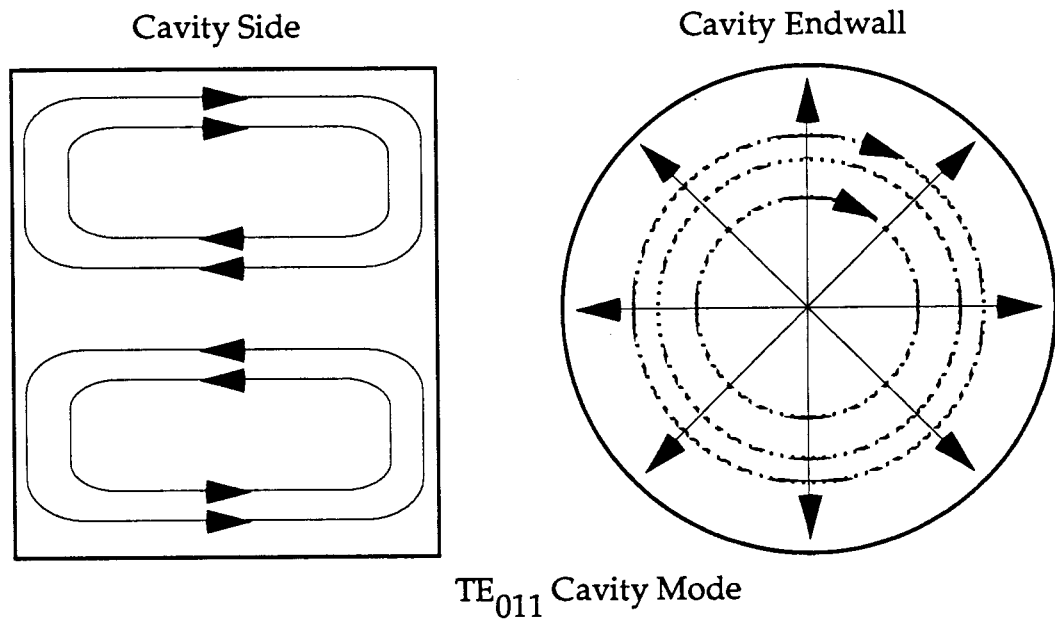
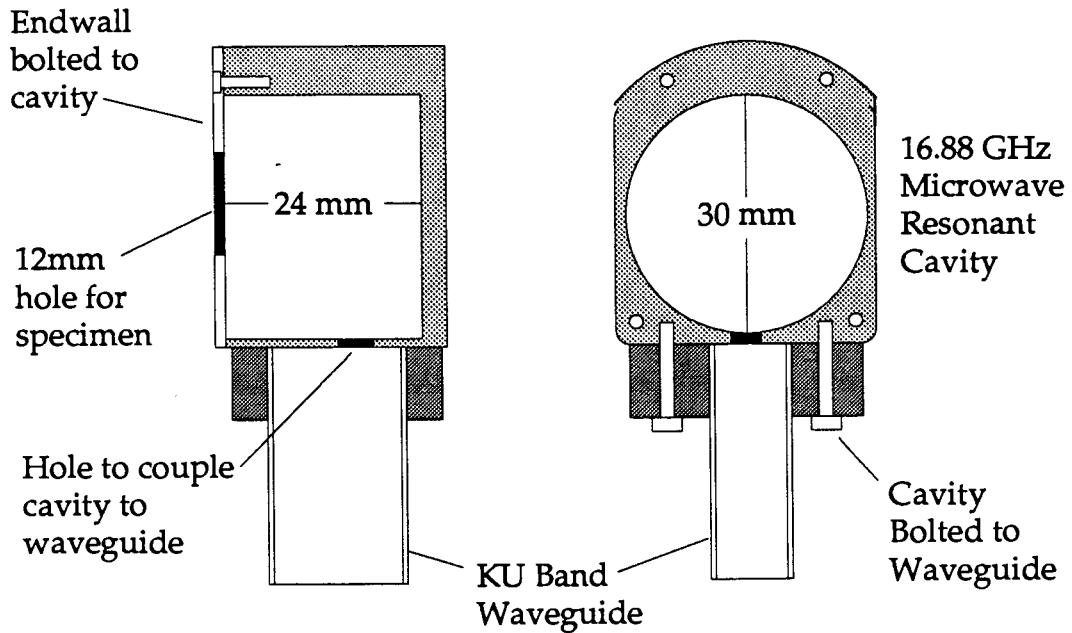


Fig. 2.24. In situ 16.88 GHz resonant microwave cavity and the microwave electric and magnetic field distributions of the TE_{011} resonant cavity mode. The magnetic field lines are solid, the electric field lines are dashed. A specimen brought up to the cavity endwall for FMR measurements does not need to make close contact with the wall in order for the cavity to resonate with a large Q value.

Perfect contact was difficult to achieve in practice due to small tilts between the cavity and the specimen holder. Tests carried out on the cavity outside the MBE facility showed that tilts up to 4° caused no detectable changes in the FMR absorption line-shape.

2.8.3 The *in-situ* FMR Spectrometer

The *in-situ* portion of the microwave spectrometer is shown in Fig. 2.25. The resonant cavity was attached to a 14" length of stainless steel KU-Band waveguide. Microwaves entered the cavity through a 4 mm coupling hole as shown in Fig. 2.24. The waveguide was attached to a 4.5" UHV mounting flange that formed part of a bellows assembly used to move the cavity into the tunnel connecting the MBE growth and analysis chambers. Specimens to be measured entered the tunnel from the analysis chamber and were pressed against the 12 mm hole in the end-wall of the cavity. The portion of the waveguide outside the MBE facility was sealed off from the atmosphere by means of a microwave permeable window made of mica. A double walled tube ran along the side of the waveguide and was connected to the cavity by means of a copper mesh "cooling finger". Feeding liquid nitrogen down this tube allowed the cavity and the specimen to be cooled for low temperature FMR measurements. The cooling system was not used in the experiments described in this thesis.

A schematic drawing of the entire *in-situ* microwave spectrometer is shown in Fig. 2.26. A water cooled electromagnet (described in the next section) supplied a uniform 0–5.5 kOe d.c. field at the position of the sample. Microwaves were generated by means of a Varian X-12 air cooled klystron driven by a PRD Electronics Inc. Type 819-A Universal Klystron Power Supply. The klystron operated in the 12.4–22 GHz frequency range with an output power of 100 milliWatts. The klystron frequency was locked to

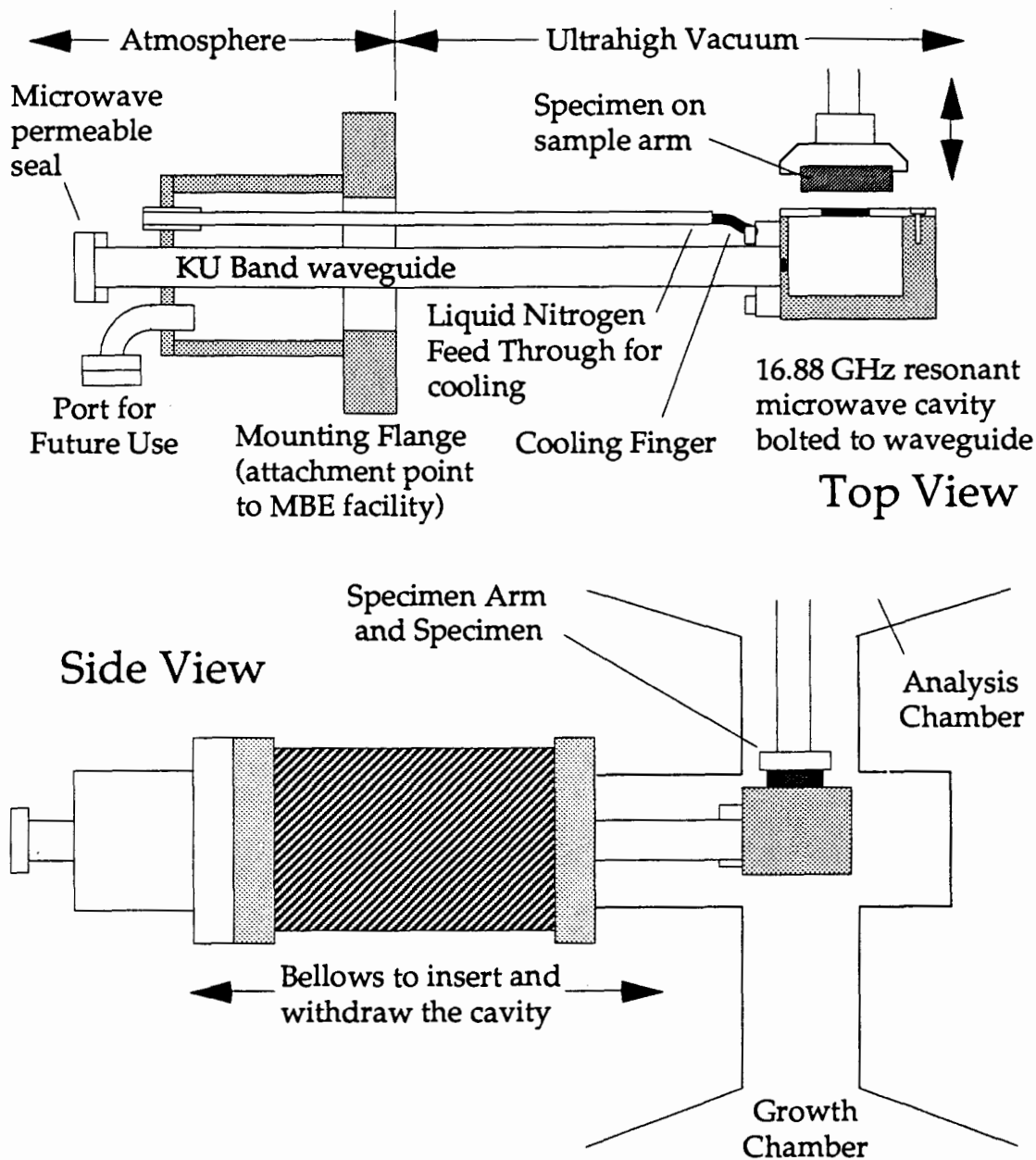


Fig. 2.25. In situ 16.88 GHz resonant microwave cavity and mount. A 14" length of KU band waveguide was attached to a 4.5" UHV mounting flange and sealed off from the atmosphere by a microwave permeable window. The cavity was attached to the other end. The cavity could be moved in and out of the tunnel connecting the growth and analysis chambers of the MBE facility. Specimens to be measured were brought up against a 12mm hole in the cavity endwall where they became part of the cavity. Cooling of the specimen could be accomplished by feeding liquid nitrogen through a double walled tube attached to the cavity with copper mesh. The above drawings are not to scale. The bellows assembly was approximately 14" long.

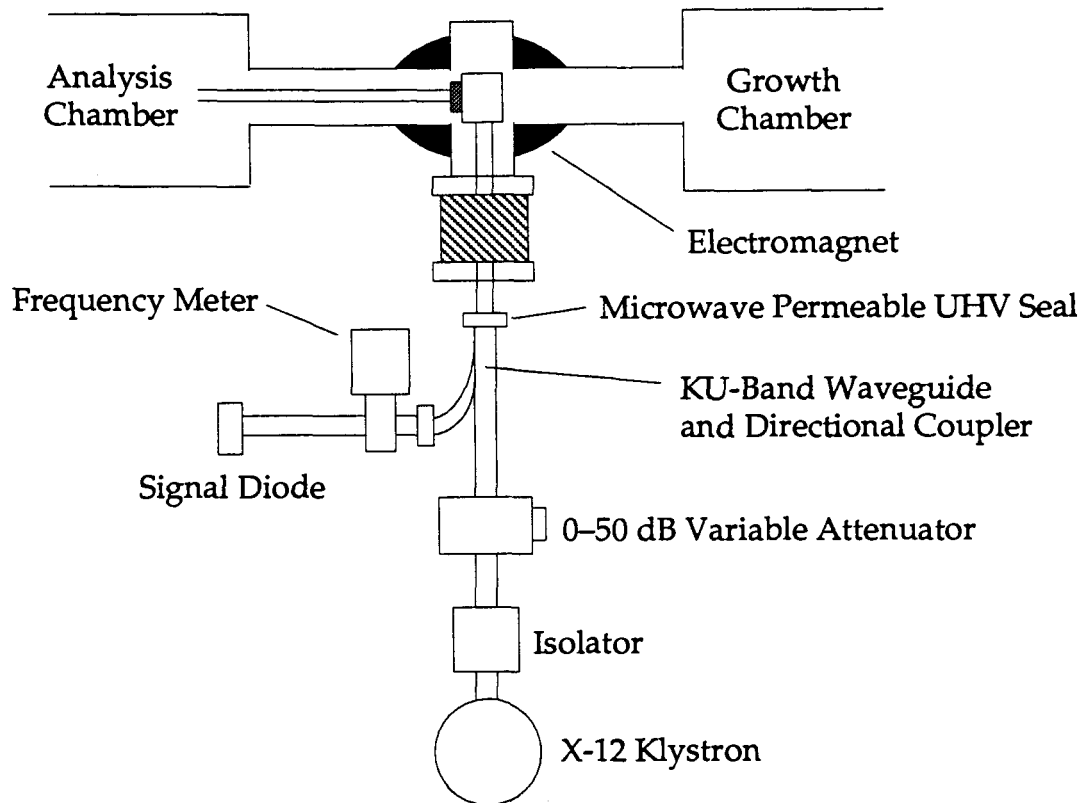


Fig. 2.26. The *in-situ* 16.88 GHz FMR Spectrometer. An electromagnet positioned around the tunnel connecting the MBE Growth and Analysis chambers supplies a 0–5.5 kOe d.c. field in the plane of the specimen. The specimen is made part of the end-wall of a 16.88 GHz resonant microwave cavity. An external Klystron supplies microwaves to the cavity and part of the reflected signal is detected by a point-contact diode that generates a voltage proportional to the amplitude of the microwaves incident on it. The d.c. field is weakly modulated at 70 Hz. The 70 Hz component of the reflected signal is detected by means of a lock-in amplifier to improve the signal to noise ratio. As a result, the FMR experiment provides a measure of the derivative of the absorption signal with respect to the applied magnetic field.

the 16.88 GHz resonant frequency of the cavity as described in section 2.8.1. A PRD Type 1208 microwave isolator prevented reflected microwave radiation from feeding back to the klystron. A Hewlett-Packard Model P375A 0–50 dB Variable Attenuator controlled the microwave output power level. A portion of the signal reflected from the cavity was diverted by a Sperry Microline Model 45U1-3 multihole coupler to a frequency meter and a point-contact diode. The Hewlett Packard Model P532A frequency meter was used to measure the microwave frequency to ± 0.005 GHz. The diode provided an output voltage proportional to the amplitude of the microwave signal incident upon it. The diode mount was electrically isolated from the waveguide by means of a mica gasket and nylon bolts. This prevented problems with ground loops. The d.c. magnetic field was weakly modulated by adding a small 73 Hz a.c. voltage to the output of the power supply connected to the electromagnet. Detecting the 73 GHz component of the diode output with a lock-in amplifier yielded the FMR absorption derivative as a function of the d.c. field. The d.c. field was measured using a Bell 630 Hall Probe located on one of the pole pieces of the electromagnet. The Hall probe calibration is described in the next section.

2.8.4 The *in-situ* Electromagnet

The static magnetic field for the *in-situ* FMR system was supplied by a water-cooled electromagnet designed by Mr. Ken Myrtle of the SFU Surface Physics Laboratory. The electromagnet surrounded the connecting tunnel between the MBE growth and analysis chambers as shown in Fig. 2.27. The yoke and pole pieces were made of soft iron. The pole pieces were approximately 3" \times 2" wide, elliptical in cross section, and 2.75" long. They were separated by a 1.5" gap. Each pole piece was wrapped with 150 turns of hollow copper tubing connected to a 300 Amp, 150 Volts power supply. Magnetic fields of

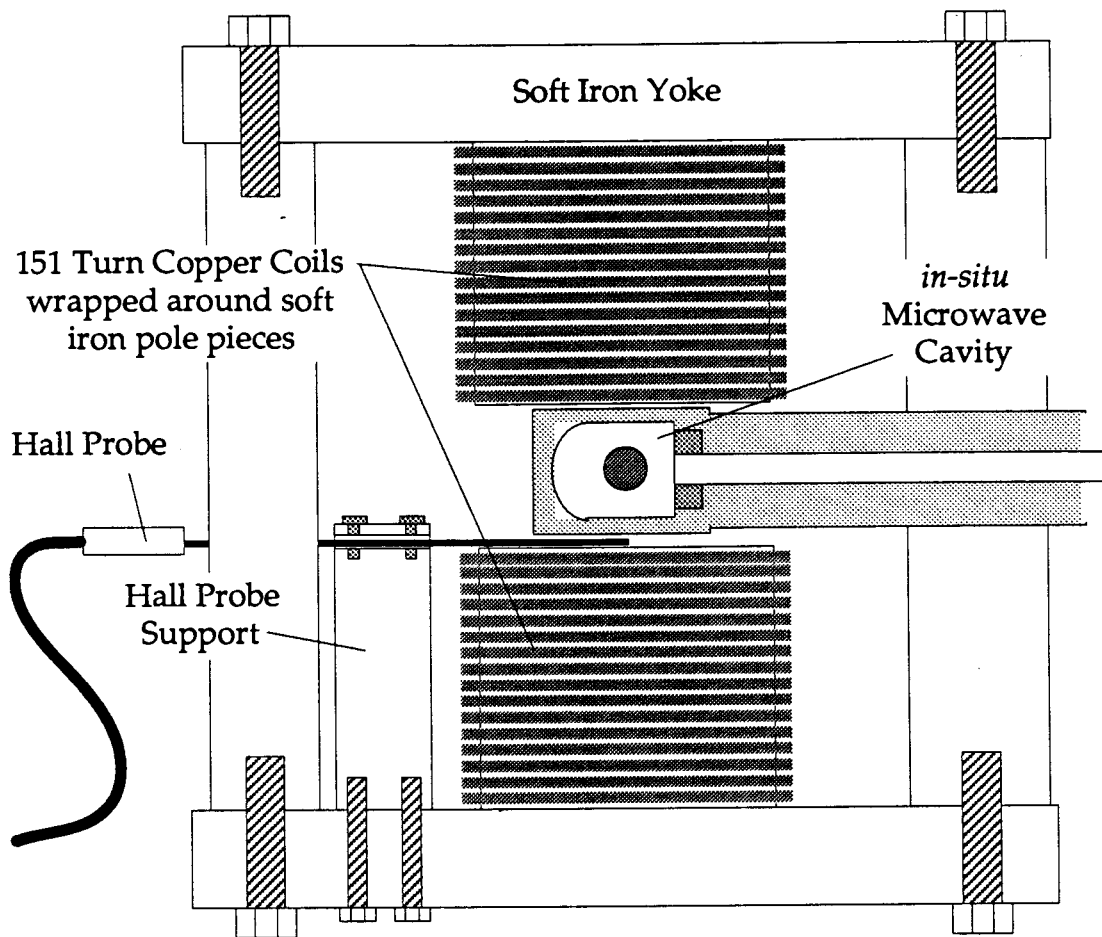


Fig. 2.27. Side view of the electromagnet used in conjunction with the 16.88 GHz *in-situ* FMR spectrometer. 5.5 kOe fields could be developed in the plane of the specimen. A Hall Probe mounted on one of the pole pieces measured the magnetic field.

up to 5.5 kOe could be generated at the center of the gap. A current of 150 Amps could be used to generate a field of 4 kOe indefinitely. The magnet was cooled during operation by forcing cold tap water through its windings. Cooling efficiency was increased by splitting the 150 turn coils in three places to form three separate 50-turn coils which could be cooled separately as shown in Fig. 2.28. The magnetic field in the gap was determined by means of a Bell 630 Hall Probe held placed on the lower pole piece. The Hall probe was calibrated in a separate experiment. A second Hall probe, calibrated

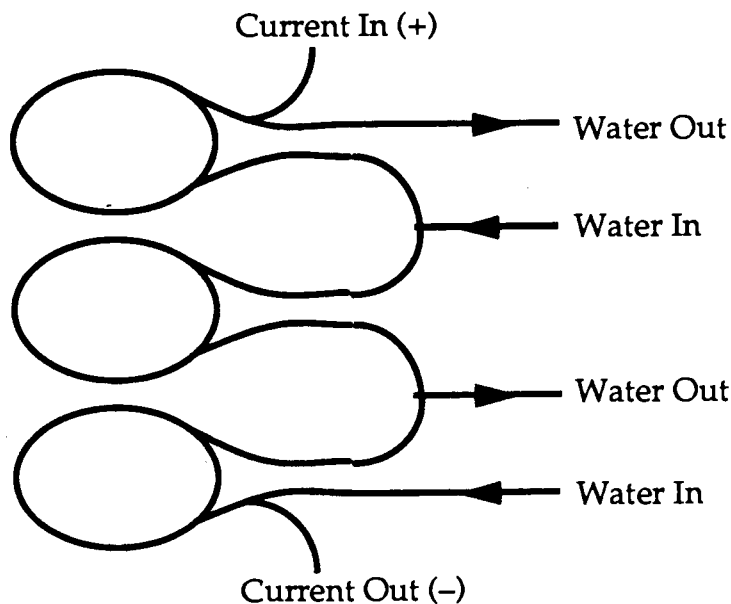


Fig. 2.28. Electrical and cooling water connections to each of the three 50-turn hollow copper coils wrapped around the pole pieces of the *in-situ* electromagnet. The coils are connected electrically in series to form a single 150 turn coil.

against NMR (Borer, 1978), was placed at the center of the magnet gap and the reading of the two probes compared over the full field range.

2.8.5 The *ex-situ* FMR Spectrometers

Three FMR spectrometers operating at 9.6, 36.6, and 73.0 GHz were used to measure the ultrathin films outside of the MBE facility. The systems used TE_{012} cylindrical cavities similar to the *in-situ* spectrometer (see section 2.8.2). The cavities could be surrounded by liquid nitrogen cooled vacuum dewars to enable FMR measurements to be carried out at $T = 77K$ as well as at room temperature. The magnetic fields for the *ex-situ* spectrometers was supplied from a Varian V-3800 electromagnet capable of generating 18 kOe fields in a 3.5" gap and, after installation of special pole pieces, 22.5 kOe fields in a 2" gap. A block diagram of the 73.0 GHz spectrometer is shown in Fig. 2.29.

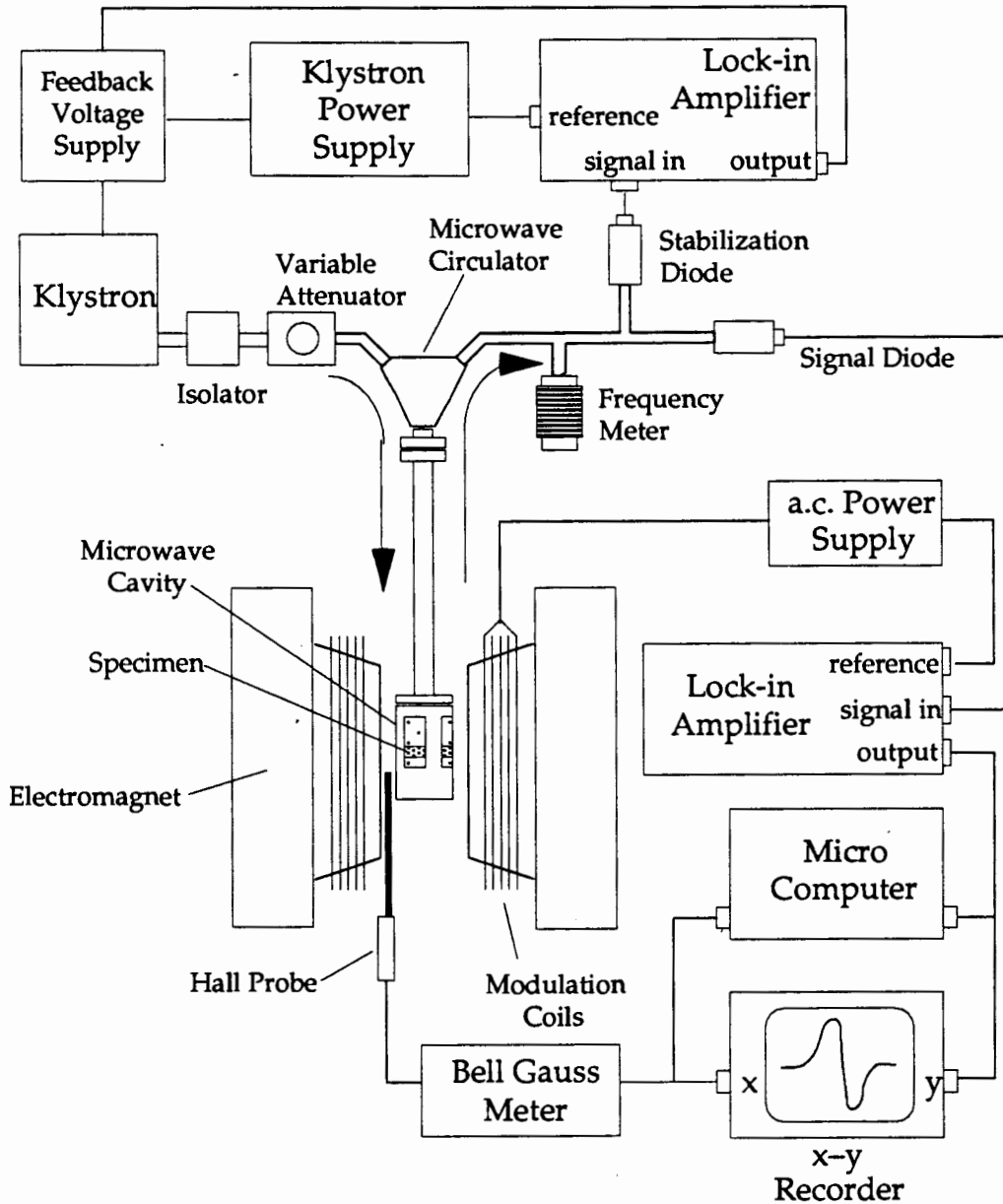


Fig. 2.29. Block diagram of a 73 GHz FMR spectrometer. A klystron supplies microwaves to a 73 GHz resonant cavity suspended between the pole pieces of an electromagnet. The ferromagnetic specimen forms part of the cavity end-wall. The klystron output and the applied d.c. field H_0 are weakly modulated and the microwaves reflected by the cavity are detected by a pair of sensing diodes as shown above. The output from the stabilization diode is fed into a lock-in amplifier and used to lock the klystron frequency to the resonant frequency of the cavity. The output of the signal diode is fed into a lock-in amplifier whose output is proportional to the magnetic field derivative of the microwave power absorbed by the specimen.

Chapter 3

FMR Theory

3.1 Introduction

Ferromagnetic resonance experiments measure either the microwave power absorption as a function of the applied d.c. magnetic field, H , or the derivative of the absorption with respect to the field. The resulting curves are described by a resonance field, H_{FMR} , that corresponds to maximum power absorption, and by an absorption linewidth, ΔH . In this chapter we calculate the microwave absorption of an ultrathin ferromagnetic film as a function of the applied field H and the magnetic parameters of the film. The latter include the saturation magnetization, $4\pi M_s$, the surface and the bulk magnetocrystalline anisotropies, the spectroscopic g -factor, and the magnetic damping parameter.

The standard approach combines Maxwell's equations for the rf electric and magnetic fields in the specimen with the Landau-Lifshitz equation of motion for the magnetization, including exchange, to set up and solve an appropriate boundary value problem (Ament and Rado, 1955). The surface anisotropies, which are of primary interest in this thesis, enter the problem through the boundary conditions on the magnetization (Rado and Weertman, 1959). The solution of the boundary value problem for a magnetic film of arbitrary thickness is complicated: the roots of a sixth-order polynomial must be extracted and the results used to solve an 8×8 set of simultaneous equations before the absorption can be calculated.

The absorption calculation can be considerably simplified for the case of an ultrathin film whose thickness, d , is much less than the rf skin depth, δ , of the metal. In this limit, one finds that the surface anisotropies affect the resonance field, H_{FMR} , precisely the same way as bulk anisotropies except that the surface terms have a $1/d$ dependence. This can be used to distinguish the surface anisotropies from the other parameters that determine H_{FMR} .

In section 3.2 the complete boundary value problem appropriate for an ultrathin film supported by a non-magnetic metal substrate is presented. The simplified solution valid for an ultrathin film is considered in section 3.3 where the $1/d$ dependence of the surface anisotropies is derived. Section 3.3 discusses how the surface and bulk anisotropies, the g -factor, the saturation magnetization and the magnetic damping parameter can be extracted from measured FMR spectra.

3.2 Calculation of the Microwave Absorption in an Ultrathin Film

The FMR spectrometers described in section 2.8 used the ultrathin bcc iron film and its supporting Ag(001) substrate as part of the endwall of a cylindrical microwave cavity. The d.c. magnetic field, H , was applied in the specimen plane and could be rotated in that plane. The model geometry appropriate for this experimental configuration is shown in Fig. 3.1. A thin ferromagnetic film of thickness “ d ” in the z -direction is supported by a non-magnetic metal substrate that fills the space $z > d$. The [001] crystallo-

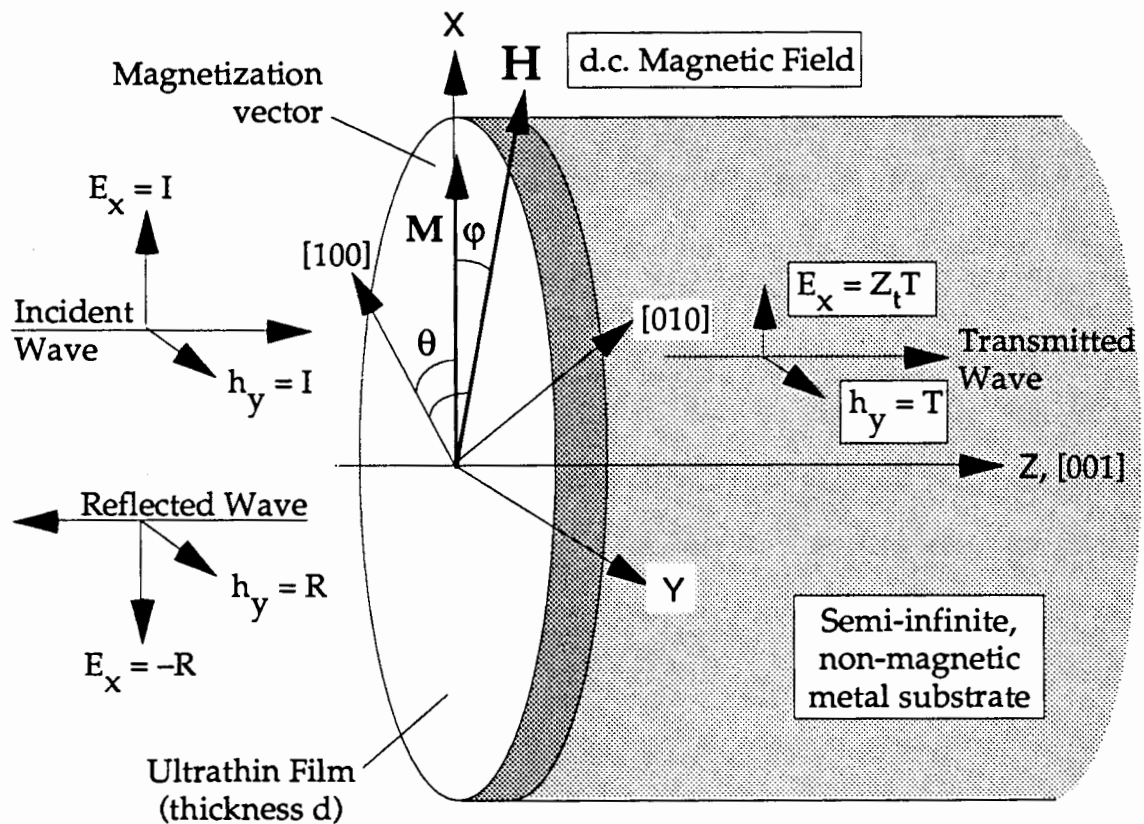


Fig. 3.1. Geometry used to calculate the absorption of microwave radiation by an ultrathin ferromagnetic film supported by a non-magnetic metal substrate. The film is assumed to be uniformly magnetized with the equilibrium direction of M parallel to the x -axis. The [100] in-plane crystal axis makes an angle θ with M . Magnetocrystalline anisotropy can cause the equilibrium direction of M to deviate by a small angle ϕ from the direction of the applied d.c. field H .

graphic direction in the film is normal to the specimen plane. The [100] axis makes an angle θ with the x-direction. The film is taken to be unbounded in the x and y directions and is assumed to be uniformly magnetized with the equilibrium saturation magnetization, M_s , directed along the x-axis and very nearly parallel with the applied magnetic field H . In-plane magnetocrystalline anisotropies tend to rotate M_s away from H unless the applied field is along one of the in-plane {100} or {110} directions. This has been taken into account by letting H be at an angle ϕ to M_s . The precise value of ϕ is discussed in section 3.2.3.

Linearly polarized microwave radiation impinges on the film at normal incidence from a vacuum filling the space $z < 0$. The incident microwave magnetic field is directed along the y-axis and is orthogonal to the equilibrium direction of the magnetization. This plane wave approximation is justified for specimens mounted in a microwave cavity because the index of refraction of the metal is so large that obliquely incident waves are refracted into the direction of the specimen normal.

The response of the model ultrathin ferromagnetic film to applied microwave radiation can be determined from Maxwell's equations for the rf electric and magnetic fields generated in the slab combined with the equation of motion for the magnetization (Ament and Rado, 1955). A solution is sought for the unknown transmitted and reflected microwave magnetic field amplitudes, T and R , that satisfies appropriate boundary conditions on the rf electric fields, magnetic fields, and magnetizations at the surfaces of the film. The microwave absorption can then be calculated from the values of I , R , and T (see section 3.2.5).

3.2.1 Maxwell's Equations

Maxwell's equations in Gaussian units are:

$$\begin{aligned}\nabla \times \mathbf{E} &= -\frac{1}{c} \frac{\partial \mathbf{b}}{\partial t}; & \nabla \times \mathbf{h} &= \frac{4\pi}{c} \mathbf{j} + \frac{1}{c} \frac{\partial \mathbf{D}}{\partial t} \\ \nabla \cdot \mathbf{b} &= 0; & \nabla \cdot \mathbf{D} &= 4\pi\rho\end{aligned}\tag{3.1}$$

We shall assume that all quantities have a space and time variation of $\exp(i[kz - \omega t])$ and that the constitutive relations linking the current density \mathbf{J} and the displacement \mathbf{D} with the electric field \mathbf{E} are given by

$$\mathbf{J} = \sigma \mathbf{E}; \quad \mathbf{D} = \epsilon \mathbf{E}\tag{3.2}$$

where σ is the d.c. conductivity and ϵ is the dielectric constant. For the geometry shown in Fig. 3.1, there will be no rf electric field components in the y-direction and no rf magnetic field components in the x-direction. Maxwell's equations therefore reduce to:

$$\begin{aligned}kE_x &= \frac{\omega}{c} b_y; & kh_y &= \left[\frac{4\pi i \sigma}{c} + \epsilon \frac{\omega}{c} \right] E_x \\ E_z &= 0; & b_z &= 0\end{aligned}\tag{3.3}$$

We seek solutions of equations (3.3) in the vacuum, in the film, and in the metal substrate. The vacuum occupying the space $z < 0$ is characterized by $b_y = h_y$, $\sigma = 0$ and $\epsilon = 1$. In this region, Maxwell's equations have the general solution:

$$h_y(z) = A_v e^{ikz} + B_v e^{-ikz}; \quad E_x(z) = A_v e^{ikz} - B_v e^{-ikz}; \quad k = \frac{\omega}{c}\tag{3.4}$$

where A_v and B_v are the amplitudes of waves travelling in the +ve z and -ve z directions respectively. The time dependence $\exp(-i\omega t)$ has been suppressed.

The nonmagnetic metal substrate is assumed to be a good conductor characterized by $b_y = h_y$, $\sigma \geq 10^{15} \text{ sec}^{-1}$ and $\epsilon = 1$. The displacement current is much smaller than the conduction current density in a good conductor at microwave frequencies and can be neglected. For example, at 36 GHz: $(4\pi\sigma/c) \approx 4 \times 10^7 \gg \epsilon(\omega/c) \approx 7.5$. The solution of equations (3.3) in the space $z > d$ for a wave travelling in the +ve z direction is therefore:

$$h_y(z) = A_s e^{ikz}; \quad E_x(z) = Z_t A_s e^{ikz}$$

$$Z_t = \frac{E_x(z)}{h_y(z)} = \frac{\omega}{c k}; \quad k^2 = i \frac{4\pi\omega\sigma}{c^2} = \frac{i}{\delta^2} \quad (3.5)$$

where A_s is the wave amplitude in the substrate and Z_t is the wave impedance. Note that the value of wave-vector, k , defined in equations (3.5) is not the same as the k defined in equations (3.4). The quantity $\delta = c/(4\pi\omega\sigma)^{1/2}$ is the rf skin depth, a measure of the distance a propagating wave can travel through a good conductor before its wave amplitude is attenuated by the factor of $\exp(-1)$. The skin depth for 36 GHz radiation propagating through a silver substrate ($\sigma \approx 9 \times 10^{17} \text{ esu}$) is approximately $\delta \approx 2.6 \times 10^{-5} \text{ cm}$. Implicit in (3.5) is the assumption that $\text{Im}[k] > 0$ (the imaginary part of the wave-vector, k , is positive) in order that the wave be attenuate as it travels into the substrate and away from the film.

The ferromagnetic film is also assumed to be a good conductor with $b_y = h_y + 4\pi m_y$. In this case, the general solutions of Maxwell's equations (3.3) take the form:

$$h_y(z) = \mathcal{A}e^{ikz} + \mathcal{B}e^{ik(d-z)}; \quad E_x(z) = \frac{\omega \mu_y}{c k} [\mathcal{A}e^{ikz} - \mathcal{B}e^{ik(d-z)}] \quad (3.6)$$

$$m_y(z) = \chi_y h_y(z); \quad b_y(z) = \mu_y h_y(z) \quad (3.7)$$

$$\chi_y = -\frac{1}{4\pi} (1 + ik^2 \delta^2); \quad \mu_y = -ik^2 \delta^2 \quad (3.8)$$

where we have defined a wave-number dependent susceptibility χ_y and a wave-number dependent permeability μ_y in equation (3.8). Again, the condition $\text{Im}[k] > 0$ is assumed and we point out that the values of k defined in (3.6)–(3.8) are not necessarily the same as those defined in (3.4) and (3.5). The solution corresponding to a wave traveling in the $-ve$ z direction in (3.6) was given an exponential factor of $\exp(ik[d-z])$ instead of $\exp(-ikz)$ to simplify notation in the boundary value problem described in section 3.2.5.

This is all the information that Maxwell's equations can give us. To proceed further we need to find a relation between the effective permeability (or susceptibility) given by (3.8) and the unknown value(s) of the wave-vector k . This is obtained from the equation of motion of the magnetization in the film.

3.2.2 The Equation of Motion for the Magnetization

The magnetization vector in a ferromagnetic material obeys the equation of motion:

$$-\frac{1}{\gamma} \frac{\partial \mathbf{M}}{\partial t} = \mathbf{M} \times \mathbf{H}_{\text{eff}} \quad (3.9)$$

where \mathbf{H}_{eff} is the total internal magnetic field acting on the magnetization, $\gamma = g|e|/(2mc) = (g/2)(1.7588 \times 10^7 \text{ Oe}^{-1} \text{ sec}^{-1})$ is the gyromagnetic ratio; "g" is the g-factor (Kittel, 1949), "e" is the electronic charge, "m" is the electron rest mass, and "c" is the speed of light (Gaussian units). For bulk iron, $g = 2.09$ and $\gamma = 1.8379 \times 10^7 \text{ Oe}^{-1} \text{ sec}^{-1}$. The magnetic equation of motion is simply another way of saying that the time rate of change of the angular momentum \mathbf{J} of the magnetization \mathbf{M} is equal to the net torque $\boldsymbol{\tau}_{\text{eff}}$ acting on the magnetization: that is, $\partial \mathbf{J} / \partial t = \boldsymbol{\tau}_{\text{eff}}$. In this case, the angular momentum has been expressed in terms of \mathbf{M} through the quantum mechanical relation $\mathbf{M} = -\gamma \mathbf{J}$ (Brown, 1978) and the net torque has been written as $\boldsymbol{\tau}_{\text{eff}} = \mathbf{M} \times \mathbf{H}_{\text{eff}}$. The torque

causes the magnetization to precess around its equilibrium direction with a characteristic precessional frequency ω_0 . The equilibrium direction is defined by $\mathbf{M} \times \mathbf{H}_{\text{eff}} = 0$ (ie, no net torque on \mathbf{M}). This corresponds to the condition $\mathbf{M} = M_s \mathbf{x}$ for the geometry shown in Fig. 3.1 where \mathbf{x} is a unit vector in the x-direction.

The effective magnetic field, \mathbf{H}_{eff} , in our model is composed of six fields:

- | | |
|--|----------------------------|
| (1) The applied d.c. magnetic field: | \mathbf{H} |
| (2) The driving microwave magnetic field: | $\mathbf{h}(z,t)$ |
| (3) The demagnetizing field: | \mathbf{H}_d |
| (4) The magnetocrystalline anisotropy field: | \mathbf{H}_k |
| (5) The exchange field: | \mathbf{H}_{ex} |
| (6) The magnetic damping field: | \mathbf{H}_{damp} |

The magnetic fields, \mathbf{H}_i , associated with exchange and magnetocrystalline anisotropy are most easily calculated from their contributions, E_i , to the total free energy of the ultrathin film (Brown, 1978):

$$\mathbf{H}_i = \left(-\frac{\partial E_i(\mathbf{M})}{\partial M_x}, -\frac{\partial E_i(\mathbf{M})}{\partial M_y}, -\frac{\partial E_i(\mathbf{M})}{\partial M_z} \right) \quad (3.10)$$

where the free energy, E_i , is expressed as a function of the magnetization.

We now consider the form of the six fields in detail. In the discussions that follow, only small deviations from equilibrium will be considered and the magnetization will be written as

$$\mathbf{M} = (M_x, M_y, M_z) = M_s + \mathbf{m}(\mathbf{r}, t) \quad (3.11)$$

where $\mathbf{m}(\mathbf{r}, t)$ is the small rf deviation of \mathbf{M} from M_s . The magnitude of \mathbf{m} is assumed to be much less than the saturation magnetization M_s so that, to first order in \mathbf{m} , the magnetization (3.11) can be written as $\mathbf{M} \approx (M_s, m_y, m_z)$. Further, we will neglect all terms in the effective fields that are of second and higher order in m_y and m_z and consider only linear response to the applied microwave driving field $h_y(z, t)$.

(1) The applied d.c magnetic field H

The d.c. field H is applied in the x-y plane and at an angle ϕ to the x direction:

$$\mathbf{H} = (H \cos\phi, H \sin\phi, 0) \quad (3.12)$$

(2) The driving microwave magnetic field $h(z, t)$

The microwave magnetic field in the ultrathin film is directed along the y-axis:

$$\mathbf{h} = (0, h_y, 0) \quad (3.13)$$

which we shall assume to be much less than the applied d.c. field H and the saturation magnetization $4\pi M_s$.

(3) The demagnetizing field

The exchange interaction that aligns the magnetic moments in a ferromagnet parallel to one another is opposed by the magnetic dipole-dipole interaction which favors anti-parallel alignment as shown in Fig 3.2. For an exchange aligned collection of magnetic dipoles, the opposing field per unit volume (the "demagnetizing" or "depolarizing" field) is linearly dependent on $-\mathbf{M}$. For uniformly magnetized ellipsoidal specimens, the demagnetizing field can be written (Chikazumi, 1964):

$$\mathbf{H}_d = -4\pi \mathcal{D} \cdot \mathbf{M} \quad (3.14)$$

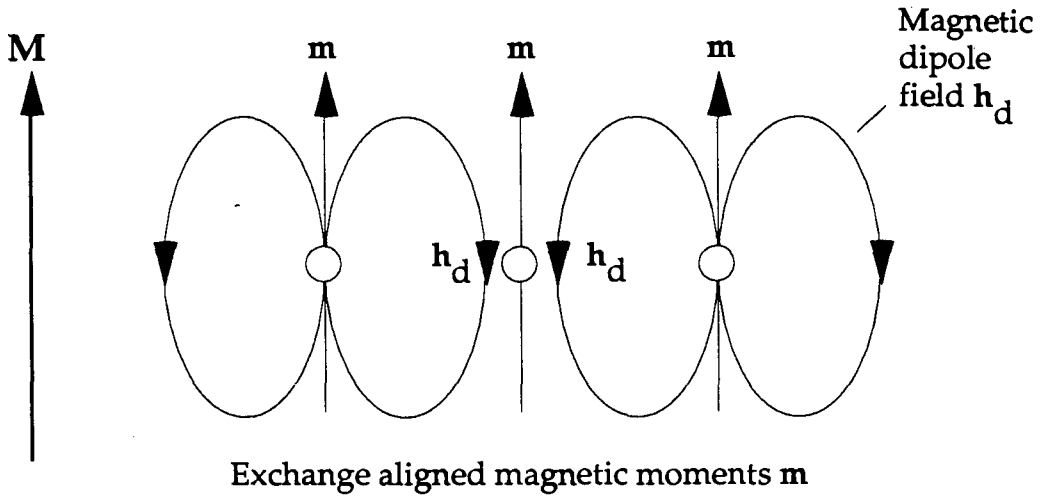


Fig. 3.2. Origin of the demagnetizing field in a ferromagnetic metal. Magnetic moments generate local dipole fields on one another that tends to oppose the aligning effect of the exchange interaction. The opposing field is proportional to M .

where \mathcal{D} is a 3×3 tensor whose components depend on the lengths of the three principal axes of the ellipsoid.

Continuum magnetic theory (which implicitly assumes that all specimen dimensions are much greater than the atomic lattice spacing) shows that the demagnetizing field H_d generated inside a ferromagnetic disc whose x and y dimensions are much greater than its thickness in the z direction is

$$\mathbf{H}_d = -4\pi \begin{bmatrix} D_x & 0 & 0 \\ 0 & D_y & 0 \\ 0 & 0 & D_z \end{bmatrix} \begin{bmatrix} M_x \\ M_y \\ M_z \end{bmatrix}; \quad D_x = D_y \approx 0; \quad D_z \approx 1 \quad (3.15)$$

This model breaks down for ultrathin films the order of a few atomic layers thick. The components of the demagnetizing tensor \mathcal{D} must be determined from an average over an explicit sum over the dipole magnetic fields acting on each magnetic moment in the lattice. The calculation for an ultrathin slab of bcc crystal of infinite extent in the plane and whose $[001]$ axis is oriented along the specimen normal is presented in

Appendix A. One can express the resulting demagnetizing field in a form similar to the continuum result (3.14) with $D_x = D_y = 0$ and

$$D_z(n) = 1 - \frac{0.42589}{n} \quad (3.16)$$

where “n” is the film thickness in monolayers. Equation (3.16) is accurate to 4 places when $n \geq 4$. For a monolayer film, $D_z(1) = 0.5392$, for a bilayer film, $D_z(2) = 0.7884$, and $D_z(3) = 0.8585$. $D_z(n)$ is very nearly equal to 1 for films thicker than 10 monolayers (see Table A.1 in Appendix A).

The ultrathin film demagnetizing field is therefore written as

$$\mathbf{H}_d = (0, 0, -4\pi D_z(n) m_z) \quad (3.17)$$

(4) The magnetocrystalline anisotropy field

The spin-orbit interaction causes the energy of a ferromagnetic crystal to depend on the direction of the magnetization relative to a particular set of crystal axes (Chikazumi, 1964). This directionally dependent energy is called the magnetocrystalline anisotropy energy and in an iron single crystal it takes the form valid for cubic symmetry:

$$E_k = K_1(\alpha_1^2\alpha_2^2 + \alpha_2^2\alpha_3^2 + \alpha_3^2\alpha_1^2) \quad (3.18)$$

where the $\alpha_i = M_i/M_s$ are the direction cosines of \mathbf{M} referred to the [100], [010], and [001] cube edges and K_1 is the first order cubic anisotropy coefficient expressed in ergs/cm³. For bulk iron, $K_1 \approx 4.8 \times 10^5$ ergs/cm³ and the anisotropy energy is a minimum when the magnetization points along a {100} direction (the “easy” axes) and a maximum when the magnetization points along a {111} direction (the “hard” axes). The magnetocrystalline anisotropy torque is zero along these directions. For other direc-

tions there will be a torque on M that acts to pull the magnetization into the nearest easy direction.

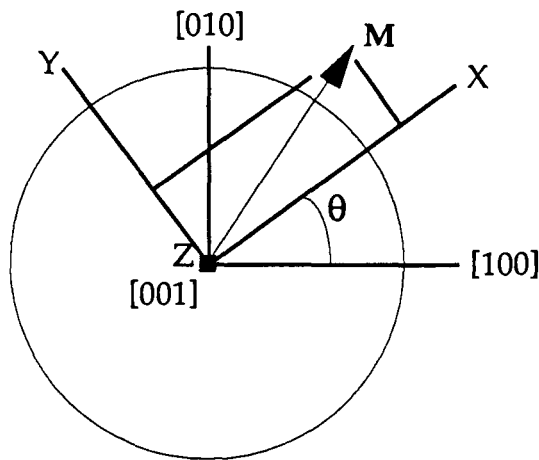
The effective magnetic field, H_k , associated with this torque is determined from (3.18) using (3.10). To begin with, the identity $\alpha_1^2 + \alpha_2^2 + \alpha_3^2 = 1$ is used to replace α_1^2 by $1 - \alpha_2^2 - \alpha_3^2$, α_2^2 by $1 - \alpha_3^2 - \alpha_1^2$, and α_3^2 by $1 - \alpha_1^2 - \alpha_2^2$ in (3.18). Multiplying out and collecting terms yields

$$E_k = K_1 - K_1(\alpha_1^4 + \alpha_2^4 + \alpha_3^4) - K_1(\alpha_1^2\alpha_2^2 + \alpha_2^2\alpha_3^2 + \alpha_3^2\alpha_1^2)$$

or

$$E_k = -\frac{K_1}{2}(\alpha_1^4 + \alpha_2^4 + \alpha_3^4) \quad (3.19)$$

where the constant energy term has been ignored because it will not contribute to the effective field. The direction cosines in (3.19) are defined in terms of the magnetization components M_1 , M_2 , and M_3 referred to the cubic crystal axes. We are working in a frame in which z is parallel with $[001]$ while the x and y directions are rotated away from $[100]$ and $[010]$, respectively, by an arbitrary angle θ (see Fig. 3.1). The components of the magnetization in the two frames are related by:



$$\begin{aligned} M_1 &= M_x \cos\theta - M_y \sin\theta \\ M_2 &= M_x \sin\theta + M_y \cos\theta \\ M_3 &= M_z \end{aligned} \quad (3.20)$$

Replacing the direction cosines, α_i , in (3.19) by their definitions $\alpha_1 = M_1/M_s$, $\alpha_2 = M_2/M_s$, and $\alpha_3 = M_3/M_s$ and then applying the transformation equations (3.20) yields:

$$E_k = -\frac{K_1}{2M_s^4} \left[(M_x \cos \theta - M_y \sin \theta)^4 + (M_x \sin \theta + M_y \cos \theta)^4 + M_z^4 \right] \quad (3.21)$$

The effective anisotropy fields, H_k , can now be obtained from (3.10). After carrying out the indicated differentiations, the magnetization components are replaced by $M_x \approx M_s$, $M_y = m_y$, $M_z = m_z$ and only terms that are first order in the small rf magnetization components m_y and m_z are retained. The result is:

$$H_x^k = \frac{2K_1}{M_s^2} \left[M_s (\cos^4 \theta + \sin^4 \theta) - \frac{3}{2} m_y (2 \sin \theta \cos \theta) (\cos^2 \theta - \sin^2 \theta) \right]$$

$$H_y^k = \frac{2K_1}{M_s^2} \left[-M_s (\sin \theta \cos \theta) (\cos^2 \theta - \sin^2 \theta) + 3 m_y (2 \sin \theta \cos \theta)^2 \right] \quad (3.22)$$

$$H_z^k = 0$$

Repeated application of the trigonometric identities:

$$\begin{aligned} 2 \sin \theta \cos \theta &= \sin 2\theta; & \cos^2 \theta - \sin^2 \theta &= \cos 2\theta \\ \sin^2 \theta &= \frac{1}{2} - \frac{1}{2} \cos 2\theta; & \cos^2 \theta &= \frac{1}{2} + \frac{1}{2} \cos 2\theta \\ \cos^4 \theta + \sin^4 \theta &= \frac{1}{4} (3 + \cos 4\theta) \end{aligned} \quad (3.23)$$

reduces the effective fields to the simpler forms (to lowest order in m_y and m_z):

$$H_x^k = \frac{K_1}{2M_s^2} [M_s(3 + \cos 4\theta) - 3m_y \sin 4\theta]$$

$$H_y^k = \frac{K_1}{2M_s^2} [-M_s \sin 4\theta + 3m_y(1 - \cos 4\theta)] \quad (3.24)$$

$$H_z^k = 0$$

(5) The exchange field

The energy associated with the exchange interaction is a minimum when all of the magnetic moments in a ferromagnet are parallel to one another (ie, the specimen is uniformly magnetized). Any deviations from parallelism results in an energy increase and a restoring torque on the magnetization. An expression for the exchange energy can be obtained from symmetry arguments (Turov, 1965) or from the simple derivation given by Brown (1978) that starts with the Heisenberg exchange interaction between two nearest-neighbour spins ($E_{ij} = -2J \mathbf{S}_i \cdot \mathbf{S}_j$) and considers the energy change as the spins are tilted out of alignment. In either case, one obtains the expression:

$$E_{\text{ex}} = \frac{A}{M_s^2} \left((\nabla M_x)^2 + (\nabla M_y)^2 + (\nabla M_z)^2 \right) \quad (3.25)$$

where A is the exchange "stiffness" parameter. In bulk iron, $A = 2 \times 10^{-6}$ ergs-Gauss². For $M_x \approx M_s$, $M_y = m_y$, $M_z = m_z$ and the assumed spatial variation of $\exp(ikz)$, the exchange field associated with (3.25) is given by:

$$H_{\text{ex}} = \frac{2A}{M_s^2} \left(0, \frac{\partial^2 m_y}{\partial z^2}, \frac{\partial^2 m_z}{\partial z^2} \right) = - \frac{2A k^2}{M_s^2} (0, m_y, m_z) \quad (3.26)$$

(6) Magnetic damping

The spin orbit interaction responsible for magnetocrystalline anisotropy also contributes to damping of the precessional motion as the magnetization changes direction in the lattice. The damping processes that allow the magnetization to relax back to its equilibrium state are included in the equation by an effective magnetic field proportional to the negative time rate of change of the magnetization (Gilbert, 1955, Brown, 1978):

$$\mathbf{H}_G = - \frac{G}{\gamma^2 M_s^2} \frac{\partial \mathbf{M}}{\partial t} = i \frac{\omega}{\gamma} \frac{G}{\gamma M_s^2} (0, m_y, m_z) \quad (3.27)$$

where G is the Gilbert damping parameter and the time variation has been taken to be $\exp(-i\omega t)$. For pure iron, $G = 0.66 \times 10^8 \text{ sec}^{-1}$ (Heinrich et al., 1987).

The effective field, \mathbf{H}_{eff} acting on the magnetization is composed of the six terms defined by equations (3.12), (3.13), (3.17), (3.24), (3.26), and (3.27). The components of the total effective field are:

$$\begin{aligned} H_x^{\text{eff}} &= H \cos \varphi + H_x^k \\ H_y^{\text{eff}} &= H \sin \varphi + h_y + H_y^k - \frac{2A k^2}{M_s^2} m_y + i \frac{\omega}{\gamma} \left(\frac{G}{\gamma M_s} \right) m_y \\ H_z^{\text{eff}} &= -4\pi D_z m_z + H_z^k - \frac{2A k^2}{M_s^2} m_z + i \frac{\omega}{\gamma} \left(\frac{G}{\gamma M_s} \right) m_z \end{aligned} \quad (3.28)$$

For a magnetization vector of $\mathbf{M} \approx (M_s, m_y, m_z)$, and a time variation of $\exp(-i\omega t)$, the equation of motion (3.9) goes over into:

$$- \frac{1}{\gamma} \frac{\partial \mathbf{M}}{\partial t} = \mathbf{M} \times \mathbf{H}_{\text{eff}} \Rightarrow \begin{bmatrix} 0 \\ i \frac{\omega}{\gamma} m_y \\ i \frac{\omega}{\gamma} m_z \end{bmatrix} = \begin{bmatrix} m_y H_z^{\text{eff}} - m_z H_y^{\text{eff}} \\ m_z H_x^{\text{eff}} - M_s H_z^{\text{eff}} \\ M_s H_y^{\text{eff}} - m_y H_x^{\text{eff}} \end{bmatrix} \quad (3.29)$$

Inserting (3.28) into (3.29), multiplying everything out, and keeping only the terms that are first order in h_y , m_y and m_z yields the two equations:

$$-i\frac{\omega}{\gamma} m_y + \left[B_z + \frac{2A k^2}{M_s} - i\frac{\omega}{\gamma} \left(\frac{G}{\gamma M_s} \right) \right] m_z = 0 \quad (3.30)$$

$$\left[H_y + \frac{2A k^2}{M_s} - i\frac{\omega}{\gamma} \left(\frac{G}{\gamma M_s} \right) \right] m_y + i\frac{\omega}{\gamma} m_z = M_s h_y \quad (3.31)$$

where

$$B_z = H \cos \varphi + 4\pi D_z M_s + \frac{K_1}{2M_s} [3 + \cos 4\theta] \quad (3.32)$$

$$H_y = H \cos \varphi + \frac{2K_1}{M_s} \cos 4\theta \quad (3.33)$$

3.2.3 The Equilibrium Tilt Angle

The angle φ between the equilibrium magnetization M_s and the applied d.c. field H is determined by the requirement that $\mathbf{M} \times \mathbf{H}_{\text{eff}} = 0$ in equilibrium. The result is:

$$K_1 \sin 4\theta - 2HM_s \sin \varphi = 0 \quad (3.34)$$

or

$$\sin \varphi = \frac{K_1 \sin 4\theta}{2HM_s} \quad (3.35)$$

The tilt angle, φ , decreases with increasing H and is zero when the applied field is directed along one of the in-plane $\{100\}$ magnetically easy directions or in-plane $\{110\}$ hard directions. We can estimate the effect of tilting in our work by evaluating (3.35) for the lowest magnetic fields used ($H \approx 3500$ Oe) and the largest cubic anisotropy coeffi-

cent measured ($K_1 \approx 5 \times 10^5$ ergs/cm³) – see Tables 5.1-5.6 in chapter 5. Assuming $M_s \approx 1715$ Gauss (the bulk iron value) and $\sin(4\theta) = 1$, yields $\sin\phi \leq 0.04$ or $\phi \approx 2.4^\circ$. The tilt angle enters the equations of motion (3.30)-(3.33) through terms of the form $H\cos\phi$. Since $\cos(2.4^\circ) \approx 0.9992$, the assumption $\cos\phi = 1$ introduces only an error of less than 4 Oe in the value of H.

3.2.4 The Effective Microwave Permeability

Equation (3.30) can be used to eliminate m_z from (3.31) and the resulting expression used to define the effective susceptibility χ_y or, equivalently, the effective permeability $\mu_y = [1 + 4\pi(m_y/h_y)]$ that appears in equations (3.8):

$$\mu_y = \frac{\left[B_z + \frac{2A}{M_s} k^2 - i\frac{\omega}{\gamma} \left(\frac{G}{\gamma M_s} \right) \right] \left[H_y + 4\pi M_s + \frac{2A}{M_s} k^2 - i\frac{\omega}{\gamma} \left(\frac{G}{\gamma M_s} \right) \right] - \left(\frac{\omega}{\gamma} \right)^2}{\left[B_z + \frac{2A}{M_s} k^2 - i\frac{\omega}{\gamma} \left(\frac{G}{\gamma M_s} \right) \right] \left[H_y + \frac{2A}{M_s} k^2 - i\frac{\omega}{\gamma} \left(\frac{G}{\gamma M_s} \right) \right] - \left(\frac{\omega}{\gamma} \right)^2} \quad (3.36)$$

The permeability exhibits a resonant behaviour that depends on the strength of the applied field, H, and the magnetic parameters that characterize the film. The value of the applied field for which the effective permeability is a maximum corresponds to ferromagnetic resonance (FMR). The resonance field, H_{FMR} , can be estimated from (3.36) by ignoring exchange, damping, and anisotropy. In this case:

$$\mu_y = \frac{(H + 4\pi D_z M_s)(H + 4\pi M_s) - (\omega/\gamma)^2}{H(H + 4\pi D_z M_s) - (\omega/\gamma)^2} \quad (3.37)$$

and FMR occurs when the denominator vanishes:

$$H_{\text{FMR}}(H_{\text{FMR}} + 4\pi D_z M_s) = (\omega/\gamma)^2 \quad (3.38)$$

For a thick iron film and 36 GHz incident microwave radiation: $D_z = 1$, $4\pi M_s = 21.55$ kOe, and $(\omega/\gamma) = 12.31$ kOe. The magnetic field corresponding to FMR is therefore $H_{\text{FMR}} = 5.58$ kOe.

Consistency between (3.8) and (3.36) determines the allowed values of the wave-vector k in the film. Equating the two expressions for the effective permeability leads to a cubic equation in the dimensionless quantity $K^2 = (k\delta)^2$:

$$C_3 K^6 + C_2 K^4 + C_1 K^2 + C_0 = 0 \quad (3.39)$$

where
$$A_M = \frac{2A}{\delta^2 M_s} \quad (3.40)$$

$$C_3 = A_M^2; \quad C_2 = A_M (B_z + H_y - iA_M) \quad (3.41)$$

$$C_1 = B_z H_y - \left(\frac{\omega}{\gamma}\right)^2 - iA_M (B_z + H_y + 4\pi M_s) \quad (3.42)$$

$$C_0 = -i \left[B_z (H_y + 4\pi M_s) - \left(\frac{\omega}{\gamma}\right)^2 \right] \quad (3.43)$$

The incident microwave radiation excites six waves in the film (three propagating in the +z direction and three propagating in the -z direction). A discussion of these wave solutions can be found in Cochran et al. (1977a) or Cochran et al. (1986).

3.2.5 The Boundary Value Problem

Having determined the six allowed values of k in the film we can solve the boundary value problem shown in Fig. 3.1 and repeated in Fig. 3.3. Referring to equations (3.6)-(3.8), and (3.30), we can write the rf electric fields, magnetic fields, and magnetizations in the film as:

$$h_y(z) = \sum_{j=1}^3 \mathcal{A}_j e^{ik_j z} + \mathcal{B}_j e^{ik_j (d-z)} \quad (3.44)$$

$$E_x(z) = \sum_{j=1}^3 \frac{\omega}{c k_j} (-ik_j^2 \delta^2) [\mathcal{A}_j e^{ik_j z} - \mathcal{B}_j e^{ik_j (d-z)}] \quad (3.45)$$

$$m_y(z) = -\frac{1}{4\pi} \sum_{j=1}^3 (1 + ik_j^2 \delta^2) [\mathcal{A}_j e^{ik_j z} + \mathcal{B}_j e^{ik_j (d-z)}] \quad (3.46)$$

$$m_z(z) = -\frac{i}{4\pi} \frac{\omega}{\gamma} \sum_{j=1}^3 \left(\frac{1 + ik_j^2 \delta^2}{B_z + A_M k_j^2 \delta^2 - i \left(\frac{\omega}{\gamma} \right) \frac{G}{\gamma M_s}} \right) [\mathcal{A}_j e^{ik_j z} + \mathcal{B}_j e^{ik_j (d-z)}] \quad (3.47)$$

The six unknown wave amplitudes \mathcal{A}_j and \mathcal{B}_j , and the reflected and transmitted wave amplitudes, R and T, are determined by the boundary conditions on the rf fields at the $z = 0$ and at the $z = d$ film boundaries and by the amplitude, I, of the incident micro-

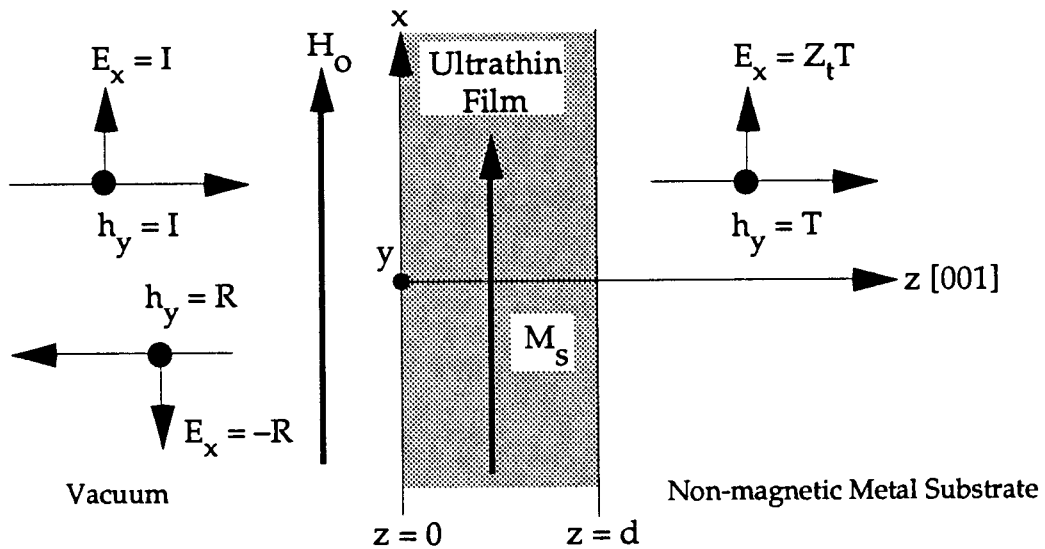


Fig. 3.3. The geometry for the ultrathin film boundary value problem.

wave magnetic field. The quantity measured by the FMR absorption experiment is proportional to the reflected microwave power, P_r . The reflected power is calculated using the time averaged Poynting vector (Jackson, 1975):

$$\bar{\mathbf{S}} = \frac{c}{8\pi} \text{Re}[\mathbf{E} \times \mathbf{h}^*] \quad (3.48)$$

Since the linearly polarized reflected wave has components $E_x = -R$ and $h_y = R$ the ratio of the reflected power to the incident power, P_i , is

$$\frac{P_r}{P_i} = \frac{|R|^2}{|I|^2} = |R|^2 \quad (3.49)$$

where the incident wave amplitude, I , has been taken to be 1 Oe for convenience. The ratio of the total power, P_a , absorbed by the film and the substrate to the incident power is

$$\frac{P_a}{P_i} = 1 - |R|^2 \quad (3.50)$$

The electromagnetic boundary conditions

The boundary conditions on the electric and magnetic fields are simple: the tangential components of \mathbf{E} and \mathbf{h} must be continuous across the film boundaries at $z = 0$ and $z = d$. With reference to Fig. 3.3, we write:

$$h_y(0) = I + R; \quad E_x(0) = I - R \quad (3.51)$$

$$h_y(d) = T; \quad E_x(d) = Z_t T \quad (3.52)$$

which may be equated with the values of the electric and magnetic fields at $z = 0$ and $z = d$ given by (3.44) and (3.45) to obtain four equations for the eight unknown wave amplitudes:

$$I = -R + \sum_{j=1}^3 \mathcal{A}_j + \mathcal{B}_j e^{ik_j d} \quad (3.53)$$

$$I = R + \sum_{j=1}^3 \frac{\omega}{c k_j} (-ik_j^2 \delta^2) [\mathcal{A}_j - \mathcal{B}_j e^{ik_j d}] \quad (3.54)$$

$$0 = -T + \sum_{j=1}^3 \mathcal{A}_j e^{ik_j d} + \mathcal{B}_j \quad (3.55)$$

$$0 = -Z_t T + \sum_{j=1}^3 \frac{\omega}{c k_j} (-ik_j^2 \delta^2) [\mathcal{A}_j e^{ik_j d} - \mathcal{B}_j] \quad (3.56)$$

where I is the amplitude of the incident microwave magnetic field and Z_t is the wave impedance in the substrate as defined by equation (3.5).

The boundary conditions on the magnetization

The boundary conditions on the rf magnetization components (3.46) and (3.47) are determined by the additional torques, τ_s , that act only on the surface spins at $z = 0$ and at $z = d$. These torques are due, for example, to surface anisotropies and surface exchange fields (Rado and Weertman, 1959). One way of deriving the boundary conditions is to formally include the surface torques in the equation of motion (3.9) in the form of delta function effective fields $H_s\delta(z)$ and $H_s\delta(z-d)$. Integrating the equation of motion from $z = -\epsilon$ to $z = \epsilon$ and from $z = d-\epsilon$ to $z = d+\epsilon$, where ϵ is vanishingly small, results in the following two conditions on the surface spins:

$$\mathbf{M} \times \mathbf{H}_s \Big|_{z=0} = 0; \quad \mathbf{M} \times \mathbf{H}_s \Big|_{z=d} = 0 \quad (3.57)$$

Our model will include three effective surface fields in \mathbf{H}_s :

(1) The surface exchange fields (Rado and Weertman, 1959):

$$\mathbf{H}_{\text{ex}}^{\text{surf}} = \frac{2A}{M_s^2} \frac{\partial \mathbf{M}}{\partial z} \Big|_{z=0}; \quad \mathbf{H}_{\text{ex}}^{\text{surf}} = -\frac{2A}{M_s^2} \frac{\partial \mathbf{M}}{\partial z} \Big|_{z=d} \quad (3.58)$$

where A is the exchange constant that appears in the bulk exchange field (3.26). When the exchange fields are included, the boundary conditions (3.57) are usually referred to as the "generalized exchange boundary conditions". The fields (3.58) are a consequence of the discontinuity in the exchange forces at the surfaces of the specimen.

(2) A uniaxial (two fold) surface anisotropy with easy axis along the specimen normal:

$$E_2 = -K_s \frac{m_z^2}{M_s^2} \quad (3.59)$$

where K_s describes the strength of the uniaxial surface anisotropy in ergs/cm². A positive value of K_s indicates that the easy direction of magnetization associated with this term is along the specimen normal. A negative value indicates the energy is a minimum for the magnetization oriented in the plane. The effective surface field associated with this energy is

$$\mathbf{H}_2^{\text{surf}} = \left(0, 0, \frac{2K_s}{M_s^2} m_z \right) \quad (3.60)$$

(3) A fourth order surface anisotropy energy having the symmetry of the bcc Fe(001) surface:

$$E_4^{\text{surf}} = -\frac{1}{2} K_1^{\text{surf}} (\alpha_1^4 + \alpha_2^4) - \frac{1}{2} K_{\perp}^{\text{surf}} \alpha_3^4 \quad (3.61)$$

where α_1 , α_2 , and α_3 are the direction cosines of the surface magnetization vector with respect to the cube axes, K_1^{surf} describes the strength of the four-fold surface anisotropy in the specimen plane, and K_{\perp}^{surf} describes the strength of the four-fold surface anisotropy perpendicular to the film surface. Equation (3.61) can be re-written as

$$E_4^{\text{surf}} = -\frac{1}{2} K_1^{\text{surf}} (\alpha_1^4 + \alpha_2^4 + \alpha_3^4) - \frac{1}{2} (K_{\perp}^{\text{surf}} - K_1^{\text{surf}}) \alpha_3^4 \quad (3.62)$$

where the first term is identical in form to the energy term used to describe the bulk cubic anisotropy in iron (see equation 3.18). The second term in (3.62) corresponds to a fourth order uniaxial anisotropy having its symmetry axis along the [001] specimen normal. The term gives rise to an effective field that is third order in m_z which does not contribute to our first order calculation if the magnetization is confined to the plane of the specimen. The effective field associated with the four-fold energy term (3.62) is therefore (by analogy with (3.24)):

$$H_x^4 = \frac{K_1^{\text{surf}}}{2M_s^2} [M_s(3 + \cos 4\theta) - 3m_y \sin 4\theta]$$

$$H_y^4 = \frac{K_1^{\text{surf}}}{2M_s^2} [-M_s \sin 4\theta + 3m_y(1 - \cos 4\theta)] \quad (3.63)$$

$$H_z^k = 0$$

Inserting (3.58), (3.60), and (3.63) into the surface torque equations (3.57), and then multiplying out and keeping only terms that are first order in m_y and m_z , yields the four boundary conditions:

$$\frac{2A}{M_s} \frac{\partial m_y}{\partial z} \Big|_{z=0} = \left[\frac{2K_1^F}{M_s} \cos 4\theta \right] m_y(0) \quad (3.64)$$

$$\frac{2A}{M_s} \frac{\partial m_z}{\partial z} \Big|_{z=0} = \left[-\frac{2K_s^F}{M_s} + \frac{K_1^F}{2M_s} (3 + \cos 4\theta) \right] m_z(0) \quad (3.65)$$

$$-\frac{2A}{M_s} \frac{\partial m_y}{\partial z} \Big|_{z=d} = \left[\frac{2K_1^R}{M_s} \cos 4\theta \right] m_y(d) \quad (3.66)$$

$$-\frac{2A}{M_s} \frac{\partial m_z}{\partial z} \Big|_{z=d} = \left[-\frac{2K_s^R}{M_s} + \frac{K_1^R}{2M_s} (3 + \cos 4\theta) \right] m_z(d) \quad (3.67)$$

where the superscripts 'F' and 'R' denote the surface anisotropy coefficients at the front ($z = 0$) and the rear ($z = d$) of the film.

Evaluating (3.46) and (3.47) at $z = 0$ and $z = d$, and substituting the resulting equations into (3.64)-(3.67), yields four relations between the six unknown internal wave amplitudes \mathcal{A}_j and \mathcal{B}_j . Combining these with the four relations (3.53)-(3.56) specified by the

electromagnetic boundary conditions completely determines the wave amplitudes in the film and the reflected and transmitted wave amplitudes R and T . Once the reflected wave amplitude is known the power absorbed by the film and substrate can be calculated from (3.50). The expressions for the wave amplitudes are extremely complicated. A computer program was written to extract the wave-vectors, k , from the cubic equation (3.39) and to solve numerically the boundary value problem. The program calculates the microwave absorption and the absorption derivative with respect to the applied field as functions of the material parameters that characterize the film and the substrate.

3.3 A Simplified Treatment of the Absorption Problem

3.3.1 The Integrated Equations of Motion

A simpler formulation of the microwave absorption problem in an ultrathin film can be derived from the equations of motion for the magnetization when the thickness of the ultrathin film is much less than the spatial variation of the fields and magnetization; that is, if the film thickness, d , is very small compared with the exchange length: $\sqrt{2\pi A/M_s^2} \approx 33 \text{ \AA}$ in iron. For reference, the equations of motion (3.30)-(3.33) used in our model calculation were:

$$-i\frac{\omega}{\gamma} m_y(z) + \left[B_z - i\frac{\omega}{\gamma} \left(\frac{G}{\gamma M_s} \right) \right] m_z(z) - \frac{2A}{M_s} \frac{\partial^2 m_z(z)}{\partial z^2} = 0 \quad (3.68)$$

$$\left[H_y - i\frac{\omega}{\gamma} \left(\frac{G}{\gamma M_s} \right) \right] m_y(z) - \frac{2A}{M_s} \frac{\partial^2 m_y(z)}{\partial z^2} + i\frac{\omega}{\gamma} m_z(z) = M_s h_y(z) \quad (3.69)$$

where

$$B_z = H + 4\pi D_z M_s + \frac{K_1}{2M_s} [3 + \cos 4\theta] \quad (3.70)$$

$$H_y = H + \frac{2K_1}{M_s} \cos 4\theta \quad (3.71)$$

where the small angle, ϕ , between the direction of H and M_s has been neglected (see section 3.2.3).

One starts by integrating (3.68)–(3.69) from $z = 0$ to $z = d$. The result is:

$$-i\frac{\omega}{\gamma}\mathcal{M}_y + \left[B_z - i\frac{\omega}{\gamma}\left(\frac{G}{\gamma M_s}\right) \right] \mathcal{M}_z - \frac{2A}{M_s} \frac{\partial m_z(z)}{\partial z} \Big|_{z=d} + \frac{2A}{M_s} \frac{\partial m_z(z)}{\partial z} \Big|_{z=0} = 0 \quad (3.72)$$

$$\begin{aligned} \left[H_y - i\frac{\omega}{\gamma}\left(\frac{G}{\gamma M_s}\right) \right] \mathcal{M}_y - \frac{2A}{M_s} \frac{\partial m_y(z)}{\partial z} \Big|_{z=d} + \frac{2A}{M_s} \frac{\partial m_y(z)}{\partial z} \Big|_{z=0} + i\frac{\omega}{\gamma} \mathcal{M}_z \\ = M_s d \left(\frac{1}{d} \int_{z=0}^{z=d} h_y(z) dz \right) \end{aligned} \quad (3.73)$$

where \mathcal{M}_y and \mathcal{M}_z , the components of the magnetization per unit area of the film, have been defined as:

$$\mathcal{M}_y = \int_{z=0}^{z=d} m_y(z) dz ; \quad \mathcal{M}_z = \int_{z=0}^{z=d} m_z(z) dz \quad (3.74)$$

The four boundary conditions (3.64)–(3.67) derived in section 3.2.5 can be used to replace the surface derivatives of m_y and m_z in (3.72) and (3.73) with the surface anisotropy fields (3.60) and (3.63). Since the film thickness is much less than the rf skin depth, we can also write:

$$m_y(0) \approx m_y(d) \approx \frac{\mathcal{M}_y}{d} ; \quad m_z(0) \approx m_z(d) \approx \frac{\mathcal{M}_z}{d} ; \quad \frac{1}{d} \int_{z=0}^{z=d} h_y(z) dz \approx h_0 \quad (3.75)$$

where $h_0 = h_y(0)$ is the driving rf magnetic field at the front surface of the film.

Making these substitutions in (3.72) and (3.73) yields:

$$-i\frac{\omega}{\gamma} \mathcal{M}_y + \left[\mathcal{B}_z - i\frac{\omega}{\gamma} \left(\frac{G}{\gamma M_s} \right) \right] \mathcal{M}_z = 0 \quad (3.76)$$

$$\left[\mathcal{H}_y - i\frac{\omega}{\gamma} \left(\frac{G}{\gamma M_s} \right) \right] \mathcal{M}_y + i\frac{\omega}{\gamma} \mathcal{M}_z = M_s dh_0 \quad (3.77)$$

where

$$\mathcal{B}_z = H + (4\pi D_z M_s)_{\text{eff}} + \frac{K_1^{\text{eff}}}{2M_s} [3 + \cos 4\theta] \quad (3.78)$$

$$\mathcal{H}_y = H + \frac{2K_1^{\text{eff}}}{M_s} \cos 4\theta \quad (3.79)$$

$$(4\pi D_z M_s)_{\text{eff}} = 4\pi D_z M_s - \frac{2K_s}{M_s d}; \quad K_s = K_s^R + K_s^L \quad (3.80)$$

$$K_1^{\text{eff}} = K_1^{\text{bulk}} + K_1^{\text{surf}}; \quad K_1^{\text{surf}} = K_1^R + K_1^L \quad (3.81)$$

Equations (3.80) and (3.81) show that the surface anisotropies enter the integrated equations of motion in the same way as bulk anisotropy fields but they are inversely proportional to the thickness of the film. The contributions of the surface fields at the front and the rear of the slab are indistinguishable in a given film. We have therefore combined the front and rear surface anisotropy coefficients to form the combined coefficients, K_s and K_1^{eff} .

3.3.2 The Ferromagnetic Resonance Condition

As mentioned in the introduction to this chapter, ferromagnetic resonance experiments measure the derivative of the microwave absorption as a function of the externally applied magnetic field H . The resulting resonance curve is characterized by a resonance field, H_{FMR} , corresponding to maximum power absorption, and a linewidth, ΔH , defined as the field interval between the extrema of the absorption derivative. In order to calculate the microwave power, P_a , absorbed by our ultrathin film (and hence determine H_{FMR} and ΔH in terms of the magnetic parameters) we note that the integrated equations of motion (3.76) and (3.77) are formally identical to the equation of motion for a single magnetic moment precessing in the effective fields defined by (3.78)-(3.81). The microwave power absorbed by the equivalent single moment is (Gurevich, 1963):

$$P_a = \frac{1}{2} \omega \text{Im} [\chi_y] |h_o|^2 \quad (3.82)$$

and hence the response of our model ultrathin film to the applied microwave magnetic field, $h_o = h_y(0)$, is determined by the imaginary part of the integrated susceptibility $\chi_y = \mathcal{M}_y / h_o$:

$$\chi_y = \frac{M_s d \left[\mathcal{B}_z - i \frac{\omega}{\gamma} \left(\frac{G}{\gamma M_s} \right) \right]}{\left[\mathcal{B}_z - i \frac{\omega}{\gamma} \left(\frac{G}{\gamma M_s} \right) \right] \left[\mathcal{H}_y - i \frac{\omega}{\gamma} \left(\frac{G}{\gamma M_s} \right) \right] - \left(\frac{\omega}{\gamma} \right)^2} \quad (3.83)$$

Ferromagnetic resonance occurs when the denominator in (3.83) is a minimum and both $\text{Im}[\chi_y]$ and the absorbed power, P_a , are a maximum. This condition is fulfilled when the real part of the denominator becomes zero:

$$\mathcal{B}_z \mathcal{H}_y - \left(\frac{\omega}{\gamma}\right)^2 \left[1 + \left(\frac{G}{\gamma M_s}\right)^2\right] = 0 \quad (3.84)$$

The contribution of magnetic damping to the FMR condition is small and can often be neglected. For example, the largest values of the Gilbert damping parameter, G , the saturation magnetization, M_s , and the gyromagnetic ratio, γ , that we measured in our work were $G \approx 2 \times 10^8 \text{ sec}^{-1}$, $M_s = 1715 \text{ Oe}$, and $\gamma = 1.84 \times 10^7 \text{ Oe}^{-1} \text{ sec}^{-1}$. Hence, $G/(\gamma M_s) \approx 0.006$ and $[1 + (G/(\gamma M_s))^2] \approx 1.000036$. Ignoring the damping correction leads to the FMR condition:

$$\left(\frac{\omega}{\gamma}\right)^2 = \mathcal{B}_z \mathcal{H}_y \quad (3.85)$$

or, in terms of the magnetic parameters:

$$\left(\frac{\omega}{\gamma}\right)^2 = \left[H_{\text{FMR}} + (4\pi D_z M_s)_{\text{eff}} + \frac{K_1^{\text{eff}}}{2M_s} (3 + \cos 4\theta) \right] \left[H_{\text{FMR}} + \frac{2K_1^{\text{eff}}}{M_s} \cos 4\theta \right] \quad (3.86)$$

Equation (3.86) summarizes, in part, the power of FMR. All of the magnetic parameters contained in (3.86) can be determined from the measurement of H_{FMR} as a function of θ at two different microwave frequencies ω_1 and ω_2 . The angular dependence of H_{FMR} yields K_1^{eff} . Fitting the K_1^{eff} values obtained for several different film thicknesses, d , to (3.81) will sort out the contributions from the surface and the bulk in-plane anisotropies. The frequency dependence of H_{FMR} determines the gyromagnetic ratio, γ , and the effective demagnetizing field $(4\pi D_z M_s)_{\text{eff}}$. The g -factor is obtained from $\gamma = g|e|/(2mc)$ while the uniaxial surface anisotropy field, $H_s = 2K_s/(M_s d)$, is determined from $(4\pi D_z M_s)_{\text{eff}}$ through equation (3.80). The surface anisotropy field, H_s , scales with the film thickness as $1/d$. In very thin films the surface anisotropy field might be able to

overcome the demagnetizing field, $4\pi D_z M_s$, and pull the saturation magnetization out of the plane and along the specimen normal in zero applied field. This condition would correspond to a negative value for the effective demagnetizing field (ie, $(4\pi D_z M_s)_{\text{eff}} \leq 0$).

One cannot obtain a value for the saturation magnetization from (3.86) due to the presence of the uniaxial surface term in $(4\pi D_z M_s)_{\text{eff}}$. However, the peak-to-peak amplitude, I , of the measured FMR absorption derivative, dP_a/dH , is directly proportional to the integrated magnetic moment of the film, $M_s d$, and the incident rf microwave power $|h_o|^2$:

$$I \propto \frac{M_s d}{(\Delta H)^2} \left[\frac{H_{\text{FMR}} + (4\pi D_z M_s)_{\text{eff}}}{2H_{\text{FMR}} + (4\pi D_z M_s)_{\text{eff}}} \right] |h_o|^2 \quad (3.87)$$

where ΔH is the measured FMR linewidth. The measurement of $M_s d$ from the absorption derivative is considered in detail in the next section (section 3.3.3) where (3.87) is derived.

The experimental linewidth ΔH measured for ultrathin iron films is composed of two parts:

$$\Delta H = 1.16 \left(\frac{\omega}{\gamma} \right) \left(\frac{G}{\gamma M_s} \right) + \Delta H(0) \quad (3.89)$$

The frequency dependent part is due to intrinsic magnetic damping characterized by the Gilbert damping parameter, G . Intrinsic damping arises from spin orbit contributions to the electron valence band energies (Kambersky, 1976). The "1.16" factor in front of the frequency dependent term must be empirically determined from the computer

program described in section 3.2 by feeding in values for G , γ , and M_s appropriate for a ferromagnetic metal and comparing the first term in (3.89) with the linewidth predicted by the program. The frequency independent part of the linewidth, $\Delta H(0)$, is caused by magnetic inhomogeneities (Heinrich et al., 1985). Local variations in the film thickness result in variations in the surface anisotropy fields which have a $1/d$ dependence. This effect would tend to increase with decreasing d . $\Delta H(0)$ therefore measures the quality of the magnetic film growth and could be as useful for characterizing ultrathin ferromagnetic films as photoluminescence linebroadening is for characterizing the quality of MBE grown III-V compounds (Heinrich et al., 1987b).

3.3.3 Extraction of the Saturation Magnetization

The saturation magnetization, M_s , cannot be uniquely determined from the measured values of H_{FMR} when a uniaxial perpendicular surface anisotropy is present (see section 3.3.2). In this section we derive an alternate method of determining the total magnetic moment per unit area, $M_s d$, of an ultrathin film from the peak-to-peak amplitude of the measured FMR absorption derivative. We start by noting that the measured FMR lineshape is Lorentzian (Gurevich, 1951) and that the peak-to-peak amplitude, I , is therefore proportional to $P_a(H_{\text{FMR}})/\Delta H$ where $P_a(H_{\text{FMR}})$ is the absorption maximum and ΔH is the experimental linewidth. The maximum power absorption is obtained from (3.82):

$$P_a = \frac{1}{2} \omega \text{Im} [\chi_y] |h_o|^2$$

by evaluating the susceptibility (3.83) at resonance and taking the imaginary part:

$$\text{Im} [\chi_y(\text{FMR})] = \frac{M_s d \mathcal{B}_z}{\frac{\omega}{\gamma} \left(\frac{G}{\gamma M_s} \right) [\mathcal{B}_z + \mathcal{H}_y]}$$

In view of (3.89) we associate the quantity $(\omega/\gamma)G/(\gamma M_s)$ with the total linewidth ΔH and write:

$$\text{Im} [\chi_y(\text{FMR})] = \frac{M_s d \mathcal{B}_z}{\Delta H [\mathcal{B}_z + \mathcal{H}_y]} \quad (3.90)$$

or, ignoring the small shifts due to in-plane magnetocrystalline anisotropies*:

$$\text{Im} [\chi_y] \approx \frac{M_s d}{\Delta H} \left[\frac{H_{\text{FMR}} + (4\pi D_z M_s)_{\text{eff}}}{2H_{\text{FMR}} + (4\pi D_z M_s)_{\text{eff}}} \right] \quad (3.92)$$

The peak-to-peak amplitude, I , of the absorption lineshape is therefore

$$I \propto \frac{P_a(H_{\text{FMR}})}{\Delta H} \approx \frac{1}{2} \omega \frac{M_s d}{(\Delta H)^2} \left[\frac{H_{\text{FMR}} + (4\pi D_z M_s)_{\text{eff}}}{2H_{\text{FMR}} + (4\pi D_z M_s)_{\text{eff}}} \right] |h_o|^2 \quad (3.93)$$

To measure the magnetization, M_s , with this technique requires a reference sample of known magnetization, M_s^{ref} . Since we do not know the values of the driving microwave magnetic fields, h_o , across the surface of the films, we also need an ESR reference marker such as the paramagnetic salt DPPH in order to measure the ratio of the driving field, h_o , for the two experiments. The procedure for measuring M_s is as follows: first, a small amount of DPPH is dissolved in benzene and painted onto a thin paper disc. The disc is then placed on top of the surface of the reference specimen and FMR measurements carried out as described in section 3.3.2. One observes, in addition to FMR, the

* $2K_1/M_2 \approx 600$ Oe in bulk iron ($K_1 = 4.8 \times 10^5$ ergs/cm³, $M_s = 1715$ Oe)

ESR signal due to the DPPH. This yields values for the peak-to-peak amplitude, I_{ref} of the reference specimen, $H_{\text{FMR}}^{\text{ref}}$, ΔH_{ref} and $(4\pi D_{\perp} M_s)_{\text{eff}}^{\text{ref}}$ which can be used in (3.93) to calculate:

$$I_{\text{ref}} = \eta \frac{M_s^{\text{ref}} d_{\text{ref}}}{(\Delta H_{\text{ref}})^2} f\left(H_{\text{FMR}}^{\text{ref}}, (4\pi D_{\perp} M_s)_{\text{eff}}^{\text{ref}}\right) |h_o^{\text{ref}}|^2 \quad (3.94)$$

where η is an unknown constant of proportionality that depends on the spectrometer, $f(H_{\text{FMR}}, (4\pi D_{\perp} M_s)_{\text{eff}})$ is the term in square brackets in (3.93), and h_o^{ref} is the unknown value of the microwave driving field. The peak-to-peak amplitude, $I_{\text{ref}}^{\text{DPPH}}$, of the DPPH ESR peak also measures the driving field:

$$I_{\text{ref}}^{\text{DPPH}} = \kappa |h_o^{\text{ref}}|^2 \quad (3.95)$$

where κ is constant of proportionality that depends on the magnetic properties of the DPPH, the dimensions of the paper disc, and the spectrometer. Dividing (3.94) by (3.95) yields an expression that is independent of the driving field:

$$I_{\text{ref}}^0 = \frac{I_{\text{ref}}}{I_{\text{ref}}^{\text{DPPH}}} = \frac{\eta}{\kappa} \frac{M_s^{\text{ref}} d_{\text{ref}}}{(\Delta H_{\text{ref}})^2} f\left(H_{\text{FMR}}^{\text{ref}}, (4\pi D_{\perp} M_s)_{\text{eff}}^{\text{ref}}\right) \quad (3.96)$$

The sample whose magnetization we wish to determine now replaces the reference specimen in the spectrometer. The same paper disc painted with DPPH is placed on top of the sample and FMR measurements carried out to determine I_{samp} , $H_{\text{FMR}}^{\text{samp}}$, ΔH_{samp} and $(4\pi D_{\perp} M_s)_{\text{eff}}^{\text{samp}}$. The result is a second intensity expression:

$$I_{\text{samp}} = \eta \frac{M_s d}{(\Delta H_{\text{samp}})^2} f\left(H_{\text{FMR}}^{\text{samp}}, (4\pi D_z M_s)_{\text{eff}}^{\text{samp}}\right) |h_o^{\text{samp}}|^2 \quad (3.97)$$

and a second DPPH marker intensity

$$I_{\text{samp}}^{\text{DPPH}} = \kappa |h_o^{\text{samp}}|^2 \quad (3.98)$$

where η and κ have the same values as they do in (3.94) and (3.95). Combining (3.97) and (3.98) results in:

$$I_{\text{samp}}^0 = \frac{I_{\text{samp}}}{I_{\text{samp}}^{\text{DPPH}}} = \frac{\eta}{\kappa} \frac{M_s d}{(\Delta H_{\text{samp}})^2} f\left(H_{\text{FMR}}^{\text{samp}}, (4\pi D_z M_s)_{\text{eff}}^{\text{samp}}\right) \quad (3.99)$$

Dividing (3.99) by (3.96), eliminates the constants of proportionality and yields the ratio of the magnetizations for the unknown sample and the reference specimen in terms of known quantities:

$$\frac{M_s d}{M_s^{\text{ref}} d_{\text{ref}}} = \left(\frac{I_{\text{samp}}}{I_{\text{samp}}^{\text{DPPH}}} \cdot \frac{I_{\text{ref}}^{\text{DPPH}}}{I_{\text{ref}}} \right) \frac{(\Delta H_{\text{samp}})^2}{(\Delta H_{\text{ref}})^2} \frac{f\left(H_{\text{FMR}}^{\text{ref}}, (4\pi D_z M_s)_{\text{eff}}^{\text{ref}}\right)}{f\left(H_{\text{FMR}}^{\text{samp}}, (4\pi D_z M_s)_{\text{eff}}^{\text{samp}}\right)} \quad (3.100)$$

Chapter 4

Ultrathin Iron Film Growth

4.1 Introduction

The ultrathin bcc Fe(001) films used in this work were grown on bulk Ag(001) single crystal substrates and either covered with 30-60Å coverlayers of Ag(001) and/or Au(001) or left bare. The {Ag/Fe}, {Au/Fe}, and {vacuum/Fe} interfaces allowed the effect of different interfaces on the overall magnetic properties of ultrathin iron to be investigated. The Au coverlayers also served to protect the Fe and Ag/Fe films from oxidation when they were removed from the MBE facility for measurement in one of the external FMR spectrometers.

Silver and gold were natural choices for the substrate and coverlayer materials. Theoretical studies of ultrathin film growth carried out by van der Merwe (1982) have indicated that a necessary condition for good layer-by-layer epitaxial film growth is a substrate whose lattice spacing matches, or very nearly matches, that of the film material. When the (001) face of Ag or Au is rotated by 45°, the surface looks like a regular square array of atoms having lattice spacings of 2.88Å (for Ag) and 2.89Å (for Au). These surface nets are well matched to the (001) surface of bcc Fe, which consists of a square array of atoms 2.87Å on a side. The situation is illustrated in Fig. 4.1 where one monolayer of Fe is shown growing on top of Ag(001). Silver was chosen for the substrate material because Bader and Moog (1987) have shown that iron will not grow on gold in a layer by layer fashion. In contrast, LEED and Auger studies by Smith et al. (1982) have shown that iron grows layer by layer on Ag(001) for at least the first 3 ML.

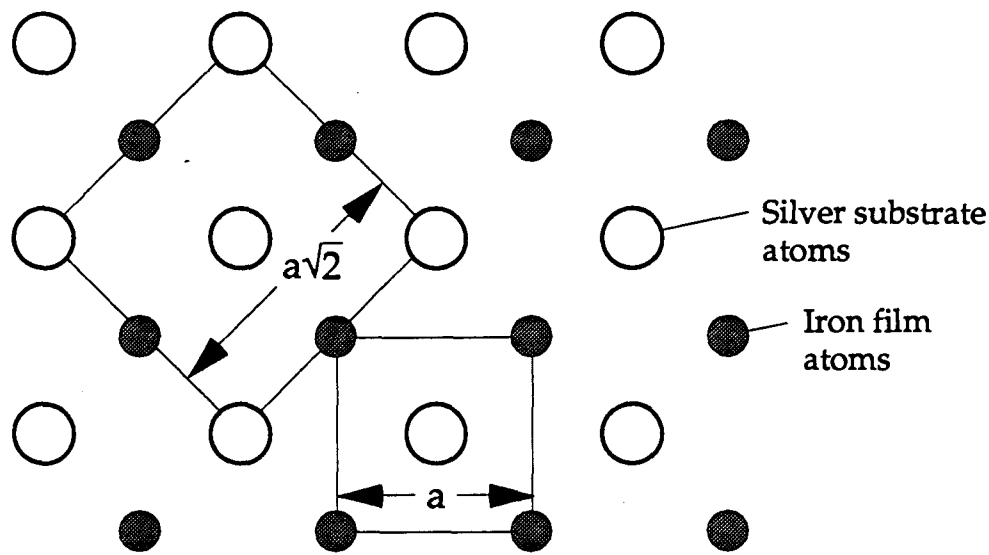


Fig. 4.1 Schematic depiction of the growth of bcc Fe on a (001) surface of fcc Ag. After a 45° rotation, the silver surface net matches the (001) fcc Fe surface net to within 0.6%. The spacing " a " of the rotated Ag(001) surface net is 2.8839\AA while that of bulk Fe(001) is 2.8665\AA . Such a close match is essential for good epitaxial growth of one material on another.

Our goal in this thesis was to investigate the magnetic properties of *well defined* ultrathin iron films; that is, bcc Fe(001) films possessing flat, smooth surfaces and uniform thicknesses. It was therefore important to determine the physical structure of the films we grew. To that end we have carried out an extensive study of the MBE growth of our Fe, Ag, and Au films using RHEED, Auger, and XPS. The results we obtained are consistent and reproducible.

The most important result is that RHEED intensity oscillations, described in section 2.6.6 of chapter 2, were observed during the room temperature growth of 2–15ML Fe films on Ag(001) and during the growth of 15–30ML films of both Ag or Au on ultrathin bcc Fe(001). RHEED oscillations indicate epitaxial layer by layer film growth. We can therefore be confident that we have grown well defined ultrathin film structures.

RHEED patterns indicated that the iron films were characterized by slightly rough, three dimensional surfaces. The amount of roughness increased with film thickness and was very likely limited to the surface monolayer since all RHEED features associated with three dimensional surface structure vanished when less than 0.1ML of Ag was deposited on the Fe film. The Au and Ag coverlayers grew much more smoothly than the Fe films. The RHEED patterns associated with Au or Ag layers always indicated that they were atomically flat and smooth over wide areas.

Low temperature Fe growths were carried out using Ag substrates cooled to 140K. We found that Fe still grows epitaxially on Ag at 140K although the film surfaces were much rougher than those grown at 300K (see section 4.5). Angular resolved XPS carried out while a 3.4ML Fe film grown at 140K was being warmed to room temperature failed to show any interdiffusion of Ag atoms into the Fe film. This is evidence that Fe films grown on Ag at 300K should have atomically sharp interfaces free from intermixing.

A majority of the iron films were grown upon Ag(001) substrates that were misoriented by $\sim 1.8^\circ$ from the (001) plane. The surfaces of these substrates consisted of numerous atomic step edges $\sim 2\text{\AA}$ high separated by short terraces $\sim 40\text{\AA}$ wide. RHEED oscillations and AES thickness measurements both indicated that the large vertical mismatch between Fe and Ag lattices along these step edges resulted in uneven surface coverage by the Fe atoms until 3ML of Fe had been deposited (corresponding to the deposition of one complete bcc Fe unit cell). This limited our investigation into the magnetic properties of well-defined, ultrathin iron films to 3ML or thicker films.

4.2 Preparing the Silver Substrates for Growth

Five different Ag(001) substrates were used in this investigation. All of them were roughly 22 mm in diameter and 3 mm thick. The first three, referred to as Ag[I], Ag[II], and Ag[III], were cut from a boule having a mosaic structure; that is, the substrates consisted of many small single crystal grains, each grain misaligned by $\sim 1^\circ$ from its neighbours. The substrates were also misoriented by approximately 1.8° from the (001) plane. We shall refer to these as "vicinal" substrates, a term coined by Cohen et al. (1987). Since the spacing between successive layers of silver atoms parallel to the (001) surface is 2.09\AA , the vicinal substrate surfaces consisted of numerous 2\AA high step edges separated by small terraces the order of $2\text{\AA}/\tan(1.8^\circ) \approx 40\text{\AA}$ wide. The other two substrates, Ag[IV] and Ag[V], were cut from a boule free of mosaic spread and were carefully oriented so that their surfaces were aligned to within $\pm 0.25^\circ$ of the (001) plane. Such substrates have been called "singular". Their surfaces consisted of much wider terraces approximately 500\AA wide.

Following cutting and alignment, the substrates were mechanically ground and polished using the techniques described in Appendix B. Final polishing was carried out electrochemically using a cyanide free electropolish. This left the substrate surfaces clean and bright with a slight "lemon peel" finish characteristic of electro-polishing (Tegart, 1959). Lemon peel indicates a macroscopic surface roughness which has a length scale on the order of 0.01 mm. As shown later in this section, this long range disorder is quite unobservable by means of RHEED and does not affect the quality of the substrate on the atomic scale.

After final ultrasonic cleaning in methanol, the substrates were attached to one of the MBE specimen holders using Mo clips as shown in Fig. 4.2. The singular substrates

were used for *in-situ* FMR work. As shown in Fig. 4.2(b), slots were cut in their sides so that the clips would not obstruct the surface which was required to fit flush against the opening of the FMR resonant cavity (see section 2.8.3). Vicinal substrates were used exclusively for FMR measurements outside UHV and they were attached to the MBE specimen holders by means of front surface clips as shown in Fig. 4.2(a). Once mounted on the end of the specimen manipulator arm in the MBE intro-chamber, the substrates would either be left in the intro-chamber to outgas overnight or, if needed immediately, heated to ~ 120 °C for 30 minutes in the intro-chamber to hasten outgassing and then left to cool for two hours before insertion into the UHV analysis chamber.

Silver is highly reactive with oxygen and sulfur. Although the substrates looked visually clean upon entry into the Analysis chamber, Auger and XPS measurements revealed that the substrate surfaces were often highly contaminated with these two elements. It was not uncommon to find 20-30 atomic percent (at.%) of oxygen on the surface (ie, 1 in 5 to 1 in 3 surface atoms were oxygen). The singular substrates, Ag[IV] and

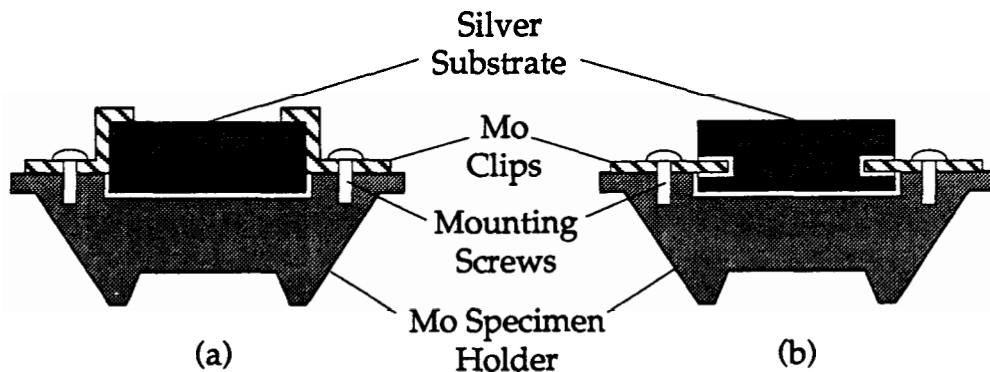


Fig. 4.2. Schematic diagram showing two methods used to mount a silver substrate in MBE machine specimen holder. (a) The substrate is held in place with two Molybdenum spring clips attached to the Mo specimen holder by screws. (b) Two grooves are cut into the substrate and clips inserted into the grooves to hold the substrate against the holder. In both cases the recess in the Mo holder kept the substrate centered in its mount.

Ag[V], showed traces of Antimony (Sb) which must have been inadvertently incorporated into the silver when the boule was grown.

Removal of the surface contaminants from the substrates was accomplished by means of sputtering the substrates for 30 minutes at room temperature using Ar^+ ions accelerated through a 2 keV potential. The ions were produced by electron bombardment of Ar atoms in an ion gun aimed at the surface of the substrate. The Ar was supplied by back filling the analysis chamber with Ar to a pressure of 5×10^{-5} Torr. AES and/or XPS analysis following sputtering always showed the substrate to be free from surface contamination within the limit of resolution of the spectrometers (± 0.03 at.%). Since sputtering involves ion bombardment of the specimen, it causes surface damage, leaving a few monolayers of disordered material on the single crystal. Crystalline perfection was restored by heating the substrate, by means of the substrate heater, to approximately 450 °C for 20-30 minutes. Higher temperatures were avoided. Substrate RHEED patterns indicated that annealing temperatures in excess of 600°C tended to produce a rough final surface. A surface roughened as a consequence of exposure to high temperatures could be restored to smoothness by continuing the annealing process for another 30 minute at a temperature of approximately 450 °C.

Annealing the singular substrates allowed Antimony atoms to diffuse from the bulk and thus to segregate on the surface. These were removed by re-sputtering the substrate for 5 minutes at the end of the above annealing process while the substrate was held at 450° C. The substrate heater was then turned off and the substrate allowed to cool slowly to room temperature. The slow cooling was sufficient to anneal out any defects caused by the final "hot" sputter. AES analysis following cooling showed no traces of Antimony.

Photographs of typical substrate RHEED patterns after annealing are shown in Fig. 4.3. The RHEED pattern of a singular Ag(001) substrate is shown in Figs. 4.3(a) and 4.3(b). The very short, sharp streaks are indicative of a nearly perfect surface flat over regions approximately 500\AA on a side. Comparing Fig. 4.3(a) with the RHEED pattern of a nearly perfect Fe[001] whisker facet shown in Fig. 2.8(a) indicates how well the singular substrates approached a nearly "perfect" surface. Fig. 4.3(b) is an overexposed version of Fig. 4.3(a) to bring out the complex Kikuchi patterns associated with the singular substrates. Kikuchi lines are present only when the atoms in the surface layers exhibit good three dimensional ordering over large areas. The presence of very small, sharp RHEED diffraction streaks and Kikuchi lines indicates the excellent quality of the singular substrates.

Fig. 4.3(c) exhibits the RHEED pattern for a vicinal substrate possessing mosaic structure. The longer, somewhat wider, streaks with intensity variations along their length indicate the presence of short range disorder. In this case, the disorder is primarily due to the 1.8° misalignment from the (001) plane which creates a step-like surface with each step (or terrace) having an average length of approximately 40\AA . Although not visible in the photographs, the vicinal substrates also exhibited Kikuchi patterns, an indication that the individual crystallites responsible for the mosaic structure of the substrate were quite large, at least several hundred angstroms on a side. Apparently, their presence had little effect on the overall quality of the vicinal substrates. The narrow, elongated RHEED streaks and the Kikuchi patterns showed that the 40\AA terraces of the vicinal substrates were flat and smooth on the atomic scale.

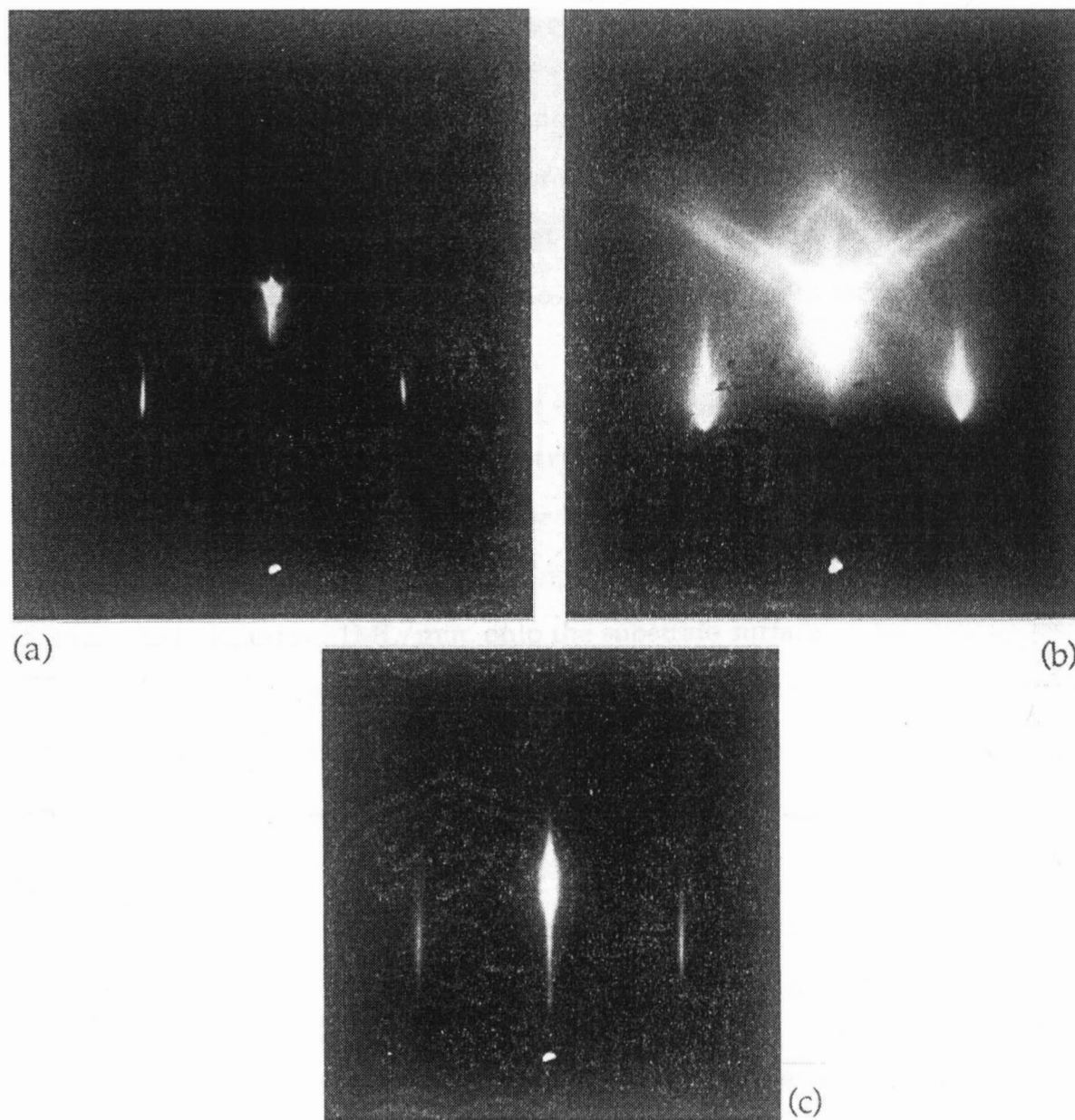


Fig. 4.3. Typical RHEED patterns for Ag substrates following sputtering and annealing just prior to growth of ultrathin Fe films. (a) Pattern along the [100] direction of a singular Ag(001) substrate misoriented less than $\pm 0.25^\circ$ from the (001) plane. (b) Same as (a) but overexposed to reveal Kikuchi patterns. (c) Pattern along the [100] direction of a vicinal Ag(001) substrate misoriented by 1.8° from the (001) plane. The sharp streaks and Kikuchi patterns of (a) and (b) are indicative of a nearly "perfect" surface flat over regions the order of 500\AA . Longer streaks with intensity variations along their length shown in (c) reflect the step-like surface of the vicinal substrate. For 1.8° misalignment, the steps causing the streaks are $\sim 40\text{\AA}$ in width.

4.3 The Growth of Iron on Bulk Silver Substrates

In all, fifteen different iron films, ranging in thickness from 2 to 28 ML, were grown on the five Ag(001) substrates. Thirteen of the films were grown at room temperature (~298K) while two of them were grown at 140K to investigate Fe film growth at low temperature. The latter two growths are described separately in section 4.5.

Fe film depositions were carried out in ambient background pressures of 10^{-10} Torr or less using MBE furnaces of the type described in section 2.4 of chapter 2. In these furnaces, a strand of pure Fe wire was wrapped around a tungsten filament and resistively heated to sublimation. A typical furnace input power of 80 Watts resulted in a beam of Fe atoms which deposited 1ML/min. onto the substrate surface. Film thicknesses were determined by means of the temperature controlled Mathis Quartz crystal thickness monitor described in section 2.3, by means of AES intensities, and by means of RHEED intensity oscillations. The AES thickness measurement technique has been described in section 2.74. The RHEED oscillation method was discussed in section 2.6.7. Typically, all three measurements techniques yielded film thicknesses in agreement to within ± 0.5 ML. This has been taken to be the uncertainty in the thickness of the grown films.

According to the RHEED patterns observed during Fe film deposition, all iron growths proceeded in a similar manner. Immediately upon opening the Fe furnace shutter to begin growth, the RHEED streaks would broaden and thicken, losing their intensity and quickly exhibiting a "spotty" structure. Fig. 4.4(a) shows the RHEED pattern along the [100] direction of a 3ML thick Fe film (note that this corresponds to the [110] direction on the Ag substrate surface – see Fig. 4.1). The diffuse background is a consequence of the random distribution of atomic steps and terraces on the surface of

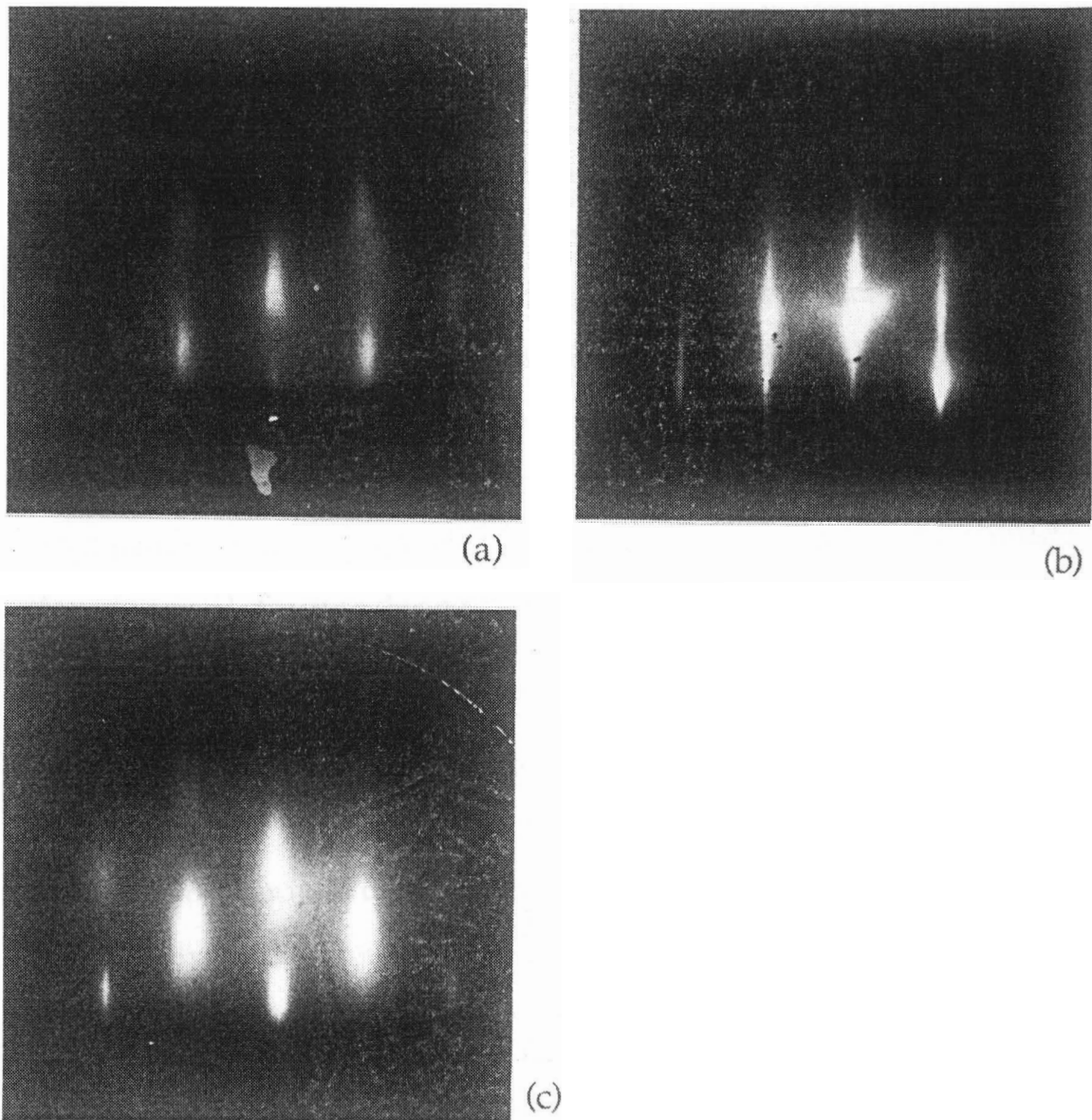


Fig. 4.4. RHEED patterns corresponding to ultrathin bcc Fe(001) films grown on bulk Ag(001) substrates. (a) A 3ML film of Fe grown on a vicinal substrate showing broad "spotty" streaks indicative of three dimensional surface roughening. (b) A 7.6ML Fe film grown on a singular substrate showing how surface roughening decreases in 4-8ML thick films. (c) A 28ML Fe film grown on a vicinal substrate showing how roughening increases markedly in films thicker than 8ML. All photographs are for the Fe [100] surface direction (which is the [110] Ag direction).

the film. RHEED beam transmission through the raised portions of these features results in the "spotty" streaks characteristic of a three dimensional surface (see section 2.6.5).

The surface roughness decreased at first but then tended to increase with film thickness. Figs. 4.4(b) and (c) show the RHEED patterns along the [100] surface direction of 7.6ML and 28.3ML Fe films. Three dimensional growth is evident. The roughness was dependent on whether or not the substrate was vicinal or singular. The RHEED patterns indicated that films grown on vicinal substrate were always much rougher than comparable films grown on singular substrates. Although not evident from Fig. 4.4, all Fe RHEED patterns exhibited Kikuchi lines. The iron films therefore maintained a good overall single crystal structure during growth.

The extreme surface sensitivity of RHEED exaggerates the extent of the surface roughness. When 0.1ML of Ag was deposited on a "rough" Fe surface, the wide spotty RHEED streaks would immediately become narrow and continuous while at the same time the diffuse background of the pattern noticeably darkened. The roughness of the iron films is likely confined to the surface monolayer.

The qualitative observation of RHEED patterns will only give information about the changing state of the film surface during growth. In order to determine the *way* in which a film is growing, one must monitor changes in the intensity of the spot on the RHEED pattern created by the electrons specularly reflected from the specimen surface. Extensive experimental and theoretical studies carried out during the growth of III-V semiconducting compounds have shown that regular oscillations in the intensity of the specular spot occur when a film is growing two dimensionally layer-by-layer on top of a substrate (Cohen et al., 1987, van Hove et al., 1983, Neave et al., 1983). The period of

one intensity oscillation corresponds to the growth of one monolayer. Recently, such oscillations have been observed for metal on metal epitaxy (Purcell et al., 1987) and provide a simple test for layer by layer growth.

RHEED oscillations were observed for Fe growths up to 14ML on both vicinal and singular Ag substrates. Oscillations in thicker films were not monitored. The oscillations recorded during the 14ML growth showed only a slight tendency to diminish in intensity towards the end of the growth. It is therefore likely that Fe grows layer by layer on Ag for much more than 14ML. Two representative RHEED intensity plots are shown in Fig. 4.5. According to the simple RHEED oscillation theory described in section 2.6.6, the strongest intensity oscillations should occur when the angles of incidence and reflection of the specular beam correspond to an anti-Bragg condition; ie, the portion of the RHEED beam reflected by the substrate is out of phase by $(2n-1)\pi$ from the portion of the beam reflected by the growing monolayer. In contrast, virtually no oscillations should be observed when the angles of incidence and reflection satisfy the Bragg condition (portion of the RHEED beam reflected by the substrate is in-phase with the portion of the beam reflected by the growing monolayer). Our results have indicated that one must indeed be close to satisfying the anti-Bragg condition in order to observe pronounced oscillations. Deviations from the anti-Bragg condition resulted in a considerable decrease in the intensity of the oscillations and the introduction of a large thickness-dependent background intensity. Consider the situations shown in Fig. 4.5(a) and Fig. 4.5(b). Fig. 4.5(a) shows the intensity oscillations monitored during the growth of 6ML of Fe on the singular substrate Ag[IV] when the π anti-Bragg condition was satisfied by the specular beam. Strong oscillations are apparent from the beginning to the end of the growth. Fig. 4.5(b) depicts the RHEED oscillations monitored during the growth of 14ML of Fe on the same singular substrate, Ag[IV], when the specular beam

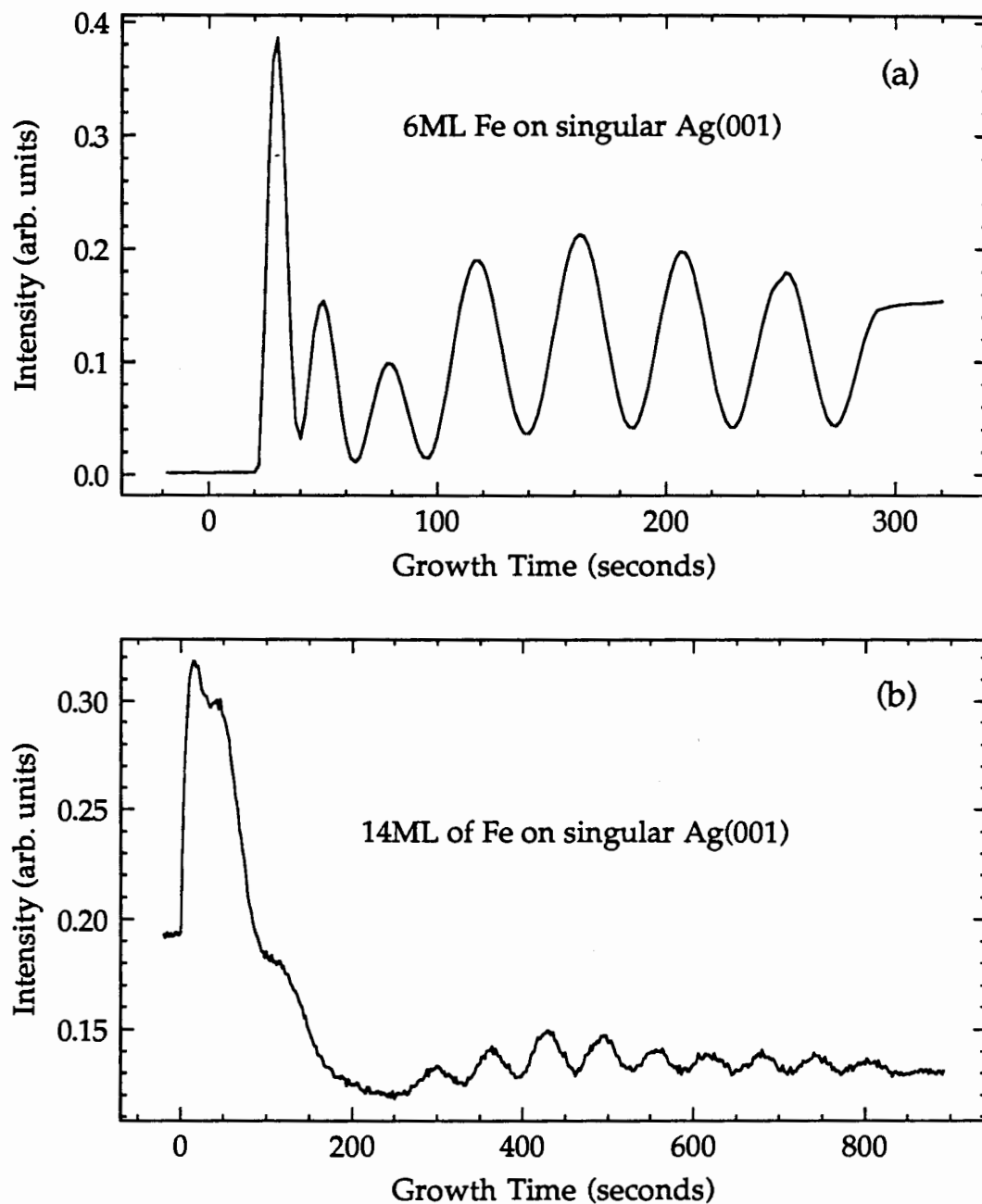


Fig. 4.5. RHEED Oscillations recorded for growths of bcc Fe(001) on bulk Ag(001) substrates. (a) Strong oscillations observed at the π anti-Bragg position for the growth of 6ML Fe on the singular substrate Ag[IV]. (b) Damped oscillations superimposed on a thickness dependent background observed half way between the 2π Bragg and the 3π anti-Bragg positions during the growth of 14ML of Fe on the singular substrate Ag[IV]. Oscillations, strong or weak, indicate layer by layer growth.

was approximately half-way between the 2π Bragg and the 3π anti-Bragg positions. In the latter case, a large thickness-dependent background signal was clearly superimposed upon a damped set of RHEED oscillations. In both figures, the vertical intensity scale was approximately the same. The large background and oscillations damping is likely due to dynamical scattering effects not accounted for by the simple kinematic theory we have been using to describe the RHEED oscillations. Note that RHEED oscillations similar to those shown in Fig. 4.5 (and in Fig. 4.7(a)) has been observed for the growth of Ni on W(110), Mo on W(110), and Cu on W(110) by Lilienkamp et al. (1988). Clearly, it is important to monitor RHEED oscillations at the $(2n-1)\pi$ anti-Bragg positions during metal-on-metal epitaxy.

RHEED oscillations observed during the growth of thinner Fe(001) films looked much like the early portions of the traces shown in Fig. 4.5(a). In all cases the period of the oscillations did not stabilize until approximately 3ML of Fe had been grown on top of the vicinal substrates and 2ML had been grown on the singular substrates (see Fig. 4.5(a)). Irregular oscillations indicate that growth is not proceeding in a layer-by-layer fashion and that successive monolayers are beginning to form before previous ones have been completed (Purcell et al., 1987, 1988a). An Fe film grown on a 12ML Ag substrate deposited on the essentially perfect surface of a [001] iron whisker facet exhibited layer by layer growth throughout the entire deposition, starting from the first monolayer (see Fig. 2 in Heinrich et al., 1988a). The poor oscillations observed in the initial stages of Fe grown on bulk Ag is likely due to the large vertical mismatch between the silver and the iron lattices. The spacing between successive silver monolayers in the [001] direction is 2.04\AA while the spacing between successive Fe(001) monolayers is 1.43\AA . This 43% difference could cause problems, particularly for the vicinal Ag substrates where every 40\AA or so one reaches the step-edge of a terrace and drops 2\AA down to the next

one. At least two monolayers of Fe would have to be grown on each Ag terrace before the Fe film atoms could bridge the large step-edges. Layer by layer growth could then proceed starting with the third monolayer. AES thickness measurements confirmed the poor initial coverage. When Fe films were grown thicker than 3 ML, the film thickness as measured by AES matched the thickness as measured by means of either RHEED oscillations or the Mathis quartz crystal thickness monitor to within 2%. When the film thickness was less than 3ML, the AES thickness estimate was often 7-17% less than that obtained from the thickness monitor. Disagreement between these two measures of film thicknesses indicates either that silver substrate atoms were intermixing with the iron atoms of the film, or that the iron was not uniformly covering the substrate. Intermixing was ruled out by angular resolved XPS (ARXPS) measurements carried out in conjunction with the 140K low temperature Fe growths described in section 5.5. ARXPS, described near the end of section 2.7.3, was used to monitor the surface region of a 3.4ML Fe film grown at 140K on vicinal Ag(001) while the film and substrate slowly warmed to room temperature. If intermixing of Fe and Ag was energetically favorable, then the silver XPS signal would increase during warming as the silver atoms diffused into the iron layer and the iron signal would decrease as the iron atoms diffused into the substrate. No such change in Fe or Ag XPS signals could be detected. The difference between the film thicknesses measured by RHEED oscillations and by AES for Fe films thinner than 3ML was likely due to poor initial coverage of the stepped Ag substrate surfaces by the depositing iron atoms.

To summarize, Fe films were grown epitaxially, layer by layer, on both vicinal and singular Ag(001) single crystal substrates at room temperature. The films exhibit some surface roughness that is likely confined to the surface monolayer. RHEED oscillations and AES thickness studies indicated that a full bcc unit cell (3ML of Fe) must be grown

on the terraced surfaces of the bulk vicinal silver substrates before layer by layer growth can begin. The layer by layer growth then continues up to at least 14ML. Since the RHEED pattern of a 28ML Fe film is essentially the same as the pattern for a 7.6ML film, layer by layer growth probably extends to at least 28ML in thickness.

4.4 The Growth of Silver and Gold Coverlayers on Iron Films

In order to investigate the effect of different coverlayers on the magnetic properties of ultrathin iron, many of the Fe films were covered with 30Å-60Å of Au(001) or of Ag(001). The Au coverlayers served to protect the iron films from almost immediate oxidation upon removal from UHV for *ex-situ* FMR measurement. Iron films covered with Ag received an additional 30Å of Au in order to protect the Ag from similar attack.

RHEED patterns observed during the growth of both Au and Ag on Fe show that both coverlayers grow epitaxially layer by layer on Fe for at least 15-20ML. The surfaces of the coverlayers were extremely smooth with very little roughness as indicated by the narrow RHEED streaks (see section 2.6.3). Typical RHEED patterns of Au(001) and Ag(001) coverlayers are shown in Fig. 4.6. Compare Fig. 4.6(a) with Fig. 4.4(c) to see how covering the rough 28ML Fe film with 30Å Au removed all traces of the three dimensional Fe surface features.

The Au coverlayers exhibited the classic Au "5 times" reconstruction pattern characteristic of the best MBE grown gold films (Zajac et al., 1985). MBE grown Au(001) undergoes a complicated reordering during growth that results in a unit cell containing 25 Au atoms. This results in the appearance of four additional streaks between the main RHEED streaks. Ag shows no such reconstruction, growing simply as fcc Ag(001) on bcc Fe(001) at room temperature.

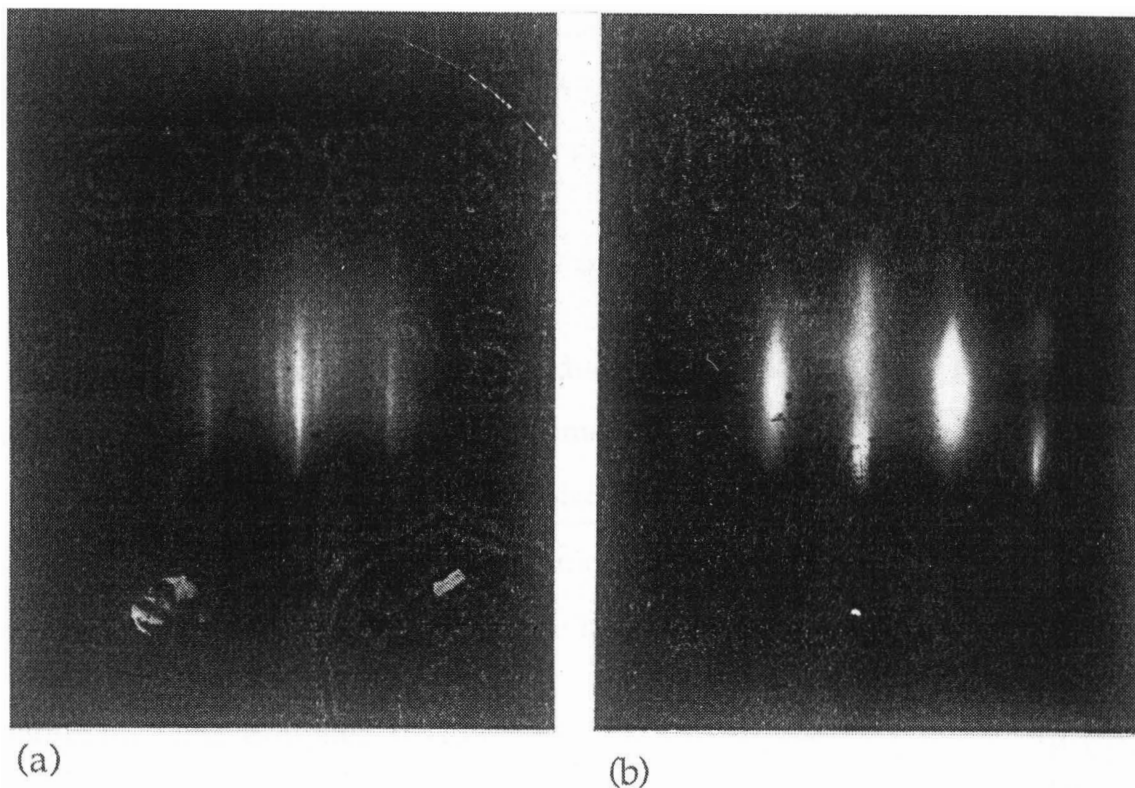


Fig. 4.6. RHEED patterns of Au and Ag capping layers grown on ultrathin Fe films deposited on bulk Ag substrates. (a) A 30Å Au film grown on a 28ML Fe film whose RHEED pattern was shown in Fig. 4.5(c). (b) A 30Å Ag film grown on the 7.6ML Fe film whose RHEED pattern was shown in Fig. 4.5(b). Note that the Ag and Au films are essentially flat and smooth compared with the slightly rough starting surfaces of the underlying Fe films.

Fig. 4.7 shows RHEED intensity oscillations recorded for the growth of $\sim 30\text{\AA}$ of Au and $\sim 30\text{\AA}$ of Ag on 3ML Fe(001) films deposited on vicinal Ag(001) substrates. Both sets of oscillations were monitored for a specular spot that did not quite satisfy the 3π anti-Bragg condition. As a result, the oscillations damped with increasing film thickness and were superimposed on a large thickness-dependent background much as in the case of Fe on Ag growth (see section 4.3). It is interesting to note that Fig. 4.7(a) for the growth of Au on Fe(001) is very similar to RHEED oscillations monitored away from an anti-Bragg position by Lilienkamp et al. (1988) during the growth of Ni on W(110) and of Cu on W(110) and shown in Fig. 4 of their paper.

4.5 The Effect of Low Temperatures on Iron and Silver Film Growth

In order to investigate the effect of reduced temperature on the growth of iron on bulk silver, and of silver on bcc Fe(001) films, two growths of 3.4ML Fe films were carried out on vicinal Ag(001) substrates cooled to approximately 140K. The cooling was accomplished by grasping the substrate holder between a pair of copper tipped, liquid nitrogen cooled, jaws mounted in the growth chamber shown in Fig. 2.1.

Both iron films exhibited irregular RHEED oscillations very much like those observed for room temperature growths of 3–4ML Fe films. The appearance of the RHEED patterns following growth indicated that the Fe film grown at 140K were much rougher than similar films grown at room temperature. In particular, the patterns exhibited a uniformly bright diffuse background indicative of a high density of point defects on the film surface. Kikuchi lines were also evident in the 140K growths although much weaker than at room temperature. The RHEED pattern of one of the 3.4ML films grown on Ag[III] is shown in Fig. 4.8(a). The patterns maintained their appearance during warming of the Fe film to room temperature. The RHEED patterns

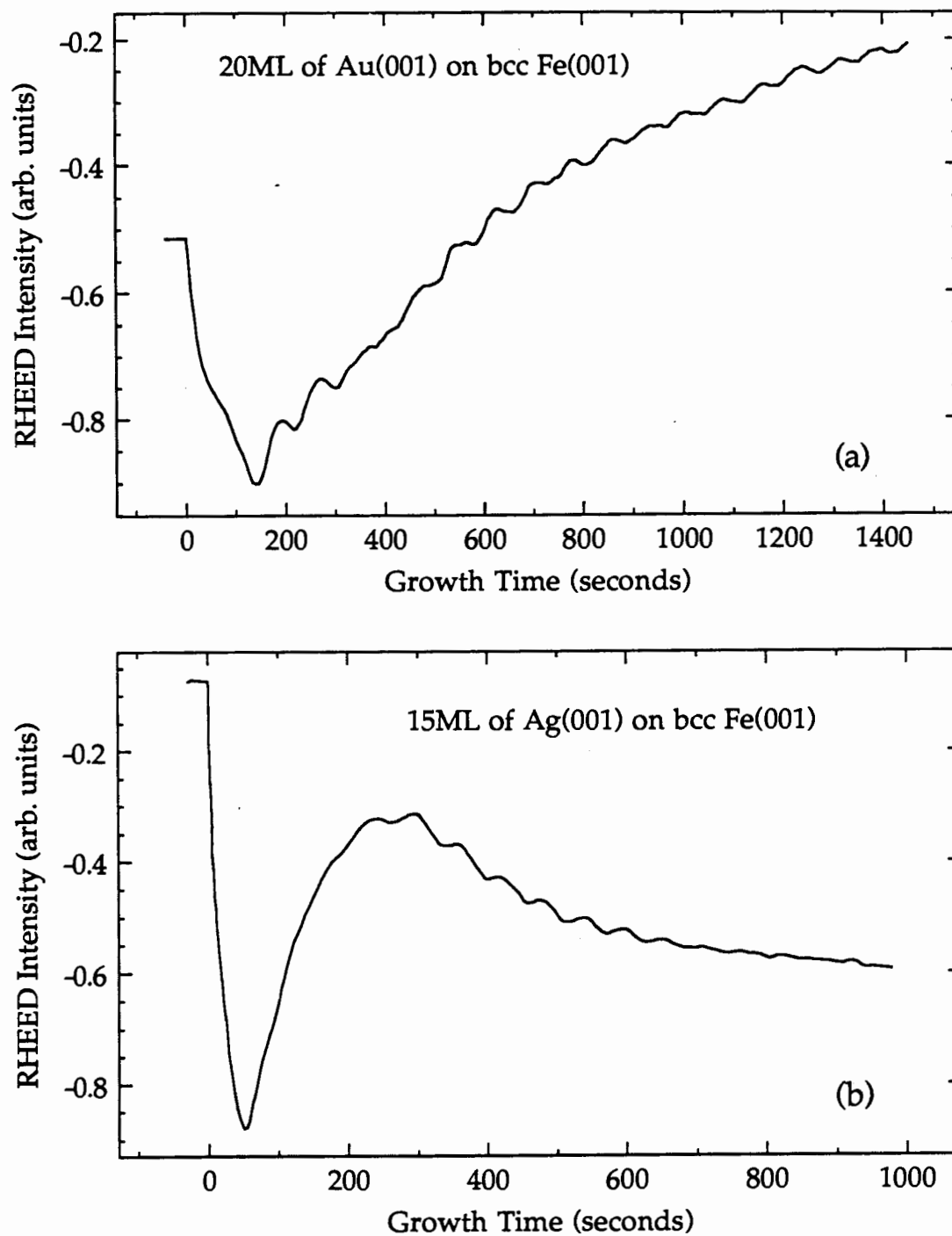


Fig. 4.7. RHEED Oscillations associated with the growth of Au and Ag on Fe(001) films. (a) Growth of 30\AA of Au on a 3ML Fe film grown on the vicinal substrate Ag[I]. (b) Growth of 30\AA of Ag on 3ML of Fe grown on the vicinal substrate Ag[II]. Good layer by layer growth of Au and Ag on the slightly rough Fe films is indicated.

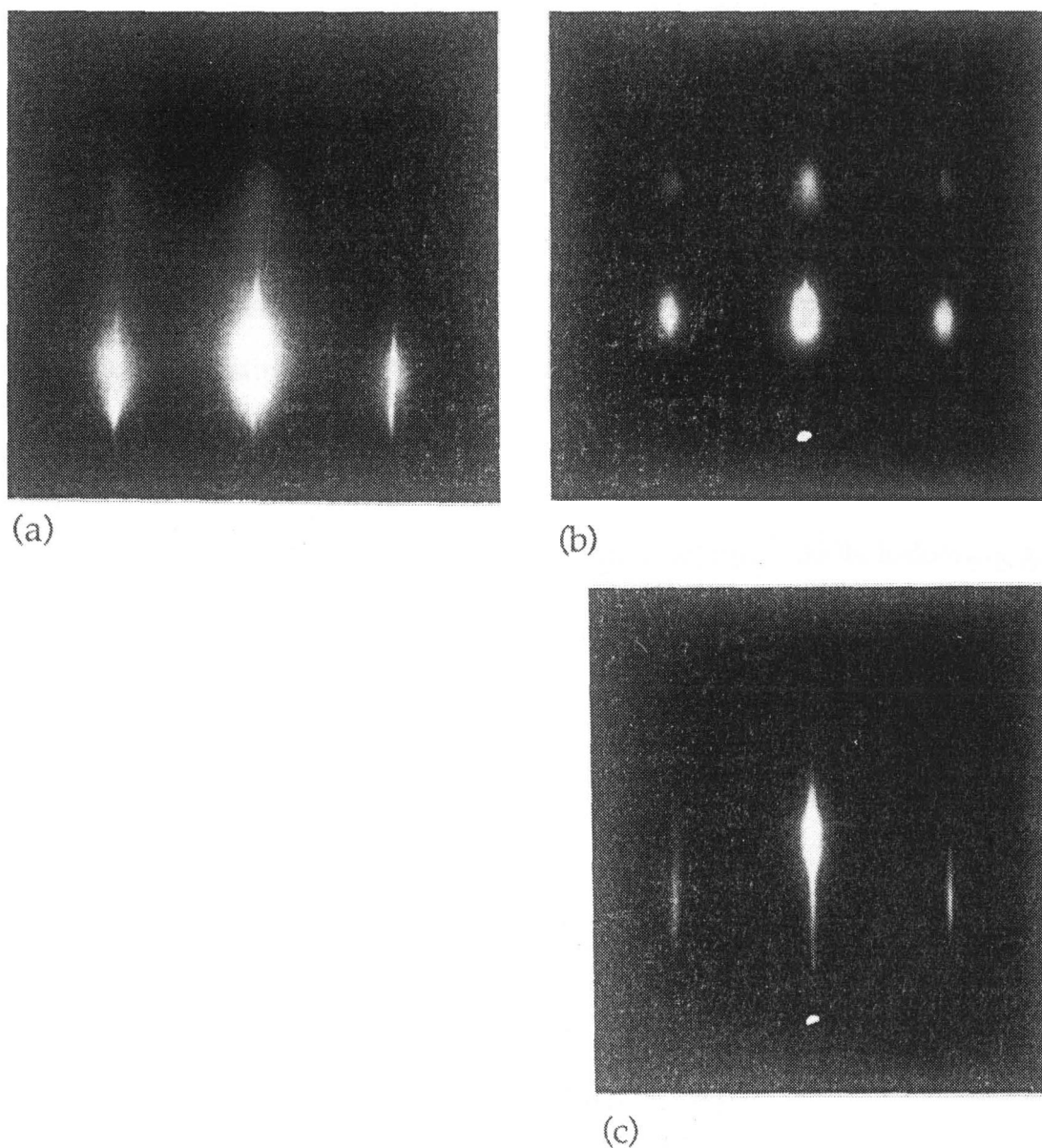


Fig. 4.8. RHEED patterns for (a) a 3.4ML bcc Fe(001) film grown on a vicinal Ag(001) substrate and (b) the same film covered with 30Å of Ag at 140K, and (c) the 30Å Ag film after annealing by warming to room temperature. Fe and Ag films grown at 140K were significantly rougher than Fe and Ag films grown at room temperature. Warming the Ag film slowly to room temperature annealed out the roughness. No such improvement in the Fe film quality was observed upon warming to 300K.

suggest that Fe atoms can diffuse across the surface of silver over a wide range of temperatures and grow as a single crystal even at reduced temperatures.

The first of the 3.4ML Fe films grown at 140K was covered with Ag at 140K in order to see how silver grows on iron at reduced temperatures. Fig. 4.8(b) shows the surface of the 30Å Ag(001) film just after deposition on the 3.4ML Fe(001) film. The strong three dimensional surface features indicated that Ag grows very poorly on Fe at 140K. However, slowly warming the Ag film to room temperature overnight was sufficient to anneal out the roughness and result in a very smooth Ag coverlayer (see Fig. 4.8(c)). In order to see if the quality of the Fe films could be improved by annealing, the second 3.4ML Fe film grown at 140K was allowed to slowly warm to 300K following growth. Unfortunately, annealing caused no noticeable improvement in the RHEED pattern for iron. The pattern observed at 300K was essentially the same as that observed at 140K.

Chapter 5

Results and Analysis

5.1 Introduction

In this chapter we present the results of a three-part investigation we have made into the magnetic properties of ultrathin iron films. The first set of experiments are described in section 5.3. FMR measurements were carried out *ex-situ* (ie, outside the ultra-high vacuum of the MBE facility) on 28, 17.2, 5.3, and 2.8 ML bcc Fe(001) iron films which had been grown at $T = 300\text{K}$ on vicinal* Ag(001) substrates and covered with 30\AA of Au(001). The measurements were made primarily to verify the presence and the origin of large uniaxial anisotropies which had been predicted to exist in ultrathin iron films by Gay and Richter (1986). We found that a large uniaxial surface anisotropy was indeed present in ultrathin iron films (Heinrich et al., 1987a).

All of the gold covered films exhibited a positive effective demagnetizing field, $(4\pi D_z M_s)_{\text{eff}}$ indicating that they were magnetized in the specimen plane in zero applied field. Our second set of experiments, described in section 5.4, were carried out to determine if replacing the gold coverlayer with silver would result in a specimen with $(4\pi D_z M_s)_{\text{eff}} < 0$; that is, a specimen whose spontaneous magnetization was oriented perpendicular to the plane in zero field. Since ultrathin films less than 3 ML thick did not exhibit layer-by-layer growth due to the large vertical mismatch along the silver substrate atomic steps only iron films approximately 3 ML thick were investigated (see

* The term "vicinal" refers to a single crystal substrate whose surface is not parallel with a low index plane. The vicinal Ag(001) substrates used in this work were misoriented by approximately 1.8° from the (001) plane.

section 4.3 and 4.5). *Ex-situ* FMR was used to measure the magnetic properties of three bcc Fe(001) films grown at $T = 300\text{K}$ on vicinal Ag(001) substrates and covered with 30 ML of Ag(001). The vicinal substrates possessed surfaces consisting of numerous atomic steps and terraces approximately 40\AA wide. In order to determine how this surface structure affected the uniaxial anisotropy, a 3 ML iron film was grown on a 15 ML Ag(001) layer deposited on the near perfect (001) surface of an iron whisker.

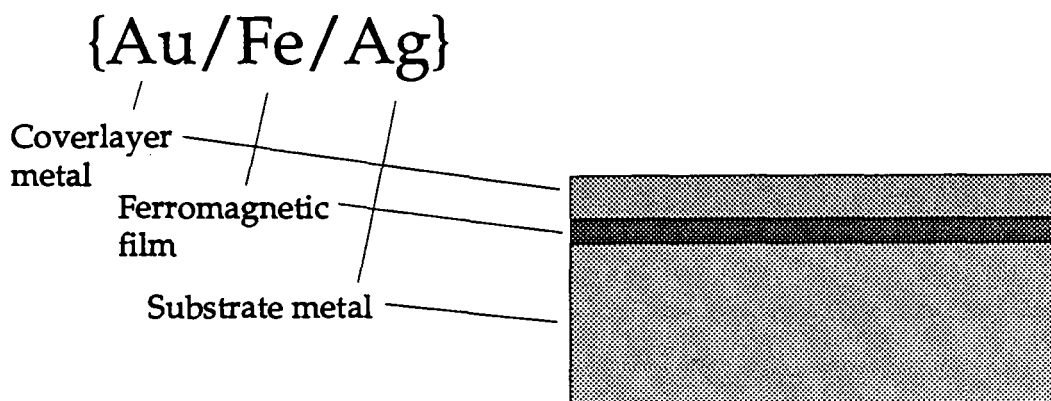
The theoretical calculations of Gay and Richter were primarily carried out for unsupported iron films. Our third set of experiments were therefore aimed at measuring the surface anisotropy associated with the vacuum/iron interface. A 16.88 GHz FMR spectrometer was installed in the MBE facility which could be used to measure FMR in applied magnetic fields up to 5.5 kOe without removing the specimen from the ultra-high vacuum (Urquhart et al., 1988). Seven iron films ranging in thickness from 5.1 to 14.2 ML were grown at $T = 300\text{K}$ on singular** Ag(001) substrates and measured with the *in-situ* FMR system without and with Ag covering layers. The results of these measurements are described in section 5.5.

FMR measurements also provide information about the dynamic magnetic properties of an ultrathin film. The resonance linewidth, ΔH , contains information about the magnetic damping processes in a film while the g-factor obtained from the resonance field, H_{FMR} , is a measure of the role that the spin-orbit interaction plays in the 3d bands of iron. In section 5.6 we show how a study of these properties can yield additional information useful in characterizing the structural and the intrinsic magnetic properties of an ultrathin film.

** The term "singular" refers to a single crystal substrate whose surface is very nearly parallel with a low index plane. The singular Ag(001) substrates used in these experiments were parallel to the (001) plane to within 0.25° .

5.2 Nomenclature

The following notation will be used to differentiate between the various types of specimens described in this chapter:



The coverlayer is listed first, followed by the ferromagnetic film material, and then by the substrate metal. The substrate is sometimes listed as Ag(001) in order to emphasize the fact that the film was grown on the (001) face. When no coverlayer was grown the specimen will be denoted by {Fe/Ag(001)}. Special structures grown on the (001) surface of an iron whisker are denoted by {Ag/Fe/Ag/Fe[001]} or {Au/Fe/Ag/Fe[001]} to indicate that a Ag(001) layer was grown on the Fe(001) whisker facet before the iron film was deposited. Two iron films were grown at $T = 140\text{K}$. They are denoted by {Ag/Fe/Ag(001)}₁₄₀ (ie, with a "140" subscript). All films without a subscript were grown at $T = 300\text{K}$.

5.3 Large Surface Anisotropies in Ultrathin Iron Films

Spin- and angle- resolved photoemission experiments carried out by Jonker et al. (1986) had suggested that the magnetization of iron films only a few atomic layers thick was oriented perpendicular to the specimen plane in zero applied field. This hypothesis was supported by the theoretical work of Gay and Richter (1986) which predicted that an unsupported monolayer of iron should possess a relatively large second-order (uniaxial) magnetocrystalline anisotropy energy whose sign and magnitude were such as to orient the magnetization perpendicular to the plane of the monolayer. Subsequent calculations by Gay and Richter (1987) indicated that this spin-orbit induced anisotropy energy had the form of the surface term $E_2 = -K_s \alpha_z^2$ which was included in the FMR absorption calculations of chapter 3 as a boundary condition on the magnetization (see section 3.2.5).

The predictions of large surface anisotropies led us to study the magnetic properties of ultrathin iron films using ferromagnetic resonance (FMR). This technique was chosen because a uniaxial surface anisotropy strong enough to pull the magnetization along the specimen normal would be readily detectable with FMR. As an example, consider a resonance experiment carried out on a 2 ML iron film using a 73 GHz spectrometer. Neglecting small variations due to in-plane anisotropy and magnetic damping, it was shown in section 3.3.2 that the applied field, H_{FMR} , corresponding to ferromagnetic resonance in an ultrathin film was given by:

$$\left(\frac{\omega}{\gamma}\right)^2 = H_{\text{FMR}} \left[H_{\text{FMR}} + (4\pi D_z M_s)_{\text{eff}} \right] \quad (5.1)$$

where

$$(4\pi D_z M_s)_{\text{eff}} = 4\pi D_z M_s - \frac{2K_s}{M_s d} \quad (5.2)$$

is the effective demagnetizing field composed of the true demagnetizing field, $4\pi D_z M_s$, and an effective field, $H_s = -2K_s/(M_s d)$, associated with the second-order surface anisotropy proposed by Gay and Richter. The quantity D_z is the ultrathin film demagnetizing factor (see Appendix A). For a 2 ML ($d = 2.86\text{\AA}$) iron film and 73 GHz microwave radiation, $(\omega/\gamma) = 25.0$ kOe, $D_z = 0.79$, and $4\pi D_z M_s = 17.9$ kOe (assuming $M_s = 1715$ Oe). In the absence of a uniaxial surface anisotropy, $(4\pi D_z M_s)_{\text{eff}} = 4\pi D_z M_s$ and equation (5.1) predicts that FMR would occur at $H_{\text{FMR}} = 17.9$ kOe. If a surface anisotropy just strong enough to orient the magnetization perpendicular to the plane in zero applied field is present, then $(4\pi D_z M_s)_{\text{eff}} \approx 0$ and the resonance field would be shifted upwards by 7.1 kOe to $H_{\text{FMR}} \approx (\omega/\gamma) = 25.0$ kOe. Such a large shift would be easily measured in the laboratory.

Our initial FMR studies were carried out on four {Au/Fe/Ag} films grown at $T = 300\text{K}$ on vicinal Ag(001) substrates and covered with 30\AA of Au(001). The depositions were carried out in the PHI Model 400 MBE facility described in chapter 2 using the growth procedures described in chapter 4. The average thicknesses of the films were 40, 24.7, 7.6, and 4.0\AA corresponding to 28.0, 17.3, 5.3, and 2.8 ML of Fe respectively. The film thicknesses were determined during deposition by means of a Mathis quartz crystal thickness monitor (section 2.3) and again after growth by measuring the decrease of the Ag $3d_{5/2}$ XPS signal from the silver substrates as described in section 2.7.4. The two thickness measurements agreed to within 3% in all four cases. The Ag substrates and the Fe films were extremely clean. AES and XPS scans revealed no traces of contamination within the resolving limits of the spectrometers (± 0.03 atomic %).

The FMR measurements were carried out *ex-situ* at $f_1 = \omega_1/(2\pi) = 73.0$ GHz and $f_2 = \omega_2/(2\pi) = 36.6$ GHz. The magnetic field corresponding to ferromagnetic resonance, H_{FMR} , and the resonance linewidth, ΔH , were measured at the two frequencies as a function of the angle θ between the applied magnetic field and the in-plane [100] direction. Values for the magnetic parameters characterizing the films were obtained by fitting the data to the ultrathin film resonance condition (section 3.3.2):

$$\left(\frac{\omega}{\gamma}\right)^2 = \left[H_{\text{FMR}} + (4\pi D_z M_s)_{\text{eff}} + \frac{K_1^{\text{eff}}}{2M_s}(3 + \cos 4\theta) \right] \left[H_{\text{FMR}} + \frac{2K_1^{\text{eff}}}{M_s} \cos 4\theta \right] \quad (5.3)$$

The fitting of data to (5.3) was carried out using MINUIT*, a multiparameter chi-squared function minimization program. The H_{FMR} vs. θ data measured at frequency ω_1 were fed into the program along with values for D_z and $\gamma = g|e|/(2mc)$. The bulk iron g-factor of $g = 2.09$ was initially assumed. The program would output values for $(4\pi D_z M_s)_{\text{eff}}$ and the effective in-plane anisotropy field $2K_1^{\text{eff}}/M_s$. The effective demagnetizing field would then be used in (5.1) to obtain the resonance field H_{FMR}^1 corresponding to zero in-plane anisotropy at the frequency ω_1 . The H_{FMR} vs. θ data measured at frequency ω_2 were then fitted to (5.3) to obtain a second set of values for $2K_1^{\text{eff}}/M_s$ and $(4\pi D_z M_s)_{\text{eff}}$. The latter would then be used in (5.1) to calculate the zero in-plane anisotropy field H_{FMR}^2 at ω_2 . A self-consistent value for the g-factor could then be calculated by substituting ω_1 , H_{FMR}^1 , ω_2 , and H_{FMR}^2 into (5.1) to obtain two simultaneous equations for $(4\pi D_z M_s)_{\text{eff}}$ and γ . The corrected g-factor was then used in (5.3) and two frequency fitting process repeated until the value of the g-factor calculated from (5.1) stabilized. Two iterations usually sufficed.

* Program available upon request from the Surface Physics Laboratory of Simon Fraser University.

The results of the fitting process carried out on the {Au/Fe/Ag} films are listed in Table 5.1. Representative FMR traces for each of the four specimens are shown in Figs. 5.1-5.4 along with plots of selected H_{FMR} vs. θ data. The latter plots include a solid curve calculated from equation (5.3) using the parameters of Table 5.1. The closeness of the fits gave us confidence in the simplified theory.

The saturation magnetizations, $4\pi M_s$, listed in Table 5.1 were obtained from absolute intensity measurements carried out at 73 GHz as described in section 3.3.3. The results show that the saturation magnetization in the specimens thicker than 5 ML was approximately that of bulk iron ($4\pi M_s = 21.55$ kOe) while the magnetization of the 2.8 ML film was approximately 30% lower at $T = 300\text{K}$. This is consistent with the measurements of $4\pi M_s$ reported by Stampanoni et al. (1987) for 0.8-10 ML iron films. They found that iron films thinner than 5 ML exhibited significantly reduced Curie temperatures, T_c . In particular, the saturation magnetization of a 3 ML film was found to increase by a factor of 1.5 upon cooling from $T = 300\text{K}$ to $T = 77\text{K}$. This enhancement factor can be used to estimate the saturation magnetization of our 2.8 ML film at low temperatures where thermal fluctuations are negligible. At $T = 300\text{K}$, the FMR absolute intensity measurements showed that $4\pi M_s = 15.2$ kOe in the 2.8 ML film. This would correspond to a saturation magnetization of 22.5 kOe at $T = 77\text{K}$ which is not significantly different from the bulk iron value. Our results therefore indicate that the magnetic moment per atom is not enhanced in low dimensional structures as predicted by the first principles band calculations of Fu et al. (1985) and of Richter et al. (1985).

The effective uniaxial anisotropy fields, $H_s = -2K_s/(M_s d)$, were calculated from equation (5.2) using the ultrathin film demagnetizing factors, D_z , of Appendix A. The uniaxial anisotropy coefficients, K_s , are only approximately given by (5.2) which as-

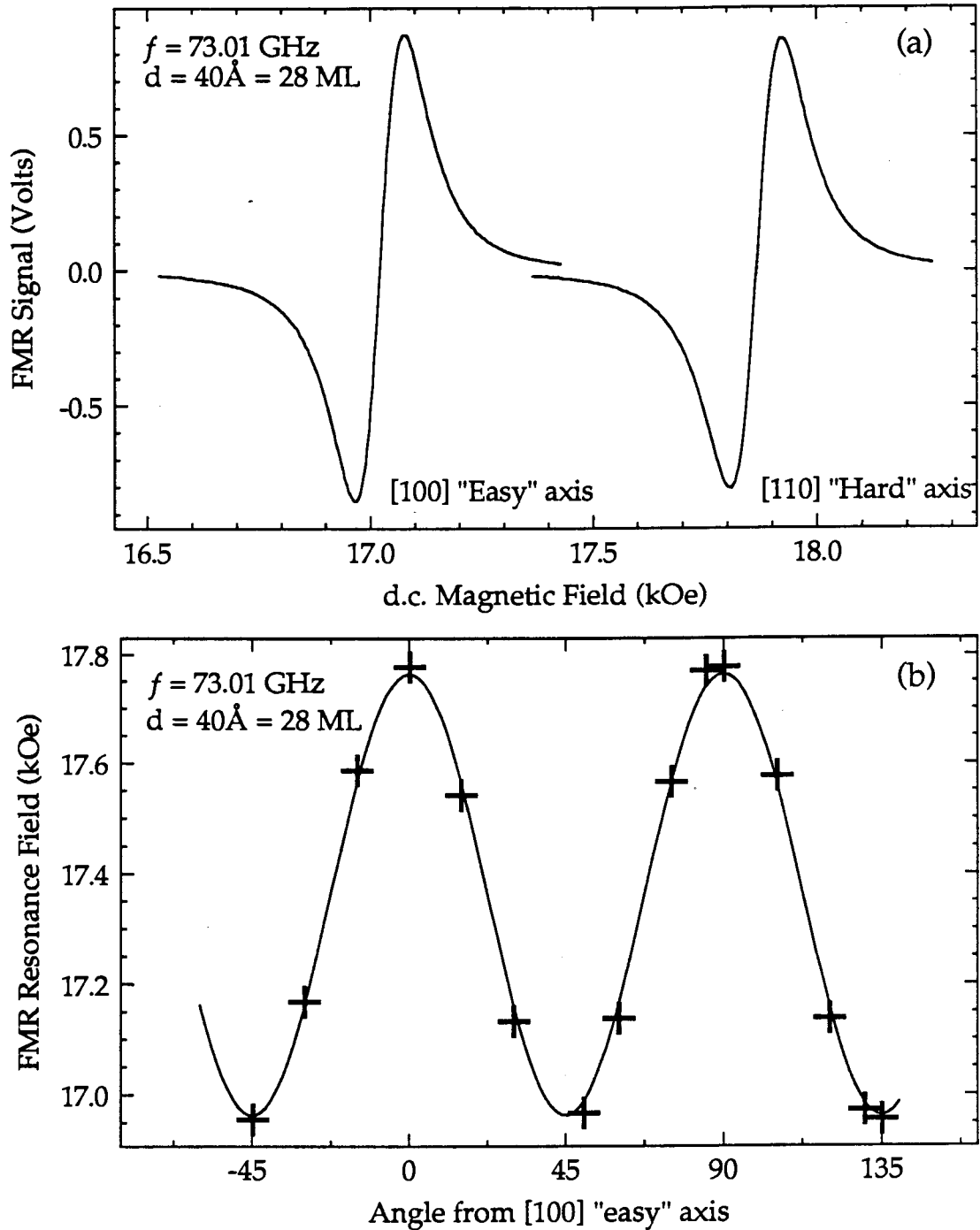


Fig. 5.1. (a) FMR absorption derivatives measured along the easy [100] and hard [110] directions of the 28 ML [Au/Fe/Ag] film at 73.01 GHz. (b) The variation of the resonance field H_{FMR} with angle θ in the plane measured from the [100] easy axis. The solid line shows the variation of H_{FMR} with θ calculated from the simplified FMR theory described in section 3.3 using the parameters listed in Table 5.1.

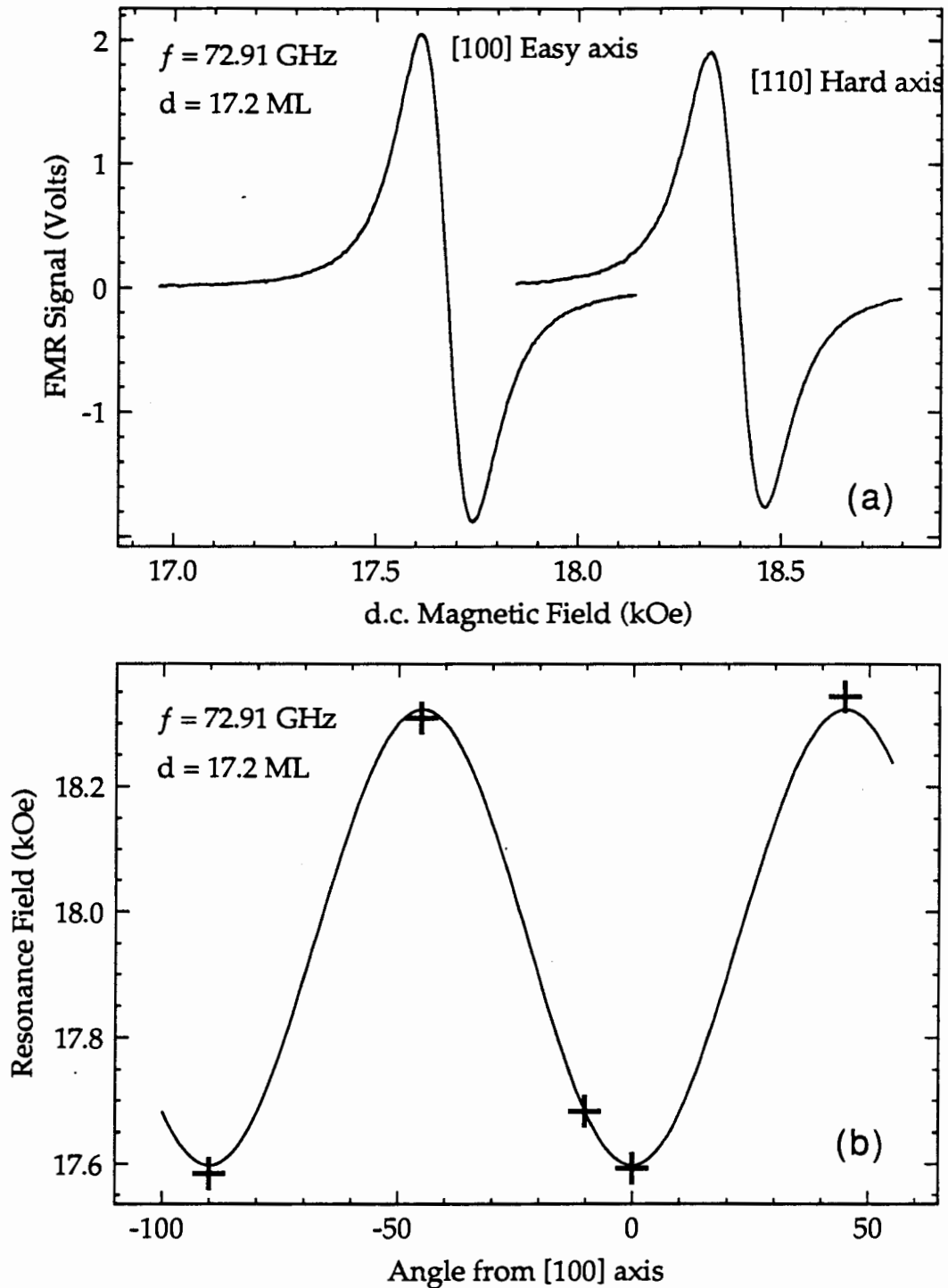


Fig. 5.2. (a) FMR absorption derivatives measured along the easy [100] and hard [110] directions of the 17.2 ML [Au/Fe/Ag] film at 72.91 GHz. (b) The variation of the resonance field H_{FMR} with angle θ in the plane measured from the [100] easy axis. The solid line shows the variation of H_{FMR} with θ calculated from the simplified FMR theory described in section 3.3 using the parameters listed in Table 5.1.

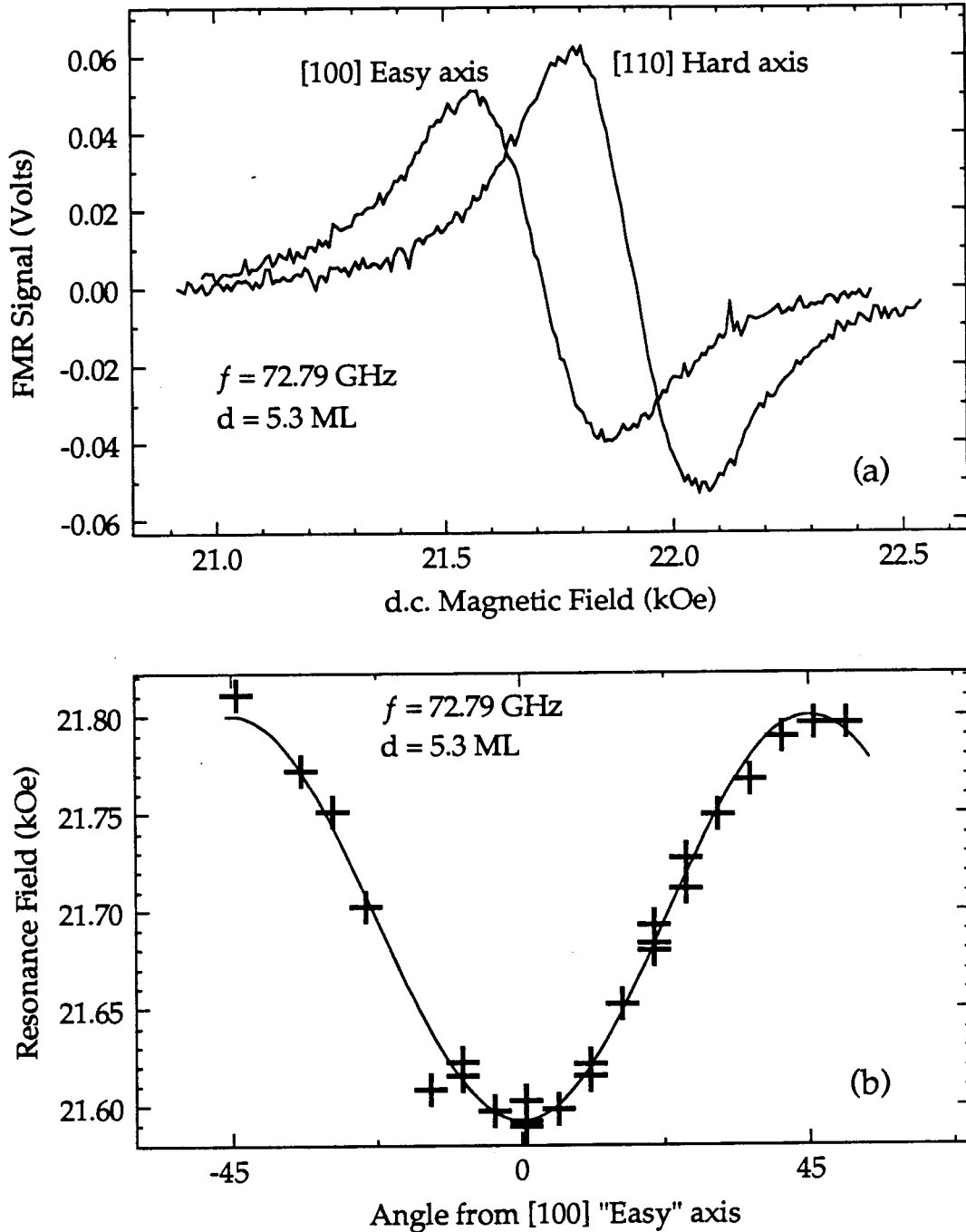


Fig. 5.3. (a) FMR absorption derivatives measured along the easy [100] and hard [110] directions of the 5.3 ML [Au/Fe/Ag] film at 72.79 GHz. (b) The variation of the resonance field H_{FMR} with angle θ in the plane measured from the [100] easy axis. The solid line shows the variation of H_{FMR} with θ calculated from the simplified FMR theory described in section 3.3 using the parameters listed in Table 5.1.

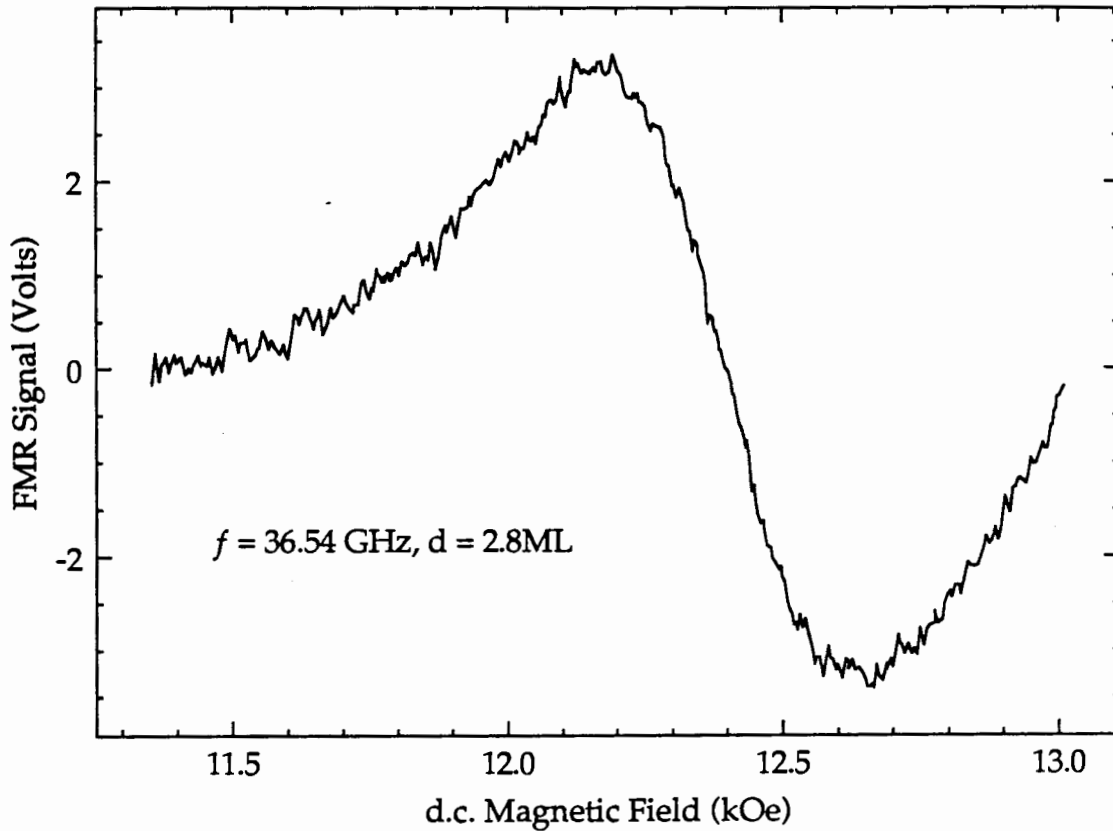


Fig. 5.4. The FMR absorption derivative measured for the 2.8 ML {Au/Fe/Ag} film at 36.54 GHz.

sumes that the rf components of the magnetization are uniform across the film (see section 3.3). The computer program that implements the full FMR absorption calculation (valid for any film thickness) was used to determine the ratio, $\beta(d)$, between the value of K_s determined from (5.2) and the value of K_s required to fit the FMR data of the four iron films using the full theory. The program showed that the relationship between K_s and $(4\pi D_z M_s)_{\text{eff}}$ was given by

$$(4\pi D_z M_s)_{\text{eff}} = 4\pi D_z M_s - \frac{2\beta(d)K_s}{M_s d} \quad (5.4)$$

TABLE 5.1. The magnetic properties of ultrathin bcc Fe(001) films grown on vicinal Ag(100) substrates.

d (ML)	T (K)	Cover Metal	$(4\pi D_z M_s)_{\text{eff}}$ (kOe)	g	$4\pi M_s$ (kOe)	D_z	H_s (kOe)	β (d)	K_s (ergs/cm ²)	K_1 (ergs/cm ³)	f_1	f_2	Freq. (GHz)	f_1	f_2
28.0	300	Au	18.084	{2.09} ^a	21.55	0.985	3.14	1.134	0.941	4.8×10^5	—	—	73.00	—	—
17.2	300	Au	16.578	2.08	21.55	0.975	4.43	1.071	0.861	4.2×10^5	4.1×10^5	—	72.91	36.50	—
5.3	300	Au	6.811	2.09	20.7	0.920	12.23	1.021	0.764	1.3×10^5	1.1×10^5	—	72.79	36.54	—
2.8	300	Au	0.562	2.09	15.2	0.848	12.33	1.010	0.299	—	—	—	72.90	36.50	—
5.3	77	Au	7.791	2.09	21.3	0.920	11.80	1.021	0.758	2.7×10^5	—	—	72.85	—	—
2.8	77	Au	0.876	2.09	22.5 ^b	0.848	13.88	1.010	0.385	—	—	—	—	—	36.63

^a Assumed to be the same as that measured for the (Ag/Fe(3ML)/Ag(001)) film at T = 300K.

^b $4\pi M_s$ at T = 77K was increased from its room temperature value by a factor of 1.5 as measured by the spin-polarized photoemission experiments of Stampanoni et al. (1987).

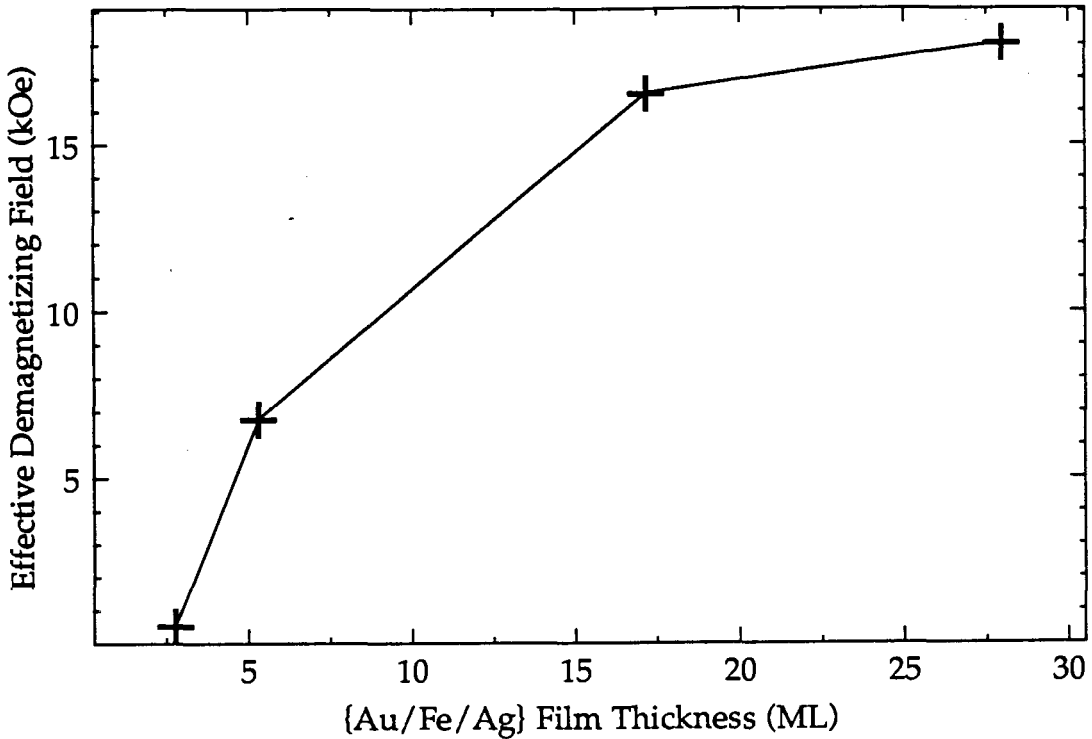


Fig. 5.5. The variation of the effective demagnetizing field $(4\pi D_z M_s)_{\text{eff}}$ with iron film thickness, d . Zero or negative values of $(4\pi D_z M_s)_{\text{eff}}$ indicate that the film is magnetized along the specimen normal in zero applied field. The plot predicts that {Au/Fe/Ag(001)} are perpendicularly magnetized for thicknesses less than 2.5ML.

where

$$\beta(d) = 0.995 + 0.00544 \cdot d(\text{ML}) \quad (5.5)$$

Note that the film thickness is expressed in terms of monolayers in equation (5.5).

The principle results of Table 5.1 are summarized in Figs. 5.5 to 5.7. The effective demagnetizing field, $(4\pi D_z M_s)_{\text{eff}}$ is plotted in Fig. 5.5 as a function of the film thickness d . The rapid decrease in $(4\pi D_z M_s)_{\text{eff}}$ with thickness clearly indicates the presence of a large uniaxial surface anisotropy with easy axis directed along the specimen normal. Extrapolation of the trend shown in Fig. 5.5 shows that the effective demagnetizing field would be less than zero for $d \leq 2.5$ ML. Thus, {Au/Fe/Ag(001)} films thinner than

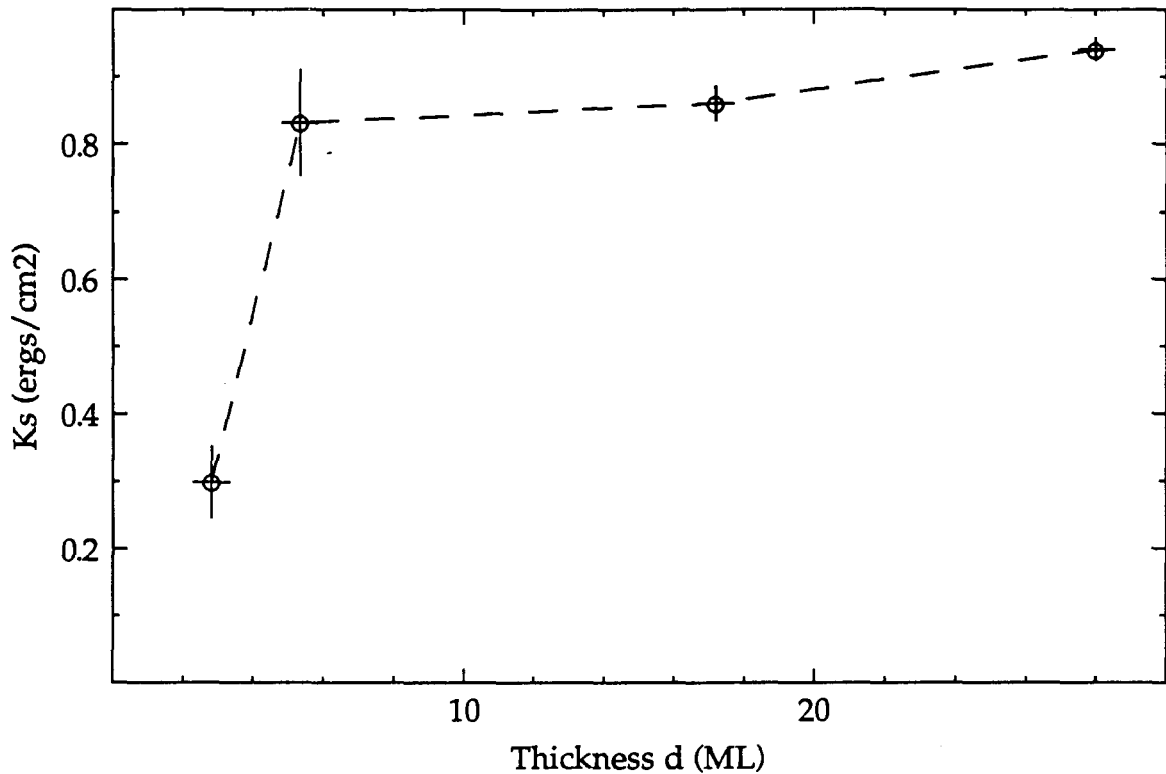


Fig. 5.6. A plot of the uniaxial surface anisotropy "constant" K_s versus film thickness d . K_s exhibits a small thickness dependence for $d > 5$ ML. It decreases by more than a factor of 2 in going from $d = 5.3$ ML to $d = 2.8$ ML.

2.5 ML should be spontaneously magnetized along the specimen normal in zero applied field. Fig. 5.6 shows a plot of K_s vs. film thickness d . The primary source of uncertainty in the plotted K_s values is the ± 0.5 ML uncertainty in the film thickness (see section 4.3). It is apparent from Fig. 5.6 that K_s slowly decreases with thickness down to $d \approx 5$ ML and then decreases more rapidly. We might expect this behavior if the uniaxial anisotropy was a property of more than just the surface atomic layers. The gradual decrease in K_s with film thickness would then be due to the increasing proximity of the two surfaces as predicted by Gay and Richter (1987).

It is also possible that the gradual increase in K_s with increasing film thickness observed for $d \geq 5\text{ML}$ is associated with the 0.6% lattice mismatch between bcc Fe(001) and the (001) face of the bulk Ag substrates. The mismatch induces a uniform strain in the ultrathin iron films that results in an additional uniaxial anisotropy field via magnetostriction (Chappert and Bruno, 1988). In this case one would obtain an "effective" uniaxial surface anisotropy coefficient, K_s^{eff} , from $(4\pi D_z M_s)_{\text{eff}}$ instead of simply K_s ; viz,

$$(4\pi D_z M_s)_{\text{eff}} = 4\pi D_z M_s - \frac{2K_s^{\text{eff}}}{M_s d} \quad (5.6a)$$

where K_s^{eff} has the thickness dependence (Appendix C):

$$K_s^{\text{eff}} = K_s + K_{\text{strain}} d \quad (5.6b)$$

where K_{strain} is the uniaxial anisotropy coefficient associated with the mismatch between the iron and silver lattices. Assuming the magnetoelastic coupling coefficient of bulk iron, and a uniform lattice strain independent of thickness, K_{strain} was calculated in Appendix C to be $-5.31 \times 10^5 \text{ ergs/cm}^3$. Fitting the values of K_s given in Table 5.1 for the $d = 5.3, 17.2,$ and 28.0 ML films to (5.6b) yields: $K_s = 0.724 \text{ ergs/cm}^2$ and $K_{\text{strain}} = +5.46 \times 10^5 \text{ ergs/cm}^3$. The difference between the calculated and the measured values of K_{strain} suggests that either: (i) uniform lattice strain is not the dominant mechanism responsible for the thickness dependence of K_s or (ii) the magnetoelastic coupling coefficient for bulk iron is not the same as the coupling coefficient for ultrathin films. The latter conclusion is more acceptable in view of the fact that Gay and Richter (1986, 1987) carried out their calculations assuming an isolated iron film stretched to conform to the lattice spacing of Fe grown on Ag(001). Their results clearly indicated that K_s

should increase with film thickness in qualitative agreement with the behaviour shown in Fig. 5.6.

All of the {Au/Fe/Ag} films exhibited a four-fold, in-plane anisotropy field, $2K_{\text{eff}}^1/M_s$, which steadily decreased with film thickness until it was unobservable at 2.8 ML (see Table 5.1). This decrease can be ascribed to the presence of an in-plane four-fold surface anisotropy which has the easy directions of magnetization along the {110} axes. In section 3.3.1 it was shown that a four-fold surface anisotropy would affect the resonant field position, H_{FMR} , in the same way as a bulk four-fold anisotropy but having a strength inversely proportional of the film thickness. The effective anisotropy field determined by FMR would therefore be given by

$$K_1^{\text{eff}} = K_1 + \frac{K_1^{\text{surf}}}{d} \quad (5.7)$$

where K_1 is the bulk four-fold anisotropy coefficient and K_1^{surf} is the surface anisotropy coefficient. If the in-plane surface anisotropy was responsible for the decrease in K_{eff}^1 then a plot of K_1^{eff} versus $1/d$ should yield a straight line. This plot is shown in Fig. 5.7 where a linear variation is clearly indicated for $d > 5$ ML. The value of the in-plane surface anisotropy coefficient was approximately $K_1^{\text{surf}} = -3.24 \times 10^{-2}$ ergs/cm² whereas the bulk cubic anisotropy constant, K_1 , was 5.57×10^5 ergs/cm³ over the 5.3–28 ML thickness range. The 16% increase in the value of K_1 over the bulk iron value of 4.8×10^5 ergs/cm³ is much smaller than the order of magnitude increases in the bulk four-fold, in-plane anisotropies of ultrathin Ni films (see Heinrich, 1988b and Jonker et al., 1988).

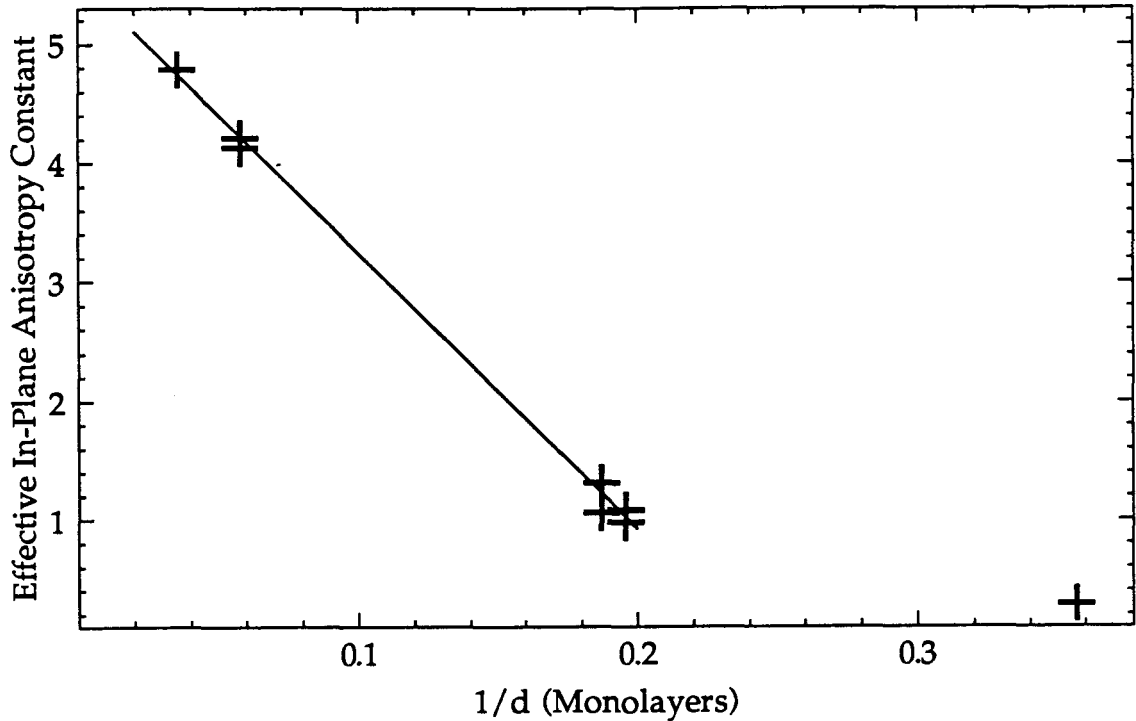


Fig. 5.7. Plot of the effective in-plane cubic anisotropy constant, K_1^{eff} versus $1/d$. The linear variation indicates the presence of a surface cubic anisotropy field having easy axes along the in-plane $\{110\}$ directions. This is contrary to the volume cubic anisotropy in bulk iron which has easy axes along the $\{100\}$ directions.

5.4 The Effect of the Coverlayer and the Role of Substrate Quality

As mentioned in section 5.1, our second set of measurements were carried out to determine if replacing the gold coverlayer with silver would result in an increase in the uniaxial anisotropy sufficient to spontaneously magnetize a 3 ML film perpendicular to the plane in zero applied field. To this end, we grew three nearly identical 3 ML bcc Fe(001) films at $T = 300\text{K}$ on vicinal silver substrates. AES and XPS studies revealed that the iron films and their silver substrates were free from contamination within the limits of resolution (± 0.03 at. %). Each specimen was then covered with 30 ML of Ag and removed from the MBE facility for *ex-situ* FMR measurements using 9.6 and

36.6 GHz spectrometers.

Representative FMR traces for a 3.0ML {Ag/Fe/Ag} film are shown in Fig. 5.8. The results of the FMR measurement are summarized in Table 5.2. The first two entries in the table correspond to the 2.8 ML {Au/Fe/Ag} film discussed in section 5.3. The third to the sixth entries describe the magnetic properties of the 3 ML {Ag/Fe/Ag} films. The last entry is associated with a special {Au/Fe/Ag/Fe[001]} structure grown on the nearly perfect [001] facet of an iron whisker and measured using Brillouin Light Scattering (BLS) – see Heinrich et al. (1988) for details. This specimen is discussed below in connection with the effect of substrate quality on the uniaxial surface anisotropy.

Table 5.2 shows that the static magnetic properties of {Ag/Fe/Ag} films do not differ significantly from the previously studied 2.8 ML {Au/Fe/Ag} specimen: there were no measurable in-plane anisotropies, the saturation magnetizations, $4\pi M_s$, were estimated to be approximately 14-15 kOe from FMR absorption intensities, and the effective demagnetizing fields, $(4\pi D_z M_s)_{\text{eff}}$ were positive and close to zero. Evidently the Au/Fe and Ag/Fe interfaces contribute almost equally to the uniaxial surface anisotropy at room temperature in these specimens. Noticeable differences occurred at low temperatures though. FMR measurements showed that the effective demagnetizing field of a 3.0 ML {Ag/Fe/Ag} film decreased from 0.32 kOe to -0.73 kOe upon cooling from $T = 300\text{K}$ to $T = 77\text{K}$ while the 2.8 ML {Au/Fe/Ag} film exhibited an increasing $(4\pi D_z M_s)_{\text{eff}}$ with decreasing temperature. As a result, the 3.0 ML {Ag/Fe/Ag} films were magnetized along the specimen normal at $T = 77\text{K}$ in zero applied field while the saturation magnetization of the {Au/Fe/Ag} film remained oriented in the plane. The uniaxial surface anisotropy increased faster than the saturation magnetization with decreasing temperature when the film was covered with silver than when the film is cov-

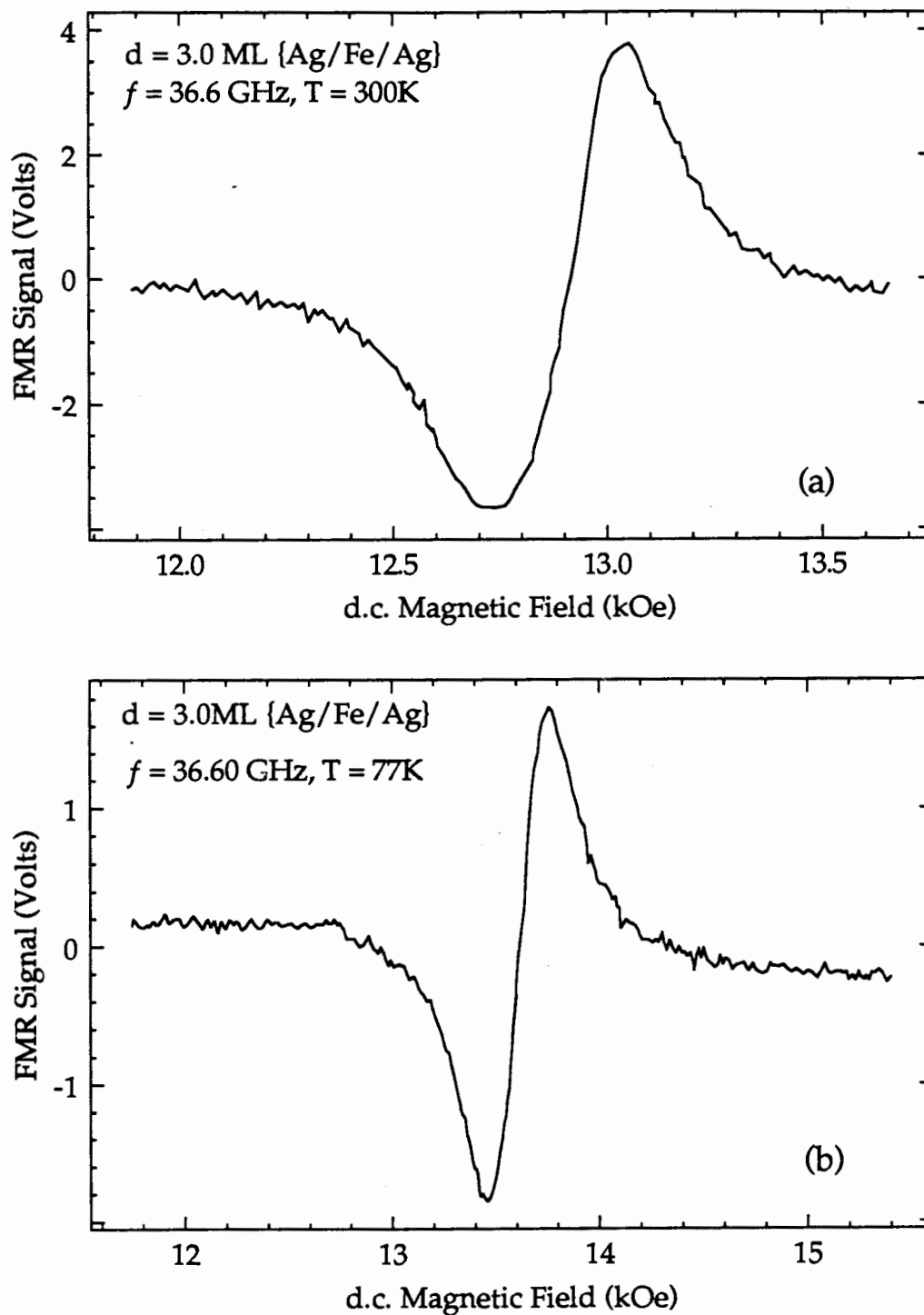


Fig. 5.8. FMR absorption derivatives measured at 36.6 GHz. (a) A 3.0 ML {Ag/Fe/Ag} film on a vicinal Ag(001) substrate measured at $T = 300 \text{ K}$. (b) The same 3.0 ML film measured at $T = 77 \text{ K}$. Note the upward shift of the resonance field upon cooling.

TABLE 5.2. The magnetic properties of ultrathin bcc Fe(001) films grown on vicinal Ag(100) substrates.

d (ML)	T (K)	Cover Metal	$(4\pi D_z M_s)_{\text{eff}}$ (kOe)	g	$4\pi M_s$ (kOe)	D_z	H_s (kOe)	β (d)	K_s (ergs/cm ²)	K_1 (ergs/cm ³)	f_1	f_2	Freq. (GHz)
2.8	300	Au	0.562	2.09	15.2	0.848	12.33	1.010	0.299	—	—	—	72.90
2.8	77	Au	0.876	2.09	22.5	0.848	13.88	1.010	0.385	—	—	—	36.63
3.0	300	Ag	0.320	2.00	14.3	0.856	11.95	1.010	0.292	—	—	—	36.60
3.0	77	Ag	-0.727	1.98	21.0	0.856	18.75	1.010	0.672	—	—	—	36.70
2.8	300	Ag	0.788	2.00 ^a	14.3 ^a	0.848	12.10	1.010	0.293	—	—	—	9.54
2.9	300	Ag	0.413	2.00 ^a	14.3 ^a	0.853	11.79	1.010	0.315	—	—	—	9.53
3.0 ^b	300	Au	-2.4	2.09	15.0	0.856	15.1	1.010	0.34	—	—	—	—

^aAssumed to be the same as that of the 3.0 ML {Ag/Fe/Ag(001)} film at T = 300K.

^bFe film grown on 15ML of Ag(001) deposited on a Fe(001) whisker facet (see Heinrich et al., 1988)

ered with gold. The result was a negative $(4\pi D_z M_s)_{\text{eff}}$ at $T = 77\text{K}$. This is consistent with studies carried out by Krebs et al. (1988) and Volkening et al. (1988) who observed that the saturation magnetization was perpendicular to the specimen plane at cryogenic temperatures ($T \leq 30\text{K}$).

The surfaces of the vicinal silver substrates used in these experiments were characterized by numerous atomic steps and short terraces approximately 40\AA wide. The large vertical mismatch associated with the steps could affect the strength of the surface anisotropies in 3 ML films (see section 4.3). The role of these atomic steps in 3 ML samples was investigated by growing a 3 ML bcc Fe(001) film on a 15 ML Ag(001) layer deposited on the nearly perfect (001) surface of an iron whisker. The surface of a whisker is characterized by atomic terraces several thousand angstroms wide (Purcell, 1988) and a correspondingly reduced number of step edges. Iron whiskers are 0.1mm wide and $\sim 10\text{mm}$ long and require special microwave cavities to be measured using FMR.

However, iron whiskers are well suited for study by Brillouin Light Scattering (BLS) in which the laser beam spot diameter was only $10\ \mu\text{m}$ wide (Dutcher et al., 1988). The results of the light scattering experiments (Heinrich et al., 1988) showed that the 3 ML specimen grown on the iron whisker exhibited the value $(4\pi D_z M_s)_{\text{eff}} \approx -2.4\ \text{kOe}$ and was therefore magnetized perpendicular to the specimen surface at room temperature. Obviously, the uniaxial anisotropies of 3 ML films depended on the quality of the substrate. All of the 3 ML {Ag/Fe/Ag} or {Au/Fe/Ag} films grown on the vicinal substrates were spontaneously magnetized in the plane at $T = 300\text{K}$.

5.5 The Surface Anisotropy at the vacuum/Fe Interface

The uniaxial anisotropy associated with the iron/vacuum interface was investigated in our last set of experiments. The bcc Fe(001) films used in this study were all grown on "singular" bulk Ag(001) substrates. The Ag substrates were aligned to within $\pm 0.25^\circ$ of the (100) plane and were characterized by surfaces consisting of a descending staircase of 500Å wide steps vertically separated by 2Å high step edges. Our previous work was carried out on "vicinal" substrates whose surfaces deviated by 1.8° from the (100) plane. The associated high density of atomic step edges was shown to result in a decreased uniaxial anisotropy. Seven bcc Fe(001) films ranging in thickness from 5.0 to 14.2 ML were grown at $T = 300\text{K}$ on singular silver substrates and measured *in-situ* without and then with a 30Å Ag coverlayer using the 16.88 GHz FMR spectrometer described in section 2.8. The principal results of the FMR measurements are summarized in Table 5.3. Based upon the values of K_s obtained for the 5.3 ML {Au/Fe/Ag} film, and the finding by Stampanoni et al. (1987) that the saturation magnetization of a 5 ML {Fe/Ag(001)} film was equal to that of bulk Fe at room temperature, we decided to grow a 5 ML thick film. We were surprised that no FMR signal could be detected in the field interval available (0–5.5 kOe) in spite of the fact that equation (5.1) predicted that the resonance should occur between 4 and 5 kOe at 16.88 GHz. We came to the conclusion that the sample might have a much higher surface anisotropy than we had expected. If FMR occurred just above the highest field available (~ 5.5 kOe) then $(4\pi D_z M_s)_{\text{eff}}$ would have been slightly less than zero corresponding to $K_s \geq 1.2$ ergs/cm² in the 5 ML Fe film.

In order to bring the resonance field within the range of our magnet, a thicker 7.6 ML {Fe/Ag(001)} film was grown. FMR traces taken for this film are shown in Fig. 5.9

TABLE 5.3. Magnetic properties of Fe(100) films grown on singular Ag(100) substrates with $4\pi M_s = 21.55$ kOe.

d (ML)	$(4\pi D_2 M_s)_{\text{eff}}$ (kOe)		δ	K_1^{eff} (ergs/cm ³)		β (d)	H_s (kOe)		K_s (ergs/cm ²)		Freq. (GHz)	oxidation (atomic %)
	bare ^a	Ag ^a		bare	Ag		bare	Ag	bare	Ag		
14.2	14.76	—	2.09	4.5×10^5	—	1.060	6.14	—	1.005	—	16.87	6%
13.9	—	13.79	2.09	—	3.8×10^5	1.059	—	7.10	—	1.138	16.87	2%
13.5	12.27	—	2.11	3.6×10^5	—	1.056	8.60	—	1.344	—	16.86	$\leq 0.03\%$
9.7	10.61	12.72	2.10	3.2×10^5	2.8×10^5	1.039	9.99	7.88	1.147	0.905	16.88	9%
7.6	2.81	6.38	2.14	1.5×10^5	1.5×10^5	1.030	17.53	13.96	1.597	1.273	16.89	$\leq 0.03\%$
5.0	~ 0.0	—	2.09	—	1.1×10^5	1.021	~ 20.0	—	1.2	—	16.88	$\leq 0.03\%$
	bare	Au ^a		bare	Au		bare	Au	bare	Au		
5.1	—	6.77	2.08	—	1.0×10^5	1.021	—	12.98	—	0.789	36.62	$\leq 0.03\%$
5.3 ^b	—	6.81	2.09	—	1.1×10^5	1.021	—	12.23	—	0.758	36.54	$\leq 0.03\%$
2.8 ^{b,c}	—	0.56	2.09	—	$< 0.3 \times 10^5$	1.010	—	12.33	—	0.252	36.05	$\leq 0.03\%$
3.0 ^{c,d}	—	-2.40	2.09	—	—	1.010	—	15.1	—	0.342	—	—

^athe notation "bare" and "Ag" (or "Au") denotes {Fe/Ag(001)} films before and after coverage with Ag (or Au).

^bFe film grown on a Ag(001) substrate misoriented by 1.8° from the (100) plane.

^cthe value of $4\pi M_s$ for these two specimens was found to be 15.0 kOe.

^dFe film grown on 15ML Ag(001) deposited on Fe(001) whisker facet (see Heinrich et al., 1988).

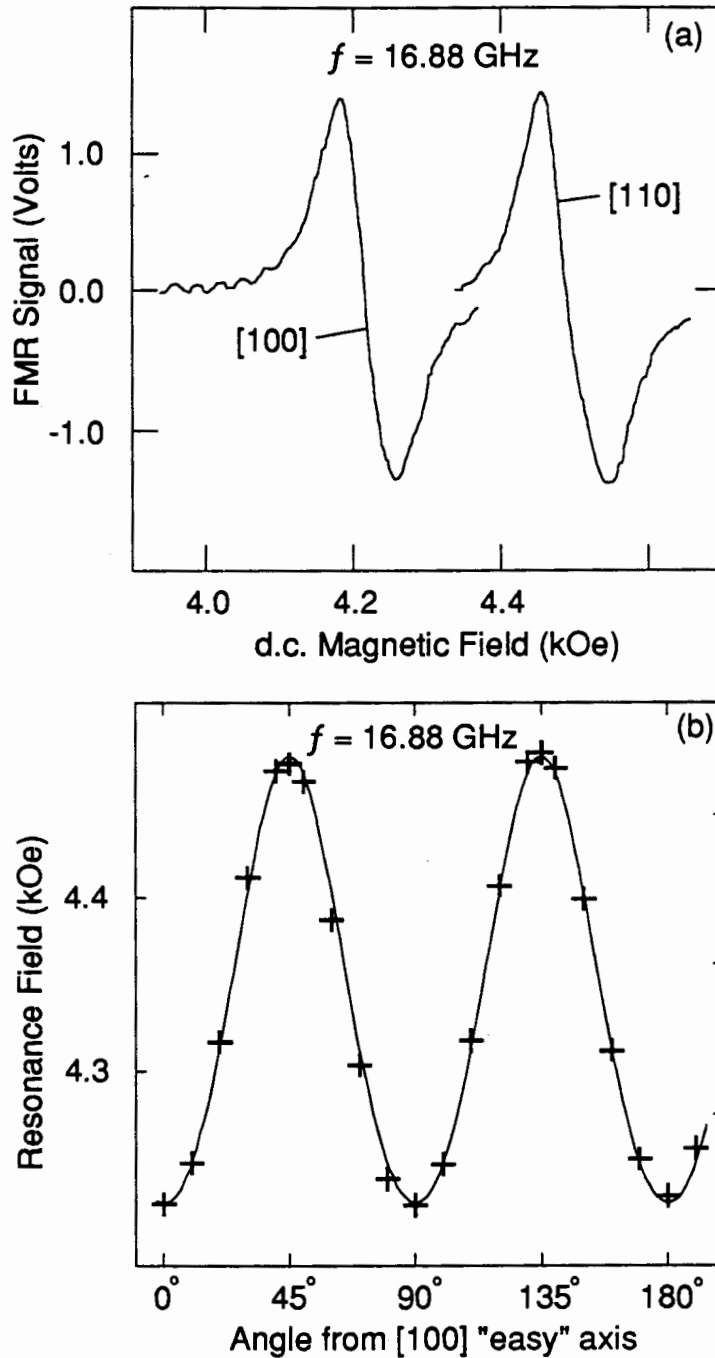


Fig. 5.9. (a) FMR traces taken along the in-plane [100] easy and [110] hard axes in ultrahigh vacuum for a 7.6 ML $\{\text{Fe}/\text{Ag}(001)\}$ film. (b) The variation of the resonance field, H_{FMR} , with the angle θ measured from the [100] in-plane direction.

along with the in-plane angular variation of H_{FMR} . The film possessed a uniaxial surface anisotropy characterized by $K_s = 1.60 \text{ ergs/cm}^2$, which decreased to 1.27 ergs/cm^2 upon covering the film with Ag (see Table 5.3). This decrease was in agreement with the predictions of Gay and Richter (1987) that the vacuum/Fe interface should exhibit a stronger uniaxial anisotropy than a Ag/Fe interface. In-plane anisotropy measurements both before and after the film was covered by Ag revealed a simple four-fold in-plane anisotropy well described by a single K_1^{eff} of $1.5 \times 10^5 \text{ ergs/cm}^3$ – a value comparable to that measured for a 5.3 ML {Au/Fe/Ag} film, $K_1^{\text{eff}} = 1.2 \times 10^5 \text{ ergs/cm}^3$. Auger analysis of the Fe film before growth of the Ag overlayer showed that the Fe film was free of oxygen contamination.

The large value found for K_s explained why no FMR signal could be measured for the 5 ML film. For $K_s = 1.60 \text{ ergs/cm}^2$, FMR would have occurred at $H_{\text{FMR}} \approx 10 \text{ kOe}$ in the 5 ML film – far beyond the 5.5 kOe upper field limit of the *in-situ* spectrometer. Further, the effective saturation magnetization of the 5 ML film would have been $(4\pi D_z M_s)_{\text{eff}} \approx -6.82 \text{ kOe}$, indicating that the film was perpendicularly magnetized at room temperature. This is different from the results of Stampanoni et al. (1987) who reported that only {Fe/Ag(001)} films 3–4 ML thick were perpendicularly magnetized and only for temperatures below $T = 15\text{K}$.

We grew two Fe films which were oxidized. One was 9.7 ML thick with 6 atomic percent (at.%) oxygen on its surface; the other was 14.2 ML thick with 9 at.% oxygen contamination (as determined by comparison of Auger peak intensities of oxygen and Ag – see section 2.7). Both specimens exhibited depressed K_s values regardless of whether the films were bare or covered with Ag. For example, a bare 13.5 ML Fe film free from oxygen contamination exhibited a value of $K_s = 1.34 \text{ ergs/cm}^2$, whereas the 6

at.% oxidized 14.2 ML Fe film exhibited a value of $K_s = 1.01 \text{ ergs/cm}^2$ (see Table 5.3). One can therefore conclude that clean, oxygen free, Fe films are a prerequisite for obtaining large K_s values. Since the films grown by Stampanoni et al. (1987) were contaminated with approximately 5-10 at. % oxygen, the K_s values for their films might have been decreased such that the saturation magnetization was oriented in the plane for films thicker than 4 ML.

We were also interested in the value of K_s in the thick film limit ($d \geq 15 \text{ ML}$). Firstly, Gay and Richter (1987) predicted that K_s should have a thickness dependence. Secondly, the growth morphology of thick films was different from that of films thinner than 8 ML. The growth studies described in section 4.3 had indicated that the thicker iron films exhibited more three dimensional surface features. An oxygen free 13.5 ML thick Fe film was grown; this film was sufficiently thick to have properties similar to bulk iron. The K_s for this film was 20% smaller than that of the bare, unoxidized 7.6 ML Fe film. Surface smoothness was therefore another significant factor which affected the strength of the uniaxial surface anisotropy.

The studies described in sections 5.3 and 5.4 were carried out on vicinal Ag substrates whose surface plane was mis-aligned with respect to the (100) surface plane by approximately 1.8° . The smaller values of K_s observed for those {Au/Fe/Ag} and {Ag/Fe/Ag} films were attributed to the presence of numerous atomic steps and ledges whose effect on the magnetic properties of the Fe films is compounded by the large vertical mismatch between the Ag and Fe lattices (see section 5.4). This conclusion was supported by BLS measurements carried out on a gold covered 3 ML Fe film deposited on an extremely smooth Ag substrate (created by growing a Ag film on top of an essentially perfect Fe(001) whisker facet). The latter specimen exhibited a larger value

of K_s than any {Au/Fe/Ag} or {Ag/Fe/Ag} film grown on a vicinal Ag substrate. The 3 ML Fe film grown on the whisker was characterized by a value of $(4\pi D_z M_s)_{\text{eff}} \approx -2.4$ kOe at $T = 300$ K; this implied that the saturation magnetization of the film was already perpendicular to the specimen plane at room temperature. It was of interest to ask if the magnetic properties of 5 ML and thicker films would also be enhanced by growing them on a singular surface which possessed a low density of atomic steps. We answered this question by growing a 5 ML Fe film on one of the singular Ag substrates and then covering it with Au instead of Ag. The overall magnetic properties of this new 5 ML film were surprisingly close to those obtained for a similar 5.3 ML thick Fe film previously grown on a vicinal Ag substrate (see the 8th and 9th entries of Table 5.3). One can therefore conclude that misorientation of the bulk Ag substrate has little effect on the value of K_s when the film thickness exceeds 5 ML.

Assuming that each Fe/Ag interface in a {Ag/Fe/Ag} film contributes equally to the total uniaxial surface anisotropy, the surface anisotropy associated with a single Fe/Ag interface of the silver covered 7.6 ML film would be 0.64 ergs/cm² and hence the contribution of the Fe/Vacuum interface to the surface anisotropy of the bare 7.6 ML {Fe/Ag(001)} film would be 0.96 ergs/cm². It is significant that the K_s value deduced for a single Ag/Fe interface is in good agreement with the value of $K_s = 0.79$ ergs/cm² obtained for surface anisotropy energies measured for a silver covered Fe(001) whisker facet using BLS (Dutcher et al., 1988). This is strong confirmation that the surface anisotropies observed for the ultrathin iron films originate from the broken symmetry associated with a surface as proposed by Gay and Richter (1987).

5.6 The Dynamic Magnetic Properties of Ultrathin Iron Films

The FMR absorption linewidth, ΔH , of ultrathin films is composed of two parts: (i) a frequency dependent component related to the intrinsic magnetic damping of the ferromagnetic metal (Kambersky, 1976) and (ii) a frequency independent part, $\Delta H(0)$, associated with inhomogeneities in the film thickness (Heinrich et al., 1985 and 1987). The expression for ΔH appropriate for our ultrathin iron films has the form (section 3.3.2):

$$\Delta H = 1.16 \left(\frac{\omega}{\gamma} \right) \left(\frac{G}{\gamma M_s} \right) + \Delta H(0) \quad (5.8)$$

where G is the intrinsic Gilbert damping parameter (Gilbert, 1955), $\gamma = g |e| / (2mc)$ is the gyromagnetic ratio, "g" is the spectroscopic g-factor, and $\Delta H(0)$ is the "inhomogeneous linewidth" or the "zero-frequency linewidth".

The Gilbert damping parameter, G , and inhomogeneous linewidth, $\Delta H(0)$, were determined for several of the ultrathin iron films grown for our investigations using the values of the experimental linewidth, ΔH_1 and ΔH_2 , obtained at two microwave frequencies ω_1 and ω_2 . The results are listed in Table 5.4 along with the g-factors extracted using the method described at the start of section 5.3.

The inhomogeneous linewidth, $\Delta H(0)$, that appears in (5.8) is a measure of the quality of the iron film growth. Local thickness variations in the film result in variations in the uniaxial anisotropy field, $H_s = 2K_s / (M_s d)$. This, in turn, causes different parts of the specimen to go through ferromagnetic resonance at slightly different values of the applied magnetic field. The associated linebroadening is independent of frequency and expressed by $\Delta H(0)$. The linebroadening should tend to increase with decreasing film thickness given a fixed amount of surface roughness. Referring to Table 5.4, one imme-

TABLE 5.4. Intrinsic magnetic damping parameters, G , and inhomogeneous linewidths, $\Delta H(0)$, of selected ultrathin bcc Fe(001) films.

d (ML)	T (K)	Cover Metal	g-factor	G (sec) ⁻¹	$\Delta H(0)$ (Oe)	Substrate Type
28.0	300	Au	2.09	{0.66×10 ⁸ } ^a	50.0	Vicinal
17.2	300	Au	2.08	0.77×10 ⁸	69.9	Vicinal
5.3	300	Au	2.09	1.9×10 ⁸	123.0	Vicinal
2.8	300	Au	2.09	3.9×10 ⁸	178.0	Vicinal
3.0	300	Ag	2.00	1.1×10 ⁸	640.0	Vicinal
13.5	300	Ag	2.11	1.6×10 ⁸	53.9	Singular
7.6	300	Ag	2.14	1.8×10 ⁸	38.6	Singular
5.1	300	Au	2.09	1.3×10 ⁸	95.5	Singular

^aAssumed to be the same as that of bulk iron.

diately notes the predicted correlation between $\Delta H(0)$ and the substrate quality. The specimens grown on singular substrates exhibit very low values for the inhomogeneous linebroadening while the films grown on the vicinal substrates possessed much larger values. For example, the 5.1 ML {Au/Fe/Ag(singular)} film had $\Delta H(0) \approx 96$ Oe while the comparable 5.3 ML {Au/Fe/Ag(vicinal)} film had $\Delta H(0) \approx 123$ Oe. For a given substrate type, the values of $\Delta H(0)$ also tended to increase with decreasing thickness as predicted (see the first four entries in Table 5.4).

The frequency dependent portion of the linewidth is caused by the spin-orbit interaction (Kambersky, 1976). The spin-dependent portions of the Fermi surface expand and contract with the precessing rf magnetization. These pulsating parts of the Fermi

surface create an effective damping field in the equation of motion for the magnetization that we accounted for in the calculations of sections 3.2 and 3.3 with the phenomenological term:

$$H_G = - \frac{G}{\gamma^2 M_s^2} \frac{\partial M}{\partial t} \quad (5.9)$$

The Gilbert damping parameter that appears in (5.8) and (5.9) is a measure of the spin-orbit interaction in the 3-d band of iron and could be directly obtained from first principle band calculations much like the magnetocrystalline anisotropy energies (Kambersky, 1976). Roughly speaking, the larger the Gilbert damping parameter, the greater the portion of the Fermi surface that changes shape in time and k-space with the precessing rf magnetization. The Gilbert damping parameters listed in Table 5.4 exhibit a steady increase with decreasing film thickness, reflecting an enhanced role of the spin-orbit interaction as the two-dimensional limit is approached. It is interesting to note that the damping parameter of the 3 ML {Ag/Fe/Ag(vicinal)} film was approximately four times smaller than the damping parameter of the comparable 2.8 ML {Au/Fe/Ag(vicinal)} film ($G = 1.1 \times 10^8 \text{ sec}^{-1}$ compared to $G = 3.9 \times 10^8 \text{ sec}^{-1}$). This suggests that the electronic structure of iron is definitely affected by the different hybridization between the *sp* bands of Au and Ag and the 3-*d* bands of iron.

The damping parameter and the magnetocrystalline anisotropy energies are measures of the spin-orbit interaction in a ferromagnet. A third measure is the spectroscopic *g*-factor which describes the orbital contribution to the total electron angular momentum (Kittel, 1949). Referring to Table 5.4, we see that the *g*-factor also exhibited some definite trends related to the type of noble metal coverlayer and the film thickness. All of the gold covered films were characterized by the bulk iron *g*-factor of 2.09. The Ag

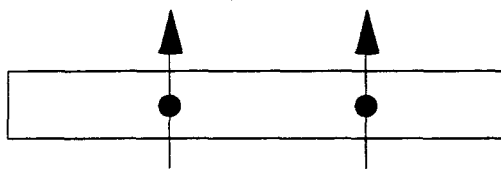
covered films thicker than 5 ML also possessed g -factors greater than or equal to the bulk value. However, as the film thickness approached the two-dimensional limit, the g -factor of the Ag covered films decreased to the free electron value of $g = 2.0$. This behaviour has been observed in 3 ML fcc Fe(001) films grown on Cu(001) substrates where the g -factor of iron was consistently *below* 2.0 (Dutcher et al., 1988). The origin of this behaviour is being investigated by Gay and Richter.

Taken together, the magnetocrystalline anisotropy energies, the magnetic damping parameter, and the g -factor provide three interrelated tests of the validity of a first principles band calculation that includes the spin-orbit interaction. Band calculations are just beginning to reach a level of maturity where they can be used to predict the electronic and the magnetic structure of ultrathin films. Experiments aimed at obtaining data for comparison to theory will serve to guide the development of the theory. In this respect, FMR is a powerful tool as it can obtain all three measures of the spin-orbit interaction. However, one must also note that our work has shown that the substrate quality, the film roughness, and the level of oxidation all affected the measured value of the surface anisotropy coefficient K_s . It is therefore vital to use the surface analysis tools of RHEED, AES, and XPS to properly characterize the physical and the chemical structure of a grown film so that one can make meaningful comparisons between theory and experiment.

Appendix A

The Ultrathin Film Demagnetizing Factor

The magnetic dipole-dipole interaction favors antiparallel alignment of parallel magnetic moments and acts to oppose the orienting effect of the exchange interaction. As a result, the energy of a uniformly magnetized film can be lowered by aligning the magnetization with the plane of the specimen:



(a) Unstable Dipole Configuration



(b) Stable Dipole Configuration

The dipole-dipole interaction generates a real magnetic field H_d (the *demagnetizing field*) inside a specimen that acts to keep the magnetization M along directions that lower the overall dipolar energy. For a uniformly magnetized ellipsoid, the demagnetizing field can be written in tensor form as (Chikazumi, 1964):

$$H_d = -4\pi D \cdot M ; \quad D = \begin{bmatrix} D_x & 0 & 0 \\ 0 & D_y & 0 \\ 0 & 0 & D_z \end{bmatrix} \quad (\text{A.1})$$

where D is the *demagnetizing tensor*. For a disc shaped specimen whose x and y dimensions are much greater than the z dimension, the tensor has components $D_x = D_y \approx 0$, $D_z \approx 1$. This demagnetizing field exerts a torque on the magnetization that acts to keep M in the plane.

Implicit in the derivation of (A.1) is the assumption that the ferromagnetic film is much thicker than the atomic spacing. This assumption is no longer valid in an ultrathin film and the demagnetizing factors must be evaluated by average magnetic field felt by each dipole in the lattice due to all the other dipoles. We carry out such a calculation for bcc Fe(001) films in this Appendix.

The dipolar field for a bcc Fe(001) lattice will be calculated assuming each lattice point contains a magnetic moment of strength $|\mathbf{m}| = (M_s a^3/2)$ where "a" is the bcc lattice constant (2.87Å for Fe). The factor of 2 accounts for the fact that a bcc unit cell contains two atoms. All of the moments are assumed to be aligned parallel. The dipoles in each lattice plane are arranged on an infinite square grid in the x and y directions. The vertical spacing between adjacent planes is $z = a/2$. Successive plane are offset from one another by $\Delta x = a/2, \Delta y = a/2$.

The magnetic field at a general point (x,y,z) due to a dipole of strength $|\mathbf{m}|$ located at (x_i, y_i, z_i) is

$$\mathbf{h}_{\text{dipole}}(\mathbf{r}) = \frac{3\mathbf{r}(\mathbf{r} \cdot \mathbf{m})}{|\mathbf{r}|^5} - \frac{\mathbf{m}}{|\mathbf{r}|^3}; \quad \mathbf{r} = \begin{bmatrix} x - x_i \\ y - y_i \\ z - z_i \end{bmatrix} \quad (\text{A.2})$$

To calculate the demagnetizing field for a monolayer, the dipole at (0,0,0) is removed and the magnetic field at (0,0,0) due to all the other dipoles is evaluated using (A.2). The dipoles are located at the points (a·j, a·k, 0) where j and k are integers. Call this field H_0 . To calculate the demagnetizing field for a bilayer structure consisting of one plane located at $z = 0$ and the other at $z = a/2$, one removes the dipole at (a/2, a/2, a/2) and evaluates the magnetic field, H_1 , at that point due to all the dipoles located in the plane at $z = 0$. The total field acting on the dipoles in the plane at $z = 0$ or $z = a/2$ is $\{H_0 + H_1\}$.

For a three monolayer film one adds a third plane at $z = a$ and evaluates the magnetic field, H_2 at $z = (0,0,a)$ due to the lattice plane at $z = 0$. By symmetry, the total field in the planes at $z = 0$ and $z = a$ is $\{H_0 + H_1 + H_2\}$ while the field in the central plane at $z = a/2$ is $\{H_0 + 2H_1\}$. The average field is $\{H_0 + 2H_1 + 2(H_0 + H_1 + H_2)\}/3$. The demagnetizing field for thicker films is calculated in a similar manner.

There are only two fields that have to be evaluated. One is the magnetic field, H_a , at a point $(0,0,a \cdot n)$ due to the dipole plane at $z = 0$. The other is the magnetic field, H_b , at a point $(a/2, a/2, a \cdot [n - 1/2])$ due to the plane at $z = 0$. In both cases "n" is an integer. The field in a monolayer is a special case of H_a with $n = 0$ and the dipole removed from $(0,0,0)$. H_a and H_b are calculated by assuming that the dipoles m successively point along the $x = (1,0,0)$, $y = (0,1,0)$, and $z = (0,0,1)$ directions. This will determine the components of the demagnetizing tensors, D_a and D_b , linking the demagnetizing fields to m or, equivalently, to M . We define the tensors by $H_a = -4\pi D_a \cdot M$ and $H_b = -4\pi D_b \cdot M$ where

$$D_a = \begin{bmatrix} D_{xx}^a & D_{xy}^a & D_{xz}^a \\ D_{yx}^a & D_{yy}^a & D_{yz}^a \\ D_{zx}^a & D_{zy}^a & D_{zz}^a \end{bmatrix}; \quad D_b = \begin{bmatrix} D_{xx}^b & D_{xy}^b & D_{xz}^b \\ D_{yx}^b & D_{yy}^b & D_{yz}^b \\ D_{zx}^b & D_{zy}^b & D_{zz}^b \end{bmatrix} \quad (A.3)$$

Evaluation of H_a

For dipole alignment along the x-direction, (A.2) yields:

$$D_{xx}^a = -\frac{1}{8\pi} \sum_{j,k} \left[\frac{3j^2}{(j^2 + k^2 + n^2)^{5/2}} - \frac{1}{(j^2 + k^2 + n^2)^{3/2}} \right] \quad (A.4a)$$

$$D_{yx}^a = -\frac{3}{8\pi} \sum_{j,k} \frac{jk}{(j^2 + k^2 + n^2)^{5/2}} \quad (\text{A.4b})$$

$$D_{zx}^a = \frac{3}{8\pi} \sum_{j,k} \frac{jn}{(j^2 + k^2 + n^2)^{5/2}} \quad (\text{A.4c})$$

For dipole alignment along the y-direction,

$$D_{xy}^a = -\frac{3}{8\pi} \sum_{j,k} \frac{jk}{(j^2 + k^2 + n^2)^{5/2}} \quad (\text{A.5a})$$

$$D_{yy}^a = -\frac{1}{8\pi} \sum_{j,k} \left[\frac{3k^2}{(j^2 + k^2 + n^2)^{5/2}} - \frac{1}{(j^2 + k^2 + n^2)^{3/2}} \right] \quad (\text{A.5b})$$

$$D_{zy}^a = \frac{3}{8\pi} \sum_{j,k} \frac{kn}{(j^2 + k^2 + n^2)^{5/2}} \quad (\text{A.5c})$$

For dipole alignment along the z-direction,

$$D_{xz}^a = \frac{3}{8\pi} \sum_{j,k} \frac{jn}{(j^2 + k^2 + n^2)^{5/2}} \quad (\text{A.6a})$$

$$D_{yz}^a = \frac{3}{8\pi} \sum_{j,k} \frac{kn}{(j^2 + k^2 + n^2)^{5/2}} \quad (\text{A.6b})$$

$$D_{zz}^a = -\frac{1}{8\pi} \sum_{j,k} \left[\frac{3n^2}{(j^2 + k^2 + n^2)^{5/2}} - \frac{1}{(j^2 + k^2 + n^2)^{3/2}} \right] \quad (\text{A.6c})$$

The sums over j and k in (A.4b) and (A.5a) are zero, as are the sums over j in (A.4c) and (A.6a) and the sums over k in (A.5c) and (A.6b). The sums (A.4a) and (A.5b) are equal by symmetry and adding (A.4a), (A.5b), and (A.6c) together yields zero; viz,

$$D_{xx}^a = D_{yy}^a \quad D_{xy}^a = D_{yx}^a = 0 \quad D_{xz}^a = D_{zx}^a = D_{yz}^a = D_{zy}^a = 0 \quad (A.7)$$

$$D_{xx}^a + D_{yy}^a + D_{zz}^a = 0 \Rightarrow D_{xx}^a = D_{yy}^a = -\frac{1}{2}D_{zz}^a$$

This leaves only the one sum (A.6c) to evaluate in order to obtain the entire demagnetizing tensor D_a :

$$D_{zz}^a = -\frac{1}{8\pi} \sum_{j,k} \left[\frac{3n^2}{(j^2 + k^2 + n^2)^{5/2}} - \frac{1}{(j^2 + k^2 + n^2)^{3/2}} \right] \quad (A.8)$$

Where the $j=k=0$ term is not included in the sum for an isolated monolayer ($n = 0$).

Evaluation of H_b

Repeating the above steps above for the magnetic field H_b at a point $(a/2, a/2, a \cdot [n - 1/2])$ due to the dipole plane at $z = 0$ yields the same symmetry relations (A.7) among the various tensor components of D_b and the single sum:

$$D_{zz}^b = -\frac{1}{8\pi} \sum_{j,k} \left[\frac{3(n - \frac{1}{2})^2}{\left((j - \frac{1}{2})^2 + (k - \frac{1}{2})^2 + (n - \frac{1}{2})^2 \right)^{5/2}} - \frac{1}{\left((j - \frac{1}{2})^2 + (k - \frac{1}{2})^2 + (n - \frac{1}{2})^2 \right)^{3/2}} \right] \quad (A.9)$$

Evaluation of the demagnetizing tensor

By (A.7)-(A.9), the demagnetizing fields H_a and H_b are related to the magnetization M by $H_a = -4\pi D_a \cdot M$ and $H_b = -4\pi D_b \cdot M$ where

$$D_a = \begin{bmatrix} -\frac{1}{2}D_{zz}^a & 0 & 0 \\ 0 & -\frac{1}{2}D_{zz}^a & 0 \\ 0 & 0 & D_{zz}^a \end{bmatrix}; \quad D_b = \begin{bmatrix} -\frac{1}{2}D_{zz}^b & 0 & 0 \\ 0 & -\frac{1}{2}D_{zz}^b & 0 \\ 0 & 0 & D_{zz}^b \end{bmatrix} \quad (A.10)$$

These can be re-written to resemble the usual demagnetizing field for a thin, flat plate ($H_d = -4\pi D_z M_z z$) by adding $2\pi D_{zz} M$ to H_a and H_b to get

$$H_a = -4\pi D_a M_z z; \quad H_b = -4\pi D_b M_z z \quad (A.11)$$

where

$$D_a = \frac{3}{2}D_{zz}^a; \quad D_b = \frac{3}{2}D_{zz}^b \quad (A.12)$$

and z is a unit vector along the z -direction. Adding a multiple of M to any effective field H_e is permissible because only the torque $M \times H_e$ enters into the Landau-Lifshitz equation of motion for M and not the effective field itself.

The demagnetizing factors (A.8) and (A.9), can be used to re-write (A.12) as:

$$D_z^a(n) = -\frac{3}{16\pi} \left(\frac{1}{2|n|^3} + 4 \sum_{j=1}^{\infty} \sum_{k=0}^{\infty} \frac{2n^2 - j^2 - k^2}{(j^2 + k^2 + n^2)^{5/2}} \right) \quad (A.13)$$

$$D_z^b(n - \frac{1}{2}) = -\frac{3}{4\pi} \sum_{j=1}^{\infty} \sum_{k=1}^{\infty} \frac{2(n - \frac{1}{2})^2 - (j - \frac{1}{2})^2 - (k - \frac{1}{2})^2}{\left((j - \frac{1}{2})^2 + (k - \frac{1}{2})^2 + (n - \frac{1}{2})^2 \right)^{5/2}} \quad (A.14)$$

where the leading term in (A.13) is ignored if $n = 0$ (ie, the summation is for an isolated monolayer) and the sums are carried out only over positive integers.

Numerical evaluation of (A.13) and (A.14) is carried out by direct summation over all points (j,k) inside a disc of radius $R = N + 1/2$, followed by an integration over continuous variables out to infinity as an approximation to the remainder of the sum.

The integral approximation for $D_z^a(n)$ is:

$$\begin{aligned}
 D_{\text{int}}^a(n) &= -\frac{3}{16\pi} \left(\sum_{j^2+k^2 > (N+\frac{1}{2})^2} \frac{2n^2 - j^2 - k^2}{(j^2 + k^2 + n^2)^{5/2}} \right) \approx -\frac{3}{16\pi} \int_0^{2\pi} \int_0^R \frac{2n^2 - r^2}{(r^2 + n^2)^{5/2}} r \, dr \, d\theta \\
 &= \frac{3R^2}{8(R^2 + n^2)^{3/2}}; \quad R = N + \frac{1}{2}
 \end{aligned} \tag{A.15}$$

where the polar coordinates $j = r \cos\theta$ and $k = r \sin\theta$ have been used in evaluating the integral.

The integral approximation for $D_z^b(n-1/2)$ is:

$$D_{\text{int}}^b\left(n - \frac{1}{2}\right) = \frac{3N^2}{8\left(N^2 + \left(n - \frac{1}{2}\right)^2\right)^{3/2}} \tag{A.16}$$

The integral correction term is VERY important. The dipole sums converge as $1/(j^2 + k^2 + n^2)^{3/2}$ which is very slow convergence. Simply carrying out the summation to a large value of N is not sufficient to insure convergence. For example, consider the

evaluation of $D_z^a(n)$ for $n = 1$ and various summation limits N :

$N = 50$	Sum = -0.02696122	Integral = 0.00742138	$D(1) = -0.01953984$
$N = 100$	Sum = -0.02327336	Integral = 0.00373079	$D(1) = -0.01954257$
$N = 400$	Sum = -0.02048037	Integral = 0.00093632	$D(1) = -0.01954405$
$N = 800$	Sum = -0.02001256	Integral = 0.00046846	$D(1) = -0.01954410$

Convergence to four places is attained for $N = 50$ when the integral correction is used.

Without the correction the sum is not even stable to 3 places by $N = 800$.

The Ultrathin Film Demagnetizing Factors

The demagnetizing factors for successive layers in a bcc Fe(001) film are (to 8 places):

$D_z^a(0)$	=	0.53915464
$D_z^b(1/2)$	=	0.24925978
$D_z^a(1)$	=	-0.01954405
$D_z^b(3/2)$	=	0.00073879
$D_z^a(2)$	=	-0.00003307
$D_z^b(5/2)$	=	0.00000141
$D_z^a(3)$	=	0.00000000

These are combined and averaged to obtain the ultrathin film demagnetizing factors as follows:

- (1) For an isolated monolayer the demagnetizing factor is just $D_z(1) = D_z^a(0) = 0.539154$

(2) For a bilayer, the demagnetizing field in the layer at $z = 0$ is equal to $-4\pi(D_z^a(0) + D_z^b(1/2))M_z z$. The demagnetizing field for the layer at $z = a/2$ is $-4\pi(D_z^a(0) + D_z^b(1/2))M_z z$. Both fields are identical and equal to $D_z(2) = 0.788414$.

(3) For three layers the factor is $D_z(3) = 0.8585$

The demagnetizing factors for films up to 12 ML thick are given in Table A.1. A plot of $D_z(n)$ versus $1/n$, where n is the film thickness in monolayers, shows that the demagnetizing factors for all $n \geq 4$ is given to four places by the simple relationship:

$$D_z(n) = 1 - \frac{0.42589}{n} \quad (\text{A.17})$$

Table A.1: The ultrathin film demagnetizing factors for bcc films up to 12 ML thick.

n (Monolayers)	$D_z(n)$
1	0.539154
2	0.788414
3	0.858472
4	0.893500
5	0.915095
6	0.929246
7	0.939354
8	0.946935
9	0.952831
10	0.957548
11	0.961407
12	0.964623

Appendix B

Silver Substrate Preparation

The ultrathin iron films used in this work were grown directly on bulk Ag(001) single crystal substrates. This appendix describes the techniques used to grind and polish the substrates prior to mounting in the MBE facility. Final *in-situ* preparation was discussed in section 4.2 of chapter 4.

B.1 Initial Preparation

The Ag(001) substrates were cut from two 99.999% pure silver single crystal boules. One boule was obtained from Kelpin Metals* of West Germany and the other from Monocrystals Inc.** of California. Laue back reflection X-Ray photographs of the boules revealed that the Kelpin crystal was composed of many small crystallites approximately 0.1mm in diameter. Adjacent grains were misaligned by approximately 20 mrad (1.1°). In contrast, the Monocrystals boule was composed of large grains of the order of 10mm on a side with adjacent grains misoriented by less than 2 mrad (0.1°).

Three Ag(001) substrates were spark cut from the Kelpin crystal and two were cut from the Monocrystals boule. The substrates were in the form of disks approximately 15mm in diameter and 4 mm thick. An error in mounting the Kelpin crystal prior to cutting resulted in the surfaces of the first three substrates being misaligned by 1.8° from the (001) plane. The surfaces of the two disks cut from the Monocrystals boule were aligned to within $\pm 0.25^\circ$ of (001).

* Kelpin Metals, Berlin, West Germany.

** MonoCrystals Inc., Hayward California.

B.2 Rough Grinding

Silver is a very soft metal and the spark cutting caused a great deal of damage to the surface of each substrate. This was removed by grinding each side of the substrate on an adhesive backed #600 Grit silicon carbide pad attached to a sheet of glass. The substrate was first cleaned with acetone and then glued to an aluminum substrate holder using Crystalbond™, a low melting point (50°C) resinous cement. The holder, in turn, was bolted to the polishing jig shown in Fig. B.1. The jig served to keep the surfaces of the substrate parallel to one another and parallel with the (001) plane throughout the grinding and polishing process.

Grinding was done by hand using a simple back and forth motion, rotating the jig approximately 30° about its center every 10-20 strokes. This technique insured uniform wear to all parts of the substrate surface. Water was used as a lubricant. The stroke

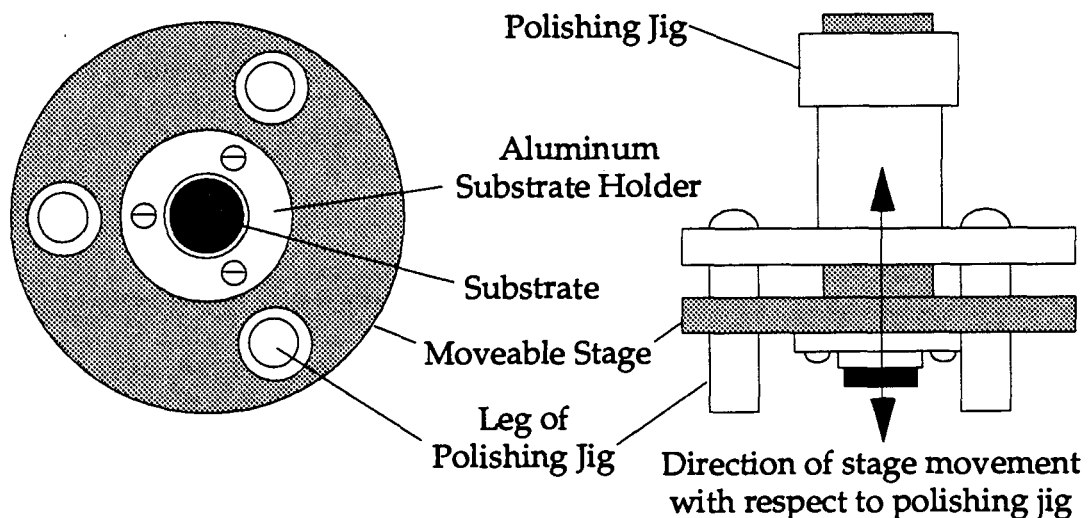


Fig. B.1. The polishing jig used to hold a substrate during grinding and polishing. The substrate is glued to an aluminum holder with beeswax or a resinous cement. The holder is bolted to a stage that can move up and down with respect to the jig. The jig serves to keep the substrate faces plane-parallel during grinding and polishing.

length was kept between 4-8cm. Grinding was continued until all visible traces of damage and grooving due to the spark cutter were removed. This required removal of approximately 0.2mm of material. To be safe, an additional 0.05-0.1 mm was often ground off to insure that the damaged surface layer had been completely eliminated. The substrate was then dismounted from the aluminum substrate holder, carefully cleaned with acetone and a cotton swab, and then remounted upside down so that the other side could be ground smooth on the #600 grit pad.

B.3 Fine Grinding

Fine grinding was carried out on adhesive backed nylon polishing pads attached to a clean sheet of glass. Aluminum oxide polishing compound* mixed with water was used as the grinding compound. Diamond pastes were not used because the small pieces of diamond tended to embed themselves in the soft silver much more easily than the aluminum oxide during the grinding process. The diamond grains would then pop out during later grinding stages to scratch the surface of the substrate or were released during final electrochemical polishing to leave behind very large craters which spoiled the surface.

Only the side of the substrate chosen for growth needed to be fine ground. Grinding commenced with 9 μ m aluminum oxide and proceeded through 5 μ m, 3 μ m, and then 1 μ m powders. Twenty minutes of grinding with each abrasive was sufficient to remove the scratching and damage left behind by the previous grit. Care was taken to clean thoroughly the substrate and the polishing jig when changing to a finer grit size. Stray grains left behind from a previous grinding step would readily produce large scratches on the substrate that required a long time to grind out.

* Available from the Linde Corporation under the trade names LindeA and LindeC.

A word of caution is in order here. Aluminum oxide mixed with water seemed to chemically react with the silver. The silver surface would rapidly tarnish if the polishing compound was left in contact with the metal for more than a minute after grinding was stopped. We're unsure of the precise cause of this effect but it could be prevented by prompt cleaning of the substrate with a cotton swab dipped in acetone. Gentle pressure must be used when cleaning to prevent scratching.

B.4 Electropolishing

Final polishing of the substrate was carried out electrochemically using the cyanide free electropolish developed by Lyles *et al.* (1978). The polishing cell is shown in Fig. B.2. It was basically a plexiglass trough. At one end a thin sheet of aluminum held by an alligator clip was connected by a braided copper wire to the negative terminal of a DC power supply. The aluminum sheet was a little smaller than the end-wall of the trough and formed the cathode of the polishing circuit. The substrate and its holder were placed at the other end of the cell. A braided copper wire passed through one of the holder's screw holes and was connected to the positive terminal of the power supply to form the anode. The cyanide-free silver electropolish consisted of:

115 ml Glacial Acetic Acid
43 ml Concentrated Sulfuric Acid
350 ml Anhydrous Methyl Alcohol
77 gm Thiourea (NH_2CSNH_2)

The method and order of mixing was important (Lyles *et al.*, 1978). A 750 ml Erlenmeyer flask was placed in an ice bath and the 115 ml of glacial acetic acid added to the flask. The 43 ml of sulfuric acid was then *slowly* mixed in. A great deal of heat is evolved during this process. The methanol and the thiourea were added last. The thiourea generally took a long time to dissolve into the solution. Twenty to sixty minutes

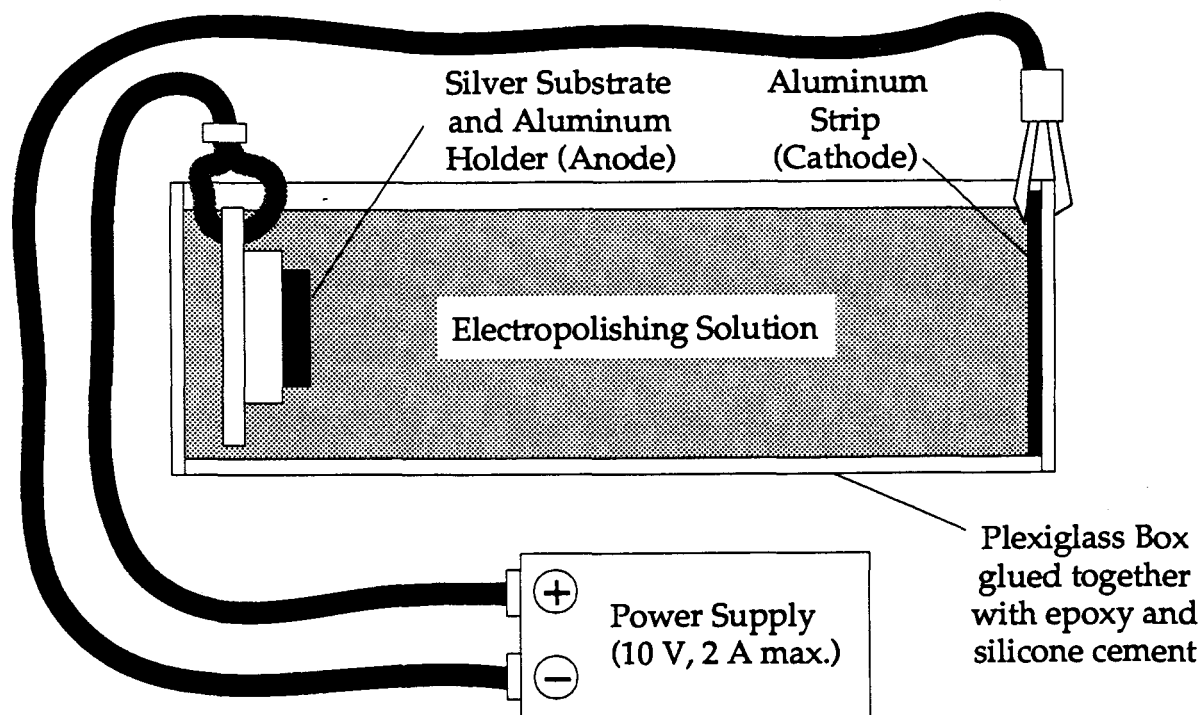


Fig. B.2. An electropolishing bath consisting of a plexiglass box glued together with epoxy and silicone cement. The substrate acts as the anode and an aluminum strip is the cathode. For silver, a potential of 9 Volts DC is maintained across the cell.

was not uncommon. Care must be taken not to get any water into the solution. It tended to inhibit the polishing action.

Electropolishing was carried out by means of a 9 Volt potential maintained across the cell at current of 1.5-1.8 Amp. The substrate and holder were placed in the cell and the power supply turned on. A white bloom tended to appear immediately on the silver surface. The white bloom was due to elemental sulfur precipitating out of the polishing solution and on to the surface. The bloom was removed by removing the silver from the bath and gently dabbing the surface with a cotton swab moistened with the electropolish. When the substrate was returned to the bath the bloom would generally not form a second time. The substrate was kept in the bath for approximately five min-

utes. Slowly moving the substrate back and forth in the solution seemed to help the polishing action. Violent agitation of the substrate is to be avoided. It tends to inhibit the polishing process (Taggert, 1964). During polishing, elemental sulfur continually precipitated out of solution and into the bath. If appreciable amounts settled on the substrate they could be removed in the same way as the initial white bloom. Five minutes in the bath was usually sufficient to obtain a substrate surface which was mirror smooth. Polishing for longer than 8 minutes seemed to promote surface pitting.

B.5 Final Cleaning

Cleaning the substrate after electropolishing required some care. Immediately upon removal from the electropolish the substrate had to be washed with a stream of acetone from a squirt bottle to flush off the polishing solution. Failure to do so would result in large amounts of elemental sulfur settling out on the surface as a greasy white mass. When sulfur was left on the surface, a cotton swab was used to dab small amounts of electropolishing solution onto the affected areas. The sulfur would go back into solution and could be flushed off with more acetone. The substrate was then dried by means of a jet of dry nitrogen gas and removed from the aluminum holder by the application of low heat to melt the glue which held the substrate to the holder.

Final cleaning was carried out ultrasonically. The substrate was given three 5 minute cleanings in pure acetone, followed by three 5 minute cleanings in anhydrous methanol. The acetone and methanol were changed after each 5 minute session. The substrate was suspended in the solvents in a fiberglass net. Direct contact between the substrate and vibrating walls of the ultrasonic cleaner caused severe damage to the polished surfaces of the substrate: cloudy patches were produced all over the polished face.

Appendix C

Strain-Induced Uniaxial Anisotropy

The ultrathin iron films used in this work were grown directly on bulk Ag(001) single crystal substrates. In section 1.2 it was shown that the (001) face of Ag looks like the (001) face of Fe after a 45° rotation in the plane (see Fig. 1.1) except that the lattice constant for the Ag(001) face is $a_{\text{Ag}} = 2.8839\text{\AA}$ compared with $a_{\text{Fe}} = 2.8665\text{\AA}$ for iron. The 0.6% mismatch results in a small homogenous strain in the iron film. This strain could be expected to produce an additional volume anisotropy in the iron film due to magnetostriction (Chikazumi, 1964). In this appendix we derive the form of this additional anisotropy term, calculate the value of the anisotropy coefficient assuming uniform strain throughout the iron film, and then show how it can give a thickness dependence to the experimentally measurable uniaxial perpendicular surface anisotropy coefficient K_s (see section 5.3 and Fig. 5.6 for further details).

C.1 The effective field associated with lattice strain

Consider a cubic lattice whose strain tensor components are given by ϵ_{11} , ϵ_{22} , ϵ_{33} , ϵ_{12} , ϵ_{23} , and ϵ_{31} . Coupling between the elastic strain and the magnetization direction may be formally taken into account by including the following term in the total energy per unit volume of the film (Chikazumi, 1964):

$$\begin{aligned}
 E_{\text{strain}} = & B_1 \left[\epsilon_{11} \left(\alpha_1^2 - \frac{1}{3} \right) + \epsilon_{22} \left(\alpha_2^2 - \frac{1}{3} \right) + \epsilon_{33} \left(\alpha_3^2 - \frac{1}{3} \right) \right] \\
 & + B_2 \left[\epsilon_{12} \alpha_1 \alpha_2 + \epsilon_{23} \alpha_2 \alpha_3 + \epsilon_{31} \alpha_3 \alpha_1 \right]
 \end{aligned} \tag{C.1}$$

where $\alpha_i = M_i/M_s$ are the direction cosines of the magnetization referenced to the [100], [010], and [001] cube edges and B_1 and B_2 are the magnetoelastic coupling coefficients. For iron, $B_1 = -2.95 \times 10^7$ ergs/cm³ and $B_2 = 7.12 \times 10^7$ ergs/cm³ (Chikazumi, 1964).

An iron film deposited on the (001) face of Ag will be uniformly strained due the small lattice mismatch between the two metals (the iron lattice will be stretched by 0.6% in the [100] and [010] directions). If, to a first approximation, it is assumed that the volume change of the film is zero then $\epsilon_{11} + \epsilon_{22} + \epsilon_{33} = 0$ and the components of the strain tensor are:

$$\begin{aligned}\epsilon_{11} = \epsilon_{22} &= -\frac{1}{2}\epsilon_{33} = 0.006 \\ \epsilon_{12} = \epsilon_{23} = \epsilon_{31} &= 0\end{aligned}\tag{C.2}$$

Substituting (C.2) into (C.1) results in the strain energy expression:

$$E_{\text{strain}} = B_1 \left[\epsilon_{11} \left(\alpha_1^2 - \frac{1}{3} \right) + \epsilon_{11} \left(\alpha_2^2 - \frac{1}{3} \right) - 2\epsilon_{11} \left(\alpha_3^2 - \frac{1}{3} \right) \right]\tag{C.3}$$

which, upon adding and subtracting $B_1 \epsilon_{11} (\alpha_3^2 - 1/3)$, reduces to the simple form:

$$E_{\text{strain}} = B_1 \epsilon_{11} \left[1 - 3\alpha_3^2 \right] = B_1 \epsilon_{11} - 3B_1 \epsilon_{11} \left(\frac{m_z}{M_s} \right)^2\tag{C.4}$$

The strain energy density (C.4) contributes an effective magnetic field to the equation of motion for the magnetization (eq. 3.9) which can be written as:

$$H_{\text{strain}}^z = -\frac{\partial E_{\text{strain}}}{\partial m_z} = \frac{2K_{\text{strain}}}{M_s^2} m_z\tag{C.5}$$

where:
$$K_{\text{strain}} = 3B_1 \epsilon_{11} \quad (\text{C.6})$$

is the anisotropy coefficient associated with the lattice strain. Equation (C.5) is formally identical to the effective field associated with a bulk uniaxial magnetocrystalline anisotropy with symmetry axis normal to the film plane (ie, along the [001] direction). The strain anisotropy coefficient has the value of $K_{\text{strain}} = -5.31 \times 10^5 \text{ ergs/cm}^3$ for the magnetoelastic coupling coefficient of bulk iron ($B_1 = -2.95 \times 10^7 \text{ ergs/cm}^3$) and the Fe lattice strain of $\epsilon_{11} = (a_{\text{Ag}} - a_{\text{Fe}})/a_{\text{Fe}} = 0.006$. The effective field (C.5) therefore acts to keep the magnetization in the specimen plane.

C.2 The effect of lattice strain on the FMR condition

Adding the effective field (C.5) to the equation of motion (3.9), and then carrying through the calculations detailed in section 3.2 and 3.3, shows that a uniform lattice strain in the iron film will modify the definition of the effective demagnetizing field, $(4\pi D_z M_s)_{\text{eff}}$ in the ultrathin film resonance condition:

$$\left(\frac{\omega}{\gamma}\right)^2 = \left[H_{\text{FMR}} + (4\pi D_z M_s)_{\text{eff}} + \frac{K_1^{\text{eff}}}{2M_s} (3 + \cos 4\theta) \right] \left[H_{\text{FMR}} + \frac{2K_1^{\text{eff}}}{M_s} \cos 4\theta \right] \quad (\text{C.7})$$

from
$$(4\pi D_z M_s)_{\text{eff}} = 4\pi D_z M_s - \frac{2K_s}{M_s d} \quad (\text{C.8})$$

to
$$\begin{aligned} (4\pi D_z M_s)_{\text{eff}} &= 4\pi D_z M_s - \left[\frac{2K_s}{M_s d} + \frac{2K_{\text{strain}}}{M_s} \right] \\ &= 4\pi D_z M_s - \frac{2(K_s + K_{\text{strain}} d)}{M_s d} \end{aligned} \quad (\text{C.9})$$

FMR experiments determine both $(4\pi D_z M_s)_{\text{eff}}$ and M_s for a given film (see the discussion at the start of section 5.3). The surface anisotropy coefficient, K_s , is then calculated from the experimental data using (C.8). However, equation (C.9) shows that in the presence of a uniform strain in the iron film we would actually be calculating an "effective" uniaxial surface anisotropy coefficient having the thickness dependence:

$$K_s^{\text{eff}} = K_s + K_{\text{strain}} d \quad (\text{C.10})$$

For iron, $K_{\text{strain}} = -5.31 \times 10^5 \text{ ergs/cm}^3 < 0$ so that the experimentally obtained surface anisotropy coefficient, K_s^{eff} , should *increase* in value with decreasing film thickness as a result of the lattice mismatch between the iron and silver lattices (assuming a uniform strain that is independent of film thickness and a magnetoelastic coupling constant, B_1 , measured for bulk iron).

References

Ament and Rado, 1955

W.S. Ament and G.T. Rado, *Phys. Rev.* **97**, 1558 (1955).

Bader and Moog, 1987

S.D. Bader and E.R. Moog, *J. Appl. Phys.* **61**, 3729 (1987).

Borer, 1978

K. Borer and G. Fremont, *Nucl. Instr. and Meth.* **154**, 61 (1978).

Briggs and Rivière, 1983

D. Briggs and J.C. Rivière, in Chapter 3 of *“Practical Surface Analysis by Auger and X-ray Photoelectron Spectroscopy”*, D. Briggs and M.P. Seah editors (John Wiley & Sons, New York, 1983).

Briggs and Seah, 1983

“Practical Surface Analysis by Auger and X-ray Photoelectron Spectroscopy”, D. Briggs and M.P. Seah editors (John Wiley & Sons, New York, 1983).

Chappert and Bruno, 1988

C. Chappert and P. Bruno, *J. Appl. Phys.* **64**, 5736 (1988).

Chikazumi, 1964

Soshin Chikazumi, *“Physics of Magnetism”* (John Wiley & Sons, Inc., New York 1964).

Cochran et al., 1977a

J.F. Cochran, B. Heinrich, and G. Dewar, *Can. J. Phys.* **55**, 787 (1977).

Cochran et al., 1977b

J.F. Cochran, B. Heinrich, and R. Baartman, *Can. J. Phys.* **55**, 806 (1977).

Cochran and Heinrich, 1980

J.F. Cochran and B. Heinrich, *IEEE Trans. Magn.* **16**, 660 (1980).

Cochran et al., 1982

J.F. Cochran, K. Myrtle, and B. Heinrich, *J. Appl. Phys.* **53**, 2261 (1982).

Cochran et al., 1986

J.F. Cochran, B. Heinrich, and A.S. Arrott, *Phys. Rev.* **B34**, 7788 (1986).

Cohen et al., 1987

P.I. Cohen, P.R. Pukite, and S. Batra in *"Thin Film Growth Techniques for Low Dimensional Structures"*. Edited by R.F.C. Farrow, S.S.P. Parkin, P.J. Dobson, J.H. Neave, and A.S. Arrott (Plenum Press, New York 1987).

Davis et al., 1979

L.E. Davis, N.C. MacDonald, P.W. Palmberg, G.E. Riach, and R.E. Weber, *"Handbook of Auger Electron Spectroscopy"* (Perkin-Elmer, Eden Prairie MN, 1979).

Dutcher et al., 1989

J.R. Dutcher, J.F. Cochran, B. Heinrich, and A.S. Arrott, *J. Appl. Phys.* **64**, 6095 (1988).

Farrow et al., 1987

"Thin Film Growth Techniques for Low Dimensional Structures". Edited by R.F.C. Farrow, S.S.P. Parkin, P.J. Dobson, J.H. Neave, and A.S. Arrott (Plenum Press, New York 1987).

Feher, 1957

G. Feher, *Bell System Tech. J.* **36**, 449 (1957).

Fu et al., 1985

C.L. Fu, A.J. Freeman, and T. Ogouchi, *Phys. Rev. Lett.* **54**, 2704 (1985).

Gay and Richter, 1986

J.G. Gay and Roy Richter, *Phys. Rev. Lett.* **56**, 2728 (1986).

Gay and Richter, 1987

J.G. Gay and Roy Richter, *J. Appl. Phys.* **61**, 3362 (1987).

Ginzton, 1957

E.L. Ginzton, *"Microwave Measurements"* (McGraw-Hill, New York, 1957).

Gilbert, 1955

T.L. Gilbert, *Phys. Rev.* **100**, 1243 (1955).

Gradmann, 1974

U. Gradmann, *Appl. Phys.* **3**, 161 (1974).

Gurevich, 1963

A.G. Gurevich, *"Ferrites at Microwave Frequencies"* (Consultants Bureau, New York 1963).

Heinrich, Cochran, and Baartman, 1977

B. Heinrich, J.F. Cochran, and R. Baartman, *Can. J. Phys.* **55**, 806 (1977).

Heinrich and Cochran, 1985

B. Heinrich and J.F. Cochran, *J. Appl. Phys.* **57**, 3690 (1985).

Heinrich et al., 1987a

B. Heinrich, A.S. Arrott, J.F. Cochran, S.T. Purcell, K.B. Urquhart, N. Alberding, and C. Liu in *"Thin Film Growth Techniques for Low Dimensional Structures"*. Edited by R.F.C. Farrow, S.S.P. Parkin, P.J. Dobson, J.H. Neave, and A.S. Arrott (Plenum Press, New York 1987).

Heinrich et al., 1987b

B. Heinrich, K.B. Urquhart, A.S. Arrott, J.F. Cochran, K. Myrtle, and S.T. Purcell, *Phys. Rev. Lett.* **59**, 1756 (1987).

Heinrich et al., 1988

B. Heinrich, K.B. Urquhart, J.R. Dutcher, S.T. Purcell, J.F. Cochran, A.S. Arrott, D.A. Steigerwald, and W.F. Egelhoff, Jr., *J. App. Phys.* **63**, 3863 (1988).

Heinrich et al., 1988b

B. Heinrich, S.T. Purcell, J.R. Dutcher, K.B. Urquhart, J.F. Cochran, and A.S. Arrott, *Phys. Rev.* **B38**, 12879 (1988).

Lent and Cohen, 1986

C.S. Lent and P.I. Cohen, *Phys. Rev. B* **33**, 8329 (1986).

Lilienkamp et al, 1988

G. Lilienkamp, C. Koziol, and E. Bauer in "*Reflection High Energy Electron Diffraction and Reflection Electron Imaging of Surfaces*". Edited by P.K. Larsen and P.J. Dobson (Plenum Press, New York 1988).

Jackson, 1975

J.D. Jackson, "*Classical Electrodynamics (2nd Edition)*" (John Wiley & Sons, New York, 1975).

Jonker et al., 1986

B.T. Jonker, K.H. Walker, E. Kisker, G.A. Prinz, and C. Carbone, *Phys. Rev. Lett.* **57**, 142 (1986).

Jonker et al., 1988

B.T. Jonker, J.J. Krebs, and G.A. Prinz, *J. Appl. Phys.*, **64**, 5340 (1988).

Kambersky, 1976

V. Kambersky, *Czech. J. Phys.* **B26**, 1366 (1976).

Kittel, 1949

C. Kittel, *Phys. Rev.* **76**, 743 (1949).

Krebs et al., 1988

J.J. Krebs, B.T. Jonker, and G.A. Prinz, *J. Appl. Phys.* **63**, 3467 (1988).

Lyles et al, 1978

R.L. Lyles Jr., S. J. Rothman, W. Jager, *Metallography* **11**, 361 (1978).

Neave et al., 1983

J.H. Neave, B.A. Joyce, P.J. Dobson, and N.Norton, *Appl. Phys.* **A31**, 1 (1983).

Pendry, 1975

J.B. Pendry, "*Low Energy Electron Diffraction*" (Academic Press, London, 1975).

Poole, 1967

C.P. Poole, *"Electron Spin Resonance – A Comprehensive Treatise on Experimental Techniques"*, (Interscience, New York, 1967).

Richter et al., 1985

Roy Richter, J.G. Gay, and John. R. Smith, *Phys. Rev. Lett.* **54**, 2704 (1985);
Roy Richter, J.G. Gay, and J.R. Smith, *J. Vac. Sci. Technol.* **A3**, 1498 (1985).

Purcell et al., 1987

S.T. Purcell, B. Heinrich, and A.S. Arrott *Phys. Rev.* **B35**, 6458 (1987).

Purcell et al., 1988a

S.T. Purcell, A.S. Arrott, and B. Heinrich, *J. Vac. Sci. Technol.* **B6**, 794 (1988).

Purcell et al., 1988b

S.T. Purcell, B. Heinrich, and A.S. Arrott, *J. Appl. Phys.* **64**, 5337 (1988).

Rado and Weertman, 1959

G.T. Rado and J.R. Weertman, *J. Phys. Chem. Solids* **11**, 315 (1959).

Rado, 1982

G.T. Rado, *Phys. Rev.* **B26**, 295 (1982); **B32**, 6061(E) (1985).

Rado, 1986

G.T. Rado and Lu Zhang, *Phys. Rev.* **B33**, 5080 (1986).

Rudd, 1985

J.M. Rudd, *"Ferromagnetic Resonance in Nickel at Low Temperatures"* (Master's Thesis, Simon Fraser University, 1985).

Seah and Dench, 1981

M.P. Seah and W.A. Dench, *Surface and Interface Analysis*, **1**, 2 (1979).

Smith et al., 1982

G.C. Smith, H.A. Padmore, and C. Norris, *Surf. Sci.* **119**, 1287 (1982).

Stampanoni et al., 1987

M. Stampanoni, A. Vaterlaus, M. Aeschlimann, and F. Meier, *Phys. Rev. Lett* **59**, 2483 (1987).

Tegart, 1959

W.J.McG. Tegart, "*The Electrolytic and Chemical Polishing of Metals*" (Pergamon Press, London 1959).

Turov, 1965

E.A. Turov in Chapter 3 of "*Ferromagnetic Resonance*" edited by S. Vonsovskii (Pergamon Press, London 1965).

Urquhart et al., 1988

K.B. Urquhart, B. Heinrich, J.F. Cochran, A.S. Arrott, and K. Myrtle, *J. Appl. Phys.* **64**, 5334 (1988).

Van Hove et al., 1983

J.M. Van Hove, C.S. Lent, P.R. Pukite, and P.I. Cohen, *J. Vac. Sci. Technol.* **B1**, 741 (1983).

van der Merwe, 1982

J.H. van der Merwe, *Phil. Mag.* **A45**, pp. 127-240 (1982).

Volkening et al., 1988

F.A. Volkening, B.T. Jonker, J.J. Krebs, N.C. Koon, and G.A. Prinz, *J. Appl. Phys.* **63**, 3869 (1988).

Wagner et al., 1979

C.D. Wagner, W.M. Riggs, L.E. Davis, J.F. Moulder, and G.E. Muilenberg, "*Handbook of X-ray Photoelectron Spectroscopy*" (Perkin-Elmer, Eden Prairie MN, 1979).

Wang et al., 1981

D.S. Wang, A.J. Freeman, and H. Krakauer, *Phys. Rev.* **B24**, 1126 (1981).

Zajac et al., 1985

G. Zajac, S.D. Bader, and R.J. Friddle, *Phys. Rev.* **B31**, 4947 (1985).